CANTILEVER AND TIP DESIGN FOR MODIFIED LATERAL FORCE MICROSCOPY

by

Mengying Wang

A Thesis

Submitted to the Faculty of Purdue University

In Partial Fulfillment of the Requirements for the degree of

Master of Science

School of Engineering Technology

West Lafayette, Indiana

August 2019

THE PURDUE UNIVERSITY GRADUATE SCHOOL
STATEMENT OF COMMITTEE APPROVAL

Dr. Helen McNally, Chair

School of Engineering Technology

Dr. Mark French

School of Engineering Technology

Dr. Haiyan (Henry) Zhang

School of Engineering Technology

Approved by:

Dr. Duane Dunlap

Head of the Graduate Program

Dedicated to my beloved parents

For their unconditional support and love.

ACKNOWLEDGMENTS

I am grateful to my advisor, Dr. Helen McNally for her support, guidance and understanding through the thesis process and the graduate program. I would like to appreciate Dr. Mark French and Dr. Haiyan Zhang for their assistance and advice through my project. I would like to thank Dr. Ragu Athinarayanan and Dr. Nancy Denton for their support and trust on my TA work. I am thankful for Niedra McLeland for her help and effort during my stay at Purdue.

I would like to appreciate my parents Fengmei Li and Yanzhen Wang for their unconditional love and faith in me. I would also say thank you to my friends and family here: Mabel, Zhui and Lynn. I appreciate your company and friendship.

At last, I would like to appreciate my time and experiences at Purdue for making me stronger and better.

TABLE OF CONTENTS

LIST OF TABLES

LIST OF FIGURES

GLOSSARY

***Lateral force microscopy (LFM)*,** also known as friction force microscopy (FFM) – LFM performs surface friction force measurements using contact mode AFM where the probe scans across the sample surface. The torsion of cantilever caused by the friction force acting on the tip is detected by the laser focused on the end of cantilever and reflected on to a photodiode (Mate, et al.,1987).

Measurement sensitivity – Measurement sensitivity in this study describes the probe's response to applied forces and is defined as the ratio of the twist angle of the cantilever to the lateral force applied on the tip.

Modified lateral force microscopy (mLFM) – The technique developed on the basis of LFM to conduct force measurements on the samples through measuring the torsion of the cantilever induced by the direct contact between the sidewall of the tip and the sample in the lateral direction (Hseu, 2015).

Probe – The probe of LFM and mLFM consists of a cantilever with one end fixed on a substrate and a small tip attached at the bottom of the free end (Morris, Kirby, & Gunning, 2014).

Torsional spring constant – Torsional spring constant describes the stiffness or flexibility of a subject in the torsional direction and is defined as the ratio of the torque applied to the rotation angle about the major axis caused by the torque (Sader, 2003).

LIST OF ABBREVIATIONS

AFM – atomic force microscopy

DOE – design of experiments

FEA – finite element analysis

FEM – finite element modeling

FFM – friction force microscopy

LFM – lateral force microscopy

LHD – Latin hypercube design

MFM – magnetic force microscopy

mLFM – modified lateral force microscopy

PSPD – position sensitive photodiode

SCM – scanning capacitance microscopy

SPM – scanning probe microscopy

SSRM – scanning spreading resistance microscopy

STM – scanning tunneling microscopy

ABSTRACT

Author: Mengying, Wang. MS
Institution: Purdue University
Degree Received: August 2019
Title: Cantilever and Tip Design for Modified Lateral Force Microscopy
Committee Chair: Dr. Helen McNally

The atomic force microscopy (AFM) has been widely used for the investigation of the surface topography and high precision force measurements at the nano-scale. Researchers have utilized AFM to quantify the viscosity of the cell membrane in the vertical direction, which is a primary indicator of a cell's functionality and health condition. A modified lateral force microscopy (mLFM) technique was developed on basis of the lateral force microscopy (LFM) to quantify viscosity through lateral force measurements applied on the sidewall of cell membranes. The resulting twist of the cantilever in mLFM is induced by the contact between sidewalls of tip and features on the sample. However, the measurement sensitivity of the mLFM requires improvement. This thesis focused on optimizing probe geometries and materials to improve the measurement sensitivity.

Probes (cantilevers and tips) with different geometries and material properties were proposed and their deformations in the mLFM force measurement were studied. The force measurement process, in which the tips contacted the sidewall of control samples, including a hard sample and a soft sample, was modelled by finite element analysis (FEA). This study calculated torsional spring constants and measurement sensitivities according to the data produced from FEA. The impact of various geometric parameters on the torsional spring constant and measurement sensitivity were presented and discussed. The optimal probe configuration and material for measurement sensitivity was found from the parameters tested in

this research. For the hard sample, the cantilever with a “T-shape” cross section and a tetrahedral tip made from graphite had the optimum measurement sensitivity. For the soft sample, the cantilever with a “T-shape” cross section and a conical tip with a 600 nm-radius sphere tip apex had the optimum measurement sensitivity. The reason for the difference in optimum probe combination for hard and soft sample was that the measurement sensitivity for hard sample was more susceptible to change in lever arm distance and measurement sensitivity for soft sample was more susceptible to the change in tip radius. The measurement sensitivity has been improved significantly on both the hard sample and soft sample compared to a DNP V-shaped probe.

CHAPTER 1. INTRODUCTION

1.1 Problem Statement

Due to the growing interest of nano-devices and nano-materials, the investigation of surface topography and mechanical properties at the nanoscale has driven the need for high precision force measurements. The scanning probe microscopy (SPM) has been widely used in the material property and surface study in the fields of physics, chemistry, electronics, biology, and medical application due to its nano-scale accuracy of force measurements and surface profiling (Eaton & West, 2010).

Cell membranes are biological membranes that consist of lipid bilayers and embedded proteins and separate the interior of the cells from the external environments. The viscosity of the cell membrane is a primary indicator of a cell's functionality and health condition and can be quantified by force measurements performed on the cell surface typically in the normal direction. A modified lateral force microscopy (mLFM) technique was developed on basis of the lateral force microscopy (LFM) to quantify viscosity though lateral force measurements applied on the sidewall of cell membranes (Hseu, 2015). mLFM and LFM techniques utilize the lateral twist of cantilevers to produce quantitative force data of the samples. The twist of cantilevers in LFM is caused by the friction force between tip apex and sample surface while the twist in mLFM is determined by the contact between sidewalls of tip and features on the sample.

The resolution and precision of LFM and mLFM are influenced by many factors simultaneously, including the sensitivity of piezoelectric scanner and photodiode, and the mechanical properties of cantilevers and tips. Among these factors, the mechanical properties of cantilevers and tips underpin the performance and versatility of LFM (Sader & Sader, 2003). Although some investigations on the mechanism of the LFM probe displacement have been done

to enhance the sensitivity of force measurement (Müller et al., 2006), the sensitivity of the mLFM force measurement technique can be improved by optimizing probe geometries and materials.

1.2 Research Problem

How can the measurement sensitivity of the mLFM technique be improved by probe configuration and materials optimization?

1.3 Scope

The cantilevers and tips play important roles in the accurate force measurements of LFM and mLFM. The design and geometry of cantilevers and tips have been studied to increase the measurement sensitivity of LFM. However, such investigation has not performed on mLFM since it was developed in 2015 (Hseu, 2015). This thesis investigated the configuration of mLFM probe to improve the measurement sensitivity from the geometries and materials of cantilevers and tips.

Cantilevers and tips with different geometries and material properties were proposed and their deformations in the mLFM force measurement technique were studied and compared. The force measurement process, in which the tips contact the sidewall of control samples was simulated by finite element analysis. The study developed fully parameterized models and led to the calculation of spring constants and measurement sensitivities. The configuration and material selection of cantilevers and tips with optimum measurement sensitivity was obtained.

1.4 Significance

The change in viscosity of cell membranes is considered as a significant indicator of the cellular functionality and health condition. A new AFM technique, mLFM was proposed to quantify the viscosity changes through measuring interaction forces between the tip and the sidewalls of the cell membrane. However, cantilevers and tips with higher measurement sensitivity are needed and have not been investigated. This study focused on improving the measurement sensitivity by optimizing the probe configurations and material properties. The probe configuration with the optimum measurement sensitivity will be manufactured in the future work to enhance mLFM in the force measurement performance on membrane structures and cells.

1.5 Assumptions

The following assumptions was made within this research:

1. The tips were assumed to be infinitely rigid and are elements with lumped-mass.
2. The vertical bending and lateral torsion of the planar cantilevers were assumed to be independent, which meant that there was no mechanical crosstalk and signal mixing between the two deflection modes. However, in practice, the coupling and nonlinear effects were observed when the LFM cantilevers are undergoing large deformation (Mitsuya, Ohshima, & Nonogaki, 1997).

1.6 Limitations

The following limitations were made in this research:

1. The finite element analysis was performed by SolidWorks Simulation Prime package. Thus, the accuracy and reliability of simulation results were limited to the capabilities

of the software. The limits of the SolidWorks simulation on nano-structures were noticeable that the SolidWorks simulation was not able to process displacement smaller than 100nm.

2. The diameter of the laser beams and location of laser spot on the cantilever in the optical lever detection system associated with the measurement sensitivity was not be considered due to the limitation of SolidWorks Simulation package. The twist angles were measured by tangential displacements in the deformed results.

1.7 Delimitations

The following delimitations was made in this research:

1. Only the pushing force method in the mLFM technique was investigated because it was validated by the researcher who developed it. The details of the force method were introduced in the section 2.4.
2. The whole process of the lateral ramp including attraction and retraction was not simulated. Only the interaction after the initial contact between the tip and the sample was investigated.
3. In the contact modelling of tips and samples, only a hard control sample with the elastic modulus of 66.3 GPa and a soft control sample with the elastic modulus of 2.97 MPa were simulated and studied. The silicon dioxide is the material of the Bruker calibration grid which was generic hard control sample used for the calibration in AFM and LFM. The soft sample Sylgard-184 Silicon Elastomer was chosen because it was widely used in the nonlinear deformation investigation of biomedical materials and biological membranes in mechanobiology (Hopf, Bernardi, Menze, Zündel, Mazza & Ehret, 2016).

1.8 Summary

The measurement sensitivity of the modified LFM technique was expected to be improved by optimizing the probe configuration. This chapter described the research problem, scope and significance. It also presented assumptions, limitations and delimitations, which guided the following investigation processes.

CHAPTER 2. REVIEW OF LITERATURE

2.1 Scanning Probe Microscopy

Scanning Probe Microscopy (SPM) is an umbrella name for a variety of techniques to provide high-precision force and high-resolution surface topography measurements at the nano-scale. Different SPM techniques utilize different probe-sample interactions while the probe is scanned across the sample to determine various information of the sample surface. Binning and Rohrer started the development of SPM with the invention of scanning tunneling microscopy (STM) in which the tunneling current was used as feedback to obtain topographical information and electrical measurements (G.Binning & Rohrer, 1982). STM has been improved since 1982 while new SPM techniques have been developed. The atomic force microscopy (AFM) was developed by Binning and Quate (G.Binning & Quate, 1986) where atomic forces between a tip and the sample surface were utilized to perform measurements. Compared with STM, the samples of AFM are not limited to conductive substance so that AFM is widely utilized in biological investigations. In 1987, Mate *et al.* (Mate et al., 1987) used an AFM to investigate atomic structure by measuring the sliding frictional force between the tip and sample surface, indicating the start of friction force microscopy (FFM) in microstructural characterization at nanoscale.

Other SPM techniques are useful characterization tools in nanotechnology, such as magnetic force microscopy (MFM), scanning capacitance microscopy (SCM), and scanning spreading resistance microscopy (SSRM). With the ability to detect nanoscale magnetic domains and characterize magnetic nanoparticles, MFM is applied in biomedical science such as magnetic hyperthermia treatment (Cordova, Attwood, Gaikwad, Gu, & Leonenko, 2014). SCM is utilized in nanoelectronics with the capability of mapping dopant profiles (Williams, 1999). SSRM can

achieve spatial resolution of five nanometers for detecting two-dimensional resistivity distribution in semiconductors (Wang et al., 2016).

2.2 Atomic Force Microscopy

The AFM, a sub-field of SPM technique, is capable of mapping the surface topography and performing force measurements of insulators on an atomic scale (G.Binning & Quate, 1986). AFM utilized the tip-sample interaction to "feel" the features on the surface rather than "looking" to determine surface information (Morris, Kirby, & Gunning, 2014). The schematic in Figure 2.1 represents the main components of an AFM.

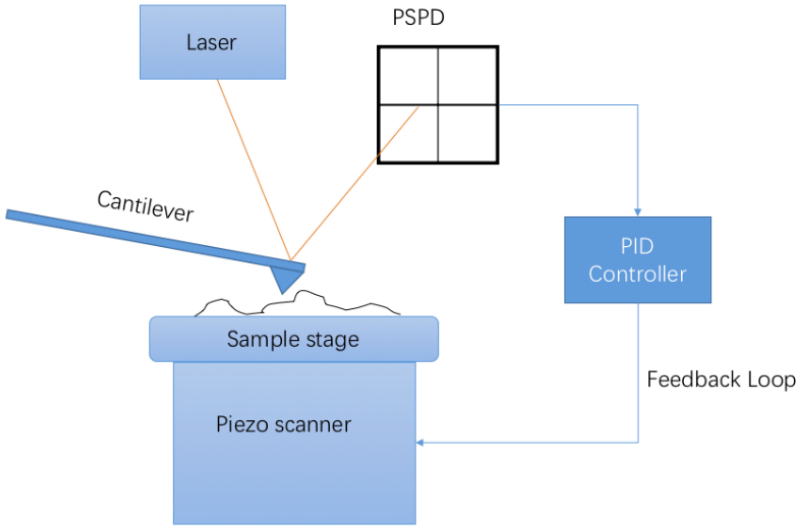

Figure 2.1 The simplified Schematics of an AFM.

A typical AFM system consists of a computer interface, a controller, a scanning head with probe, a sample stage with a piezoelectric transducer and various environment isolations. The probe of AFM is a cantilever with one end fixed and a small tip attached to the free end. A laser beam is focused at the end of cantilever and reflected off to the position sensitive

photodiode (PSPD). As the tip is scanning across the sample surface, the change in the cantilever deflection is detected by a photodiode detector. When the cantilever bends because of the height change on the sample surface, the reflected laser spot will have an angular displacement which will be displayed on the PSPD. A four-quadrant photodiode was found to be the most effective optical detection method (Weisenhorn, Hansma, Albrecht, & Quate, 1989) where the signal intensity difference between the top two quadrants and bottom two quadrants will be compared to obtain the surface topography information. The scanning motion and nanoscale positioning in three dimensions are controlled by piezoelectric scanner located under the sample stage, which expands and contracts proportionally to an applied voltage. The controller receives the commands from user interface software to control the system and simultaneously converts raw data obtained from the scanning to processed data on the software. In order to eliminate the influence of acoustic and mechanical vibration, the AFM is located on a floating table and electromagnetic shielding are applied during the scanning process.

There are many modes of AFM, two of which are contact mode and tapping mode. In contact mode AFM, the tip will remain on the sample surface as it travels across the surface in a raster scan. To maintain the force constant on the surface applied by the tip, a deflection set-point is set. A proportional–integral–derivative (PID) feedback loop is utilized to maintain the constant force between the cantilever and sample surface by vertically moving the probe at each (x,y) data point.

In tapping mode, the cantilever is excited with an external piezo element and oscillates at or near its resonance frequency. As the tip get closer to the sample surface, the amplitude of cantilever's oscillation decreases. The height of cantilever will be adjusted by the z-piezo to maintain the constant oscillation amplitude throughout the scanning process. Then the

adjustment of z-piezo is recorded and converted to the AFM tapping force curves and images. Tapping mode is most frequently used in ambient and fluid conditions because tips and sample surface are close enough to detect short-range forces while it can also prevent the tip from sticking to the surface (Zhong, Inniss, Kjoller, & Elings, 1993).

2.3 Force Curves of Atomic Force Microscopy

Mechanical properties of samples can be quantified by measuring the atomic forces between the AFM tip and the sample surface. The forces will vary with different interactions between the tip apex and a cluster of atoms on the sample surfaces so different types of forces are encountered. The forces include the van der Waals force, the electrostatic force, the capillary force, the adhesive force, and the double layer force.

In contact mode AFM, the forces between the tip and the sample surface are measured by using the vertical ramp function of the AFM system (Butt, Capella & Kappal, 2005). In the vertical ramp, a force-distance curve is obtained by pushing the tip onto the sample surface at a chosen location and then retracting the tip from the surface. A typical force-distance curve performed on a rigid surface in air is illustrated in Figure 2.2 (Digital Instrument, 1996).

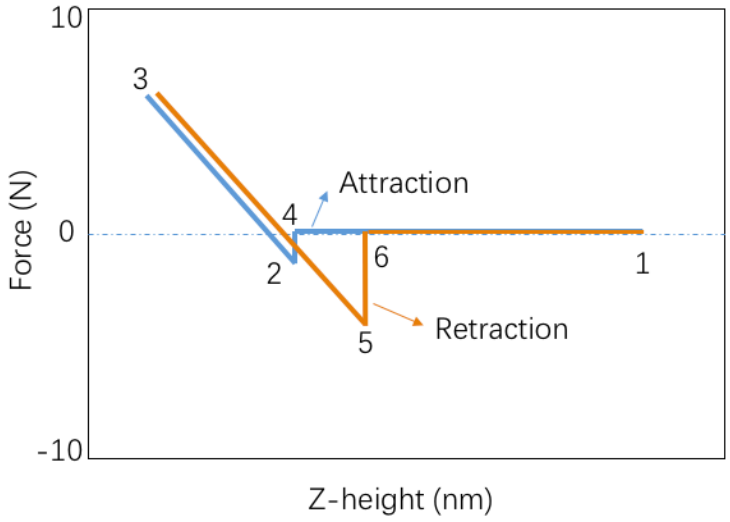

Figure 2.2 A typical contact mode AFM force curve on a hard sample in air (Digital Instrument, 1996).

At the beginning (point 1), the force is zero when the tip is approaching the sample surface until it is close to the surface and begins to deflect downwards because of the attractive force between the sample surface and the tip (point 2). The force at point 2 is known as the snap-to force and represents the tip-surface attraction. The cantilever deflects up as the tip keeps lowering and pushes into the sample surface (point 2-3). When the tip begins to retract away from the sample surface, the amount of cantilever deflection upwards decreases (point 3-4). The tip is pulled down with the sample surface and the cantilever deflects downwards because of the attractive force between the tip and surface. The force is known as pull-off force (point 5). As the retraction continues, the attractive force is broken off, the cantilever will go back to the original position (point 5-6). The typical force curves of attraction and retraction on hard surfaces in air are linear. Figure 2.3 shows an example of force curves performed on soft samples. The nonlinear regions indicating the hysteresis when the tip is coming into contact with the sample surface during attraction and retraction (Thomas, Burnham, Camesano & Wen, 2013). The hysteresis phenomenon results from the viscoelasticity of the cell membrane and occurs when

the cell reacts to the tip differently from the attraction to the distraction process (Mustata, Ritchie & McNally, 2010).

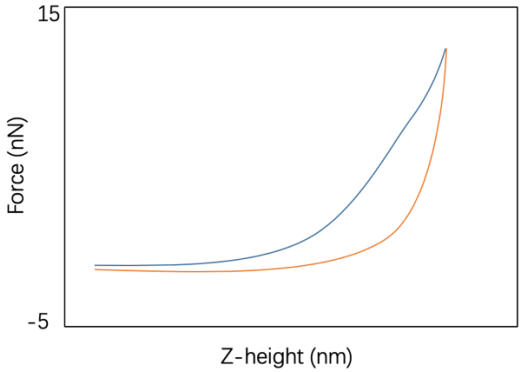

Figure 2.3 A typical force curve of neural cell body showing hysteresis and non-linear nature (Mustata, Ritchie & McNally, 2010).

2.4 Lateral Force Microscopy

Lateral Force Microscopy (LFM), also known as Friction Force Microscopy (FFM) first introduced in 1987 (Mate et al., 1987), is a method using contact mode AFM where the cantilever scans across the sample surface to perform surface friction force measurements. The principle of LFM is similar to contact mode AFM. The torsion of cantilever caused by the friction force acting on the tip is detected by the laser focused on the end of cantilever and reflected on to a photodiode. However, in LFM, the friction force between the tip and the sample surface leads to the torsion of the cantilever when it moves horizontally across the sample, so the signal difference between the left two and right two quadrants of the PSPD are compared.

The torsion of the cantilever is determined by the frictional coefficient of the surface, the height of features on the sample surfaces, and cantilever spring constant (Bhushn & Marti, 2017). LFM is utilized to study both the topography and tribology of sample surface, such as

mapping the surface topography (Sadaie et al., 2006), chemical composition (Frisbie, Rozsnyai, Noy, Wrighton, & Lieber, 1994), molecular organization (Shen et al., 2014) and the mechanical behaviors (Dinelli, Buenviaje, & Overney, 2000) of the sample surface.

2.5 Modified LFM technique

A mLFM technique was developed to study a cell membrane's viscosity. This technique intended to develop a new lateral force curve using the SPM manipulation software NanoMan. The pushing force method shown in Figure 2.4 was performed for validation of lateral ramp produced by modified LFM technique (Hseu, 2015). The AFM tip was lowered and moved close to the sidewall of the features on surface. Then with adjustment of tip's moving path and rate, the tip was pushed against the sidewall leading to the twist of cantilever, which was measured and converted into lateral ramp (presented in Figure 2.5). Similar to the vertical ramp force curves, the snap-to force and the pull-off force during the attraction and retraction can also be identified on the lateral ramp force curves on a hard and a soft sample (Figure 2.5 and 2.6). The hysteresis effect of the artificial membrane was observed in the lateral ramp shown in Figure 2.6.

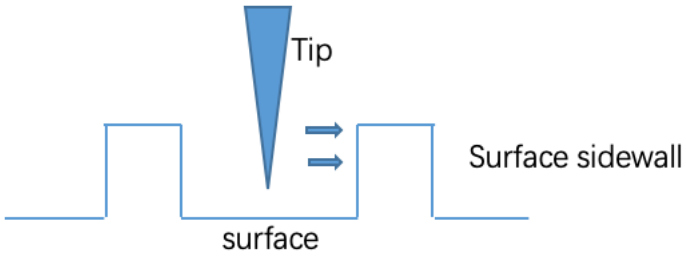

Figure 2.4 The pushing force method of mLFM technique.

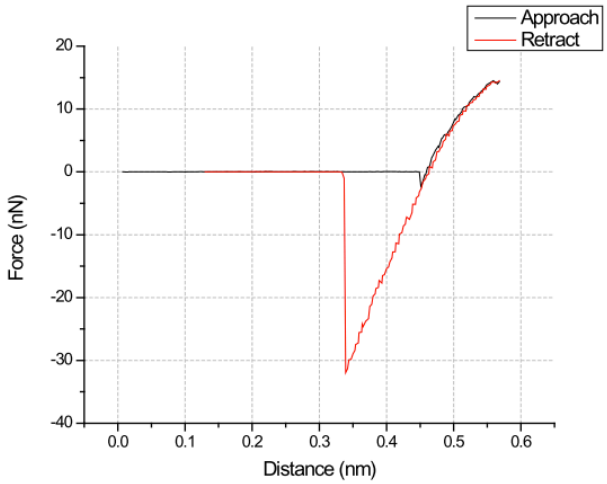

Figure 2.5 A lateral ramp curve on a hard sample in air obtained by mLFM technique (Hseu, 2015).

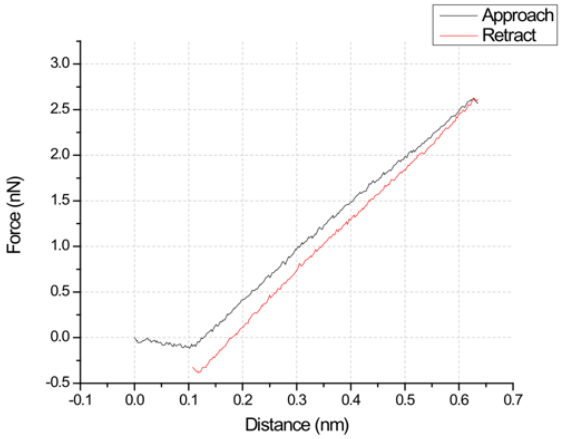

Figure 2.6 A lateral ramp curve on a soft sample in air obtained by mLFM technique (Hseu,2015).

The pushing force method was validated on a hard-flat surface, a Bruker silicon dioxide calibration grid, in air using both a DNP-S tip and a colloidal tip (Hseu, 2015). Lateral ramp was also performed on a sylgard-184 silicon elastomer and indicated that the technique was also applicable to soft samples. However, cantilevers and tips with new configuration and material

properties were to be developed in order to improve the measurement sensitivity of the modified LFM technique.

2.6 Probe-cantilevers and tips

2.6.1 Contact mode AFM cantilevers and tips

The cantilever and tip assembly shown in Figure 2.7, often referred to as the probe, is one key to resolution and precision of AFM measurements. In the scanning process, the tip governs the interaction with the sample surfaces and the resulting elastic deformation of the cantilever is recorded as well as interpreted into force data. The early AFM cantilevers were a piece of thin gold foil (G.Binning & Quate, 1986) or a tungsten wire (Mate et al., 1987). These days, two basic geometries for cantilevers are most widely employed to generate high precision mapping for the surface: rectangular and triangle (also referred to V-shaped). Different types of cantilevers with diverse mechanical properties, including stiffness and resonant frequency, are designed for different operation modes—contact mode and tapping mode. In contact mode AFM, a cantilever with low spring constant is preferred in order to increase the measurement sensitivity (Cleveland, Manne, Bocek, & Hansma, 1993).

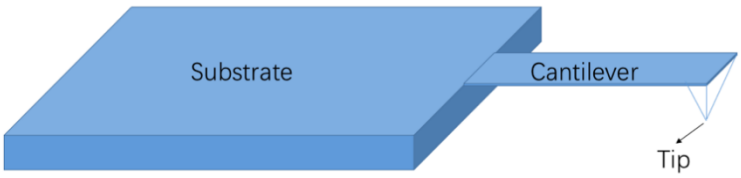

Figure 2.7 An LFM probe consists of a cantilever with a tip attached on a substrate.

The cantilever's spring constant determines the stiffness of the cantilever affecting its ability to bend and twist under different forces (Hutter & Bechhoefer, 1993). Irrespective of the shape of cantilever, the relationship between the force applied to the sample surface and the bending of cantilevers follows Hooke's Law:

$$F = -ks \tag{2-1}$$

where k is the spring constant of the cantilever and s is its displacement.

The normal spring constant of a cantilever with rectangular cross section was given by (Munz, 2010)

$$k_n = \frac{Et^3w}{4L^3} \tag{2-2}$$

where *E* is the elastic modulus, *t* is the thickness, *w* is the width, and *l* is the distance from the fixed end of the cantilever to the position where the tip is located. According to the Eq. (2-2), the spring constant increases with the cantilever thickness but decreases with the length of cantilever.

The normal spring constant of triangular cantilever was given by (Tortonese, 1997):

$$k_n = \frac{Et^3wb}{2b\left(L_1^3 - L_2^3\right) + 6wL_2^3} \tag{2-3}$$

where *E* is the elastic modulus, *t* is the thickness, *w* is the width, and the other parameters are presented in Figure 2.8 below.

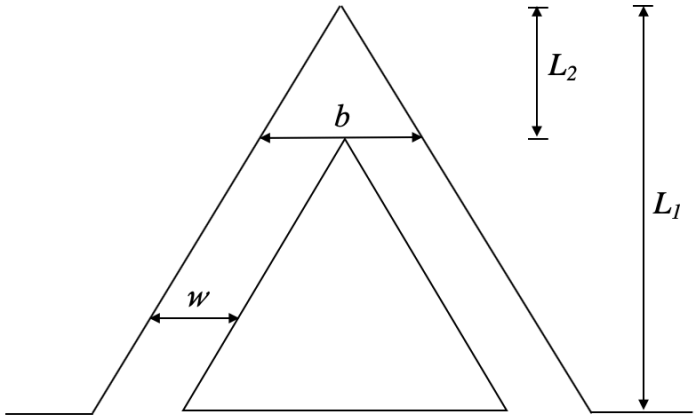

Figure 2.8 Geometric parameters of a triangular cantilever for normal spring constant.

Lengths of the cantilever also affect the resolution of AFM in addition to spring constant when optical beam detection is employed (Morris, Kirby, & Gunning, 2014). The angular displacement of the reflected laser beam is inversely proportional to the cantilever length, which indicates a longer cantilever leads to a smaller laser beam deflection compared to a shorter cantilever. Consequently, the laser spot has a smaller movement on the photodiode, producing a smaller output signal for the control loop. Thus, the long cantilevers are preferred for imaging rougher samples, because the shorter cantilevers may result in a range of motion too large for the PSPD.

Modern cantilevers of AFM are mostly made from silicon, silicon nitride, quartz, diamond and metallic materials. The back surface of the cantilever is usually coated with a metallic thin layer, such as gold or aluminum to improve the reflectivity to the laser beam, especially in liquid medium where the reflectivity of silicon nitride is much reduced (Cappella & Dietler, 1999).

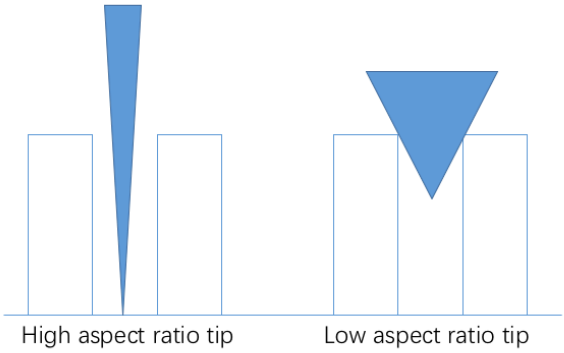

Figure 2.9 Illustration of tips with high and low aspect ratio.

Tips with high and low aspect ratio are illustrated in Figure 2.9. Tips with lower aspect ratio are used to image flatter samples, and tips with higher aspect ratio are used to image more rough surfaces because of the ability to reach deep gaps (Weihs, Nawaz, Jarvis, & Pethica, 1991). The most common tip shapes are pyramidal, conical and tetrahedral. The tip sharpness is defined as the curvature radius of the sphere at the tip apex. The tip sharpness is different from the aspect ratio in definition since tips can possess diverse sharpness when their aspect ratios remain the same as demonstrated in the Figure 2.10. Although the aspect ratios are the same in the Figure 2-10 (a) and (b), the tip in (b) has smaller radius at the tip apex than the one does in the (a), producing AFM images with higher lateral resolution (Tortonese, 1997). Currently, wet anisotropic etching and dry reactive ion etching technologies have been utilized to produce tips with curvature radius of several nanometers (Li, Xie, Xue & Wu, 2013). In reality, specific sharpness of a tip is unknown and must be determined by scanning or transmission electron microscopy (Tortonese, 1997). Sharp tips become dull due to wear or damage through use.

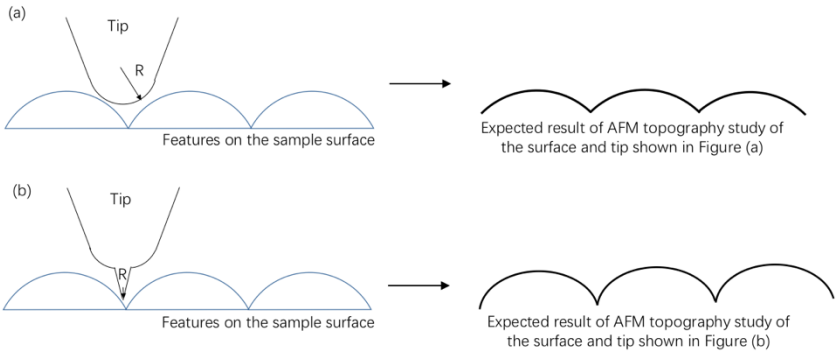

Figure 2.10 Illustration of tips with the same aspect ratio and different curvature radii (sharpness) along with the corresponding AFM image profiles: (a) shows a tip with larger curvature radius and lower sharpness; (b) a sharpened tip with smaller curvature radius.

Modern AFM tips and cantilevers are made by micro-fabrication techniques, such as lithography photo-masking, etching and vapor deposition. The selection of tip material is similar to the cantilevers and depends on the application as well as the purpose of the AFM scanning. The tip apex can be functionalized with other molecules to create specific probes and sensors to detect and characterize certain features on the sample surface (Morris, Kirby, & Gunning, 2014).

2.6.2 LFM cantilevers and tips

Geometries and materials of cantilevers and tips used in LFM are similar to those used in contact mode AFM. However, the off-plane displacement in the lateral direction of the cantilevers is recorded and interpreted into force data. Thus, the torsion of cantilevers is important. Torsional spring constant (k_θ) of LFM was defined by the torque (T) and the rotation angle (θ) about the major axis (Sader, 2003) in a similar format as the Hooke's Law in Eq. (2-3),

$$k_\theta = \frac{T}{\theta} \tag{2-4}$$

The torsional spring constant of a homogeneous rectangular cantilever was given by (Munz, 2010)

$$k_\theta = \frac{Gwt^3}{3L} \tag{2-5}$$

where G is the shear modulus of the cantilever material, t is the thickness, w is the width, and L is the distance from the fixed end of the cantilever to the position near its free end where the tip is located.

The analytical expression for V-shaped cantilevers was more difficult to derive. Neumeister and Ducker (Neumeister & Ducker, 1994) subdivide a V-shaped cantilever into a triangular plate and two prismatic beams and introduced a closed-form expression for the torsional stiffness as shown in Eq.(2-6).

$$k_\theta = \frac{Et^3}{3(1+\upsilon)}\left(\frac{1}{\tan\alpha}\log\frac{w}{d\sin\alpha} + \frac{L\cos\alpha}{w} - \frac{3\sin 2\alpha}{8}\right)^{-1} \tag{2-6}$$

where the E is the elastic modulus of the cantilever material, t is the thickness, w is the width, υ is the Poisson's ratio of the cantilever material, and the other parameters are presented in Figure 2.11.

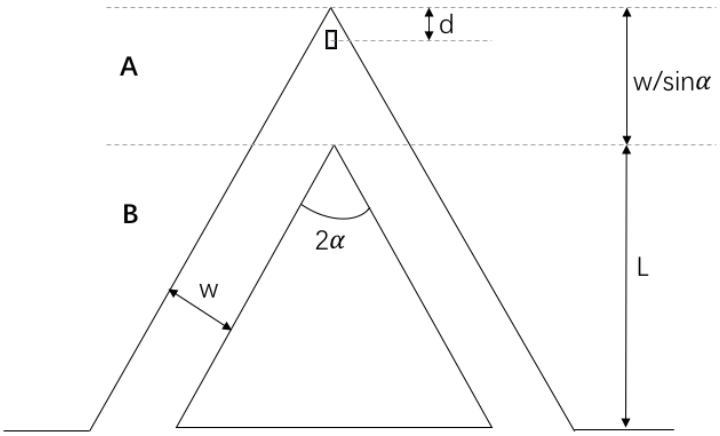

Figure 2.11 The principle geometric parameters of V-shaped cantilevers: a triangular plate (A) and two prismatic beams (B).

Rectangular cantilevers are less susceptible to torsional motions or twisting of the cantilevers while scanning compared with triangular cantilevers (Sader & Sader, 2003). Sader

(Sader, 2003) pointed out that lateral resistance is independent of rigidity of the cantilever, whilst dependent on the geometry, Poisson's ratio, the imaging tip height and the load position.

Special cantilevers have been designed particularly for LFM to increase measurement accuracy (Fukuzawa et al., 2006; Reitsma et al., 2011; Amakawa et al., 2012). For instance, a micro-fabricated T-shaped hammerhead cantilever as shown in Figure 2.12 was proposed to facilitate precise optical lever system calibration for cantilever flexure and torsion, enabling friction measurements by LFM (Reitsma et al., 2011). The greatly increased precision of torsion sensitivity was achieved by the combination of two factors: First, a longer lever-arm allows for a larger number of pivot measurements to be used to determine the result. Second, the hammerhead wings leading to longer moment arms decreases the relative uncertainty of lever-arm length determination and increases signal-to-noise. Finite element analysis predicted that when using the prototype cantilevers in lateral force measurements, the systematic measurement error is less than 3%. The researchers also proposed potential solutions to decrease the errors, including reducing head deformation, emphasizing the rotations closer to the fixed-end base to the cantilever and reducing wing flexure by using shorter lever-arms for pivot loading.

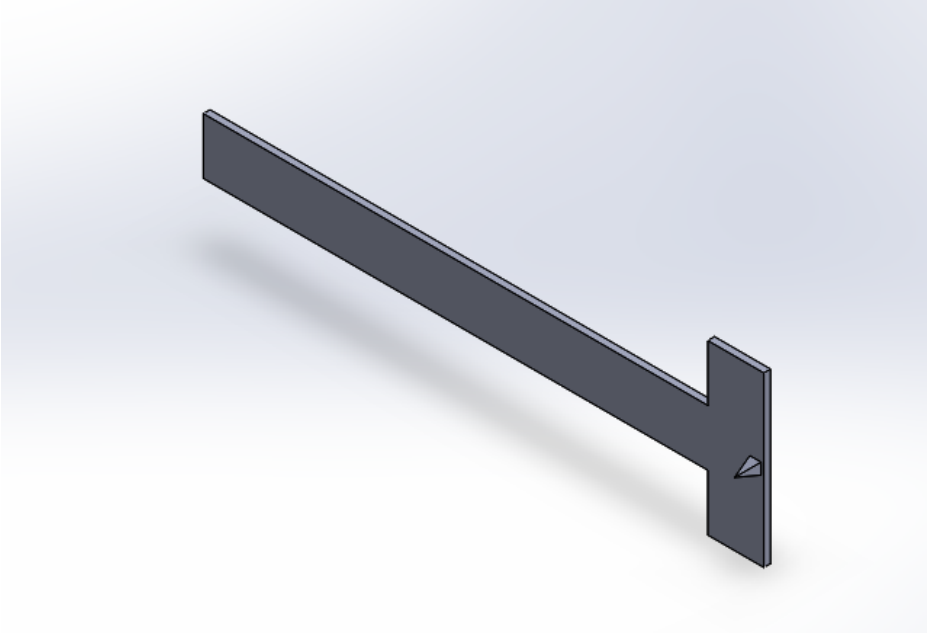

Figure 2.12 The illustration of prototype hammerhead cantilever chip (Reitsma et al., 2011).

2.7 Force measurements on cells

The understanding of cell mechanics is essential because the mechanical properties of cell are significant factors and indicators of cellular health condition and functionality. Cells are highly dynamic and change mechanical properties due to internal and external stimuli, such as aging, pressure or diseases (Kasza et al., 2008). Cells are observed to have both elastic and time-dependent responses to deformation, which means they have elastic and viscous characteristics (Moeendarbary & Harris, 2014). Thus, cells are referred as viscoelastic materials. To understand a cell's form and function, the elasticity and viscosity need to be quantified.

Measurements of cellular elasticity and viscosity entail the quantification of cellular deformation in response to an applied force, which is challenging due to the size of cells and pliability of cells (Kasza et al., 2008). The force measurements have been conducted on cells by researchers using various techniques thanks to the development of nanofabrication and piezoelectric ceramics (Moeendarbary & Harris, 2014). Laser optical tweezers (Dai & Sheetz,

1995) was utilized in investigating viscoelastic behavior of neuronal growth cone membranes at nanometer level. Viscoelastic moduli of living cells were quantified by the method of particle tracking microrheology (PTM) with high spatiotemporal resolution (Tseng, Kole, & Wirtz, 2002). Traction force microscopy (TFM) was a force sensing technique used to investigate cell spreading, migration and mechanical properties in living neuronal growth cones (Koch, Rosoff, Jiang, Geller, & Urbach, 2012) and filopodia (Chan & Odde, 2008). Atomic force microscopy (AFM) is also used to measure elasticity of various cells such as endothelial cells (Mathur, Collinsworth, Reichert, Kraus, & Truskey, 2001), living neurons (Mustata, Ritchie, & McNally, 2010). A standardized nanomechanical AFM procedure (SNAP) to measure elasticity of cells was developed involving calibration methods and data acquisition (Schillers et al., 2017). This SNAP ensures measurement of high consistency and accuracy independent of laboratory, equipment and operators by precisely calibrating the vertical deflection sensitivity of cantilevers. The values for the cellular young's modulus typically range from tens of kilopascals to several hundred pascals and the viscosity is about several hundred pascal-seconds (Moeendarbary & Harris, 2014).

2.8 Finite Element Analysis

It is difficult to find closed-form or analytical solution of some practical engineering problems when complex geometries, multiple materials, complicated boundary and initial conditions are involved. Thus, numerical methods, such as finite element analysis (FEA) are utilized to solve complicated problem (Pidaparti, 2017). FEA is a popular numerical method applied in the design analysis of mechanical (Pidaparti, 2017), aerospace (Xu, Chen, Men & Sun,2018), biomedical (Hatami, 2019), and electrical systems (Salon, 1995), which predicts the behavior of a product subjected to loads. In FEA, the geometry of the designed product is

discretized into small elements at nodes and analyzed for functional performance by applying boundaries as well as load conditions. FEA is cost saving and time saving in the design cycle while creating reliable and better-quality designs.

FEA has been used to investigate the mechanics of nanostructures including SPM cantilevers by many researchers. Nuemeister and Ducker (Neumeister & Ducker, 1994) proposed simple equations for the torsional stiffness of V-shaped cantilevers and demonstrated good agreement between the equations proposed as shown in Eq. (2-5) and (2-6) and Finite Element (FE) modelling results. Hazel and Tsukruk (Hazel & Tsukruk, 1999) measured the normal and lateral spring constants of composite Si_3N_4-Au cantilevers effectively using a combination of FEA and resonant frequency measurements. FEA was utilized to investigate the compressive, tensile and bending stress analysis of nanobeams with different geometries, materials and loading conditions. Load-displacement curves from a bending experiment using AFM were plotted with the prediction curve obtained from modelling for comparison. It was observed that the nanobeam follows an elastic behavior in the actual experiment, therefore the elastic model used in the FEM is justified (Bhushan &Agrawal, 2002). A fully parameterized FE model of V-shaped cantilevers with different geometries was utilized to calculate the different force constants and detection sensitivities in the three spatial directions (Müller et al., 2006). This investigation focused on the linear limits and nonlinearity of the cantilevers when they were submitted to incremental deformations respectively. Linear regime extended up to 10 nanometers of tip displacement in the lateral direction and a strong nonlinearity was observed beyond this deformation. However, this study excluded the modeling of the contact between tips and samples. Choi and Gethin (Choi & Gethin, 2009) explored the sensitivity and generic response of a simple beam and a V-shaped cantilever incorporating a colloidal tip in both normal and lateral

directions. The results suggested that material properties of cantilevers and the height, size, and fixity area of the colloidal tip affected the deflection angles. The FE contact modeling revealed three generic stages of lateral response between tips and sample surfaces comprising of twisting, bending and finally sliding. Although many FE studies have been done on the deformation of AFM cantilevers and tips, the modified LFM technique has not been investigated using FE modeling.

2.9 Summary

This chapter reviewed a brief history and introduction of scanning probe microscopy, atomic force microscopy and lateral force microscopy. The mLFM technique as well as the investigation and development in LFM probe, including the cantilever and tips were introduced. Different force measurement techniques on biological materials were briefly presented. The application of FEA on the study of LFM probe, which was utilized as the simulation tool in this research, was also discussed. The next chapter described the methodology that was used in the research process.

CHAPTER 3. RESEARCH METHODOLOGY

This chapter discussed the methodology employed for improving the measurement sensitivity of the mLFM technique by optimizing the geometric configuration and materials of probes. The research approach, design criteria, instrumentation, and data analysis methods were outlined in this chapter. The investigation was achieved by building a parameterized FE modeling of the cantilevers and tips with different geometries and materials to identify the optimum sensitivity and the corresponding probe materials and configurations.

3.1 Research Approach and Variables

The methods used in this study were designed to understand the relationship of the following independent variables and dependent variables. Consequently, the probe configuration and material properties with the optimum measurement sensitivity was identified by FEA.

1. Independent variables:

- Cantilever geometry: Different shape of cantilevers, other than normal rectangular and V-shaped cantilevers with varied cantilever length, width and thickness were studied.
- Tip geometry: Tips with different geometries with varied tip height, width, and apex radius were studied. The position of the incorporating tip relative to the cantilever also influences the sensitivity of measurement in modified LFM.
- Cantilever materials: The type of materials determines the mechanical property, which have a significant impact on the response of probe to the lateral loads. Thus, diverse materials with varied elastic modulus, Poisson ratio, density and yield strength were investigated.

2. Dependent variables:

- The torsional spring constant in this study was defined as the ratio of the torque applied on the cantilever to the twist angle of the cantilever. The decrease in torsional spring constant leads to the increment in cantilever flexibility and thus, measurement sensitivity. Therefore, the cantilever design with the lowest torsional spring constant was identified and selected for the tip investigation.
- The measurement sensitivity in this study was defined as the ratio of the twist angle of the cantilever to the lateral force applied to the tip. The measurement sensitivity elucidates the performance of the entity of cantilevers and tips. The angular displacement of the cantilever was represented by the angular displacement calculated by the tangential displacement of the cantilever. The tip design that resulted in the optimal measurement sensitivity was identified.

3.2 FEA Software

The FE modelling and analysis was accomplished using the commercial software SolidWorks, a powerful computer-aided design and simulation engineering software, from Dassault Systèmes. The model was established by designing, building and assigning dimensions to the geometry components. Then the FE simulation was performed by the Simulation Prime package. After applying appropriate boundary conditions and external loads, the meshing was created. Then the solver calculated the results and generated the result visualization for post-processing and analysis. The following sections describe the design and simulation procedures.

FEA set-up starts with applying material properties to all the components or the assemblies of interest. Every part and body need to be assigned to a certain material with

mechanical and thermal properties. Mechanical properties necessary for the FE simulation include the elastic modulus, the Poisson's ratio, the mass density and the yield strength. SolidWorks has a built-in material database, but users are also free to customize new materials to the database or edit properties of existing materials.

It is essential to simulate the working environment of the model by applying appropriate fixtures, loads and contact conditions. Various types of fixture can be applied to the bodies for defining boundary constraints, including fixed geometry, roller/slider, fixed hinge, and foundation bolt. External force, torque, pressure, prescribed displacement and thermal effects can be applied to parts in order to simulate the realistic working and loading conditions. SolidWorks also provides varieties of contact options to define the ways parts interact with each other including no penetration, bonded, shrink fit, and allow penetration.

Meshing is a crucial part of the FEA simulation set-up. The program will subdivide the geometric models into small pieces of simple shapes called elements connected at common points called nodes. This process is called meshing and determines the accuracy of the solution. The program will apply appropriate meshing type to bodies based on their structures, however, the users are able to customize the meshing patterns as well. In general, the finer the mesh, the better the accuracy and longer time the simulation would take.

The simulation runs to solve the model after the set-up accomplished, which is described by a group of algebraic equations. Data, figures, plots, and animations on resultant stress, strain, and displacement in multi-dimensions are produced for further data analysis and conclusion.

3.3 Design Criteria

Design criteria followed in this study was introduced in this chapter. The design criteria included the configuration designs and material properties of the cantilevers and tips to be investigated in the simulation.

3.3.1 Cantilever geometry design

Cantilevers with four diverse geometries (A-D) were proposed to decrease the torsional spring constant and improve the measurement sensitivity as illustrated in Figure 3.2 to Figure 3.5. The torsional force constant was calculated by FEA to identify the cantilever geometry and corresponding geometric parameters with the lowest stiffness. The geometric parameter ranges of the corresponding designs that was studied were listed in the Table 3.1 to Table 3.4. For model validation and comparison, a DNP probe from Bruker was utilized as the control set whose configuration and information are illustrated as Figure 3.1.

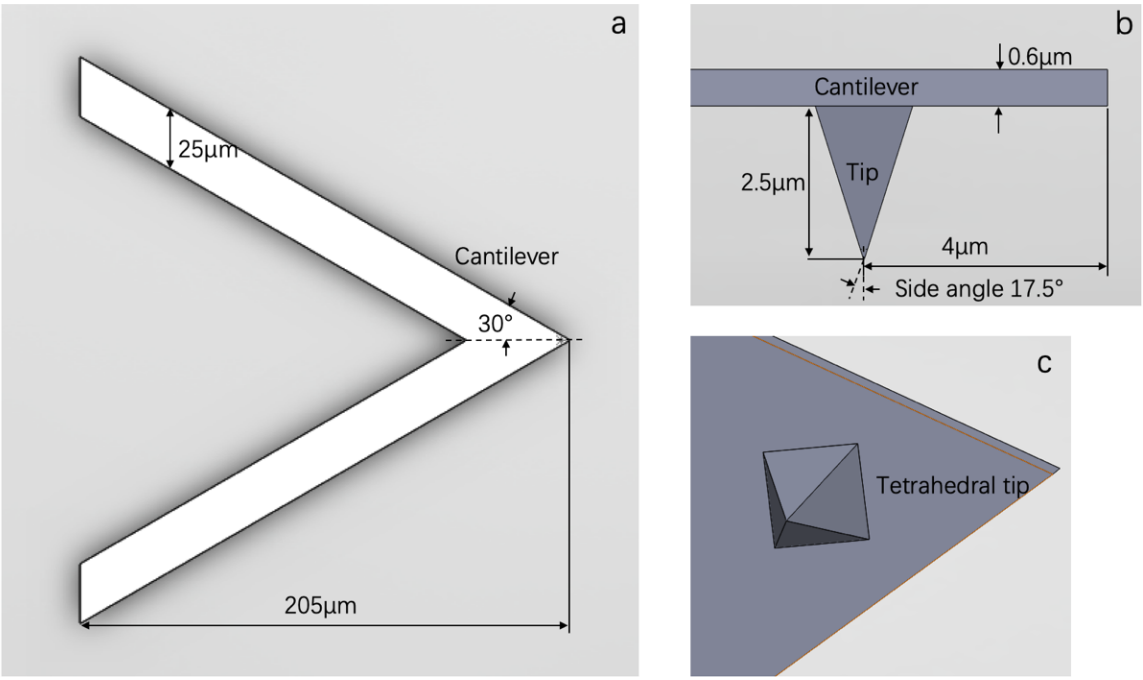

Figure 3.1 The configuration and dimensions of DNP probe: (a) the top view of the DNP cantilever; (b) the side view of the free end of the cantilever and the tip attached; (c) the bottom view indicating the tetrahedral tip.

For each design, the torsional force constants of cantilevers made from the following materials were calculated: Boron Nitride (BN), graphite, and Nickel-Titanium martensitic alloy (Ni-Ti). These materials have low elastic moduli and shear moduli compared to common cantilever materials such as silicon nitride or silicon. Also, cantilevers and tips at nano-scale or micron-scale can be made from these three materials by microfabrication or focused ion beam. The detailed mechanical properties of these materials are demonstrated in Table 3.5 (CES EduPack 2018, 2019). The torsional deformation of the materials is dominated by the shear modulus which can be expressed by the ratio of elastic modulus to the Poisson's ratio. Thus, materials with low elastic modulus and high Poisson's ratio were desired to decrease the torsional spring constant of cantilevers.

According to the analytical equations introduced in the Section 2.6.2, the geometric dimensions, length, width, and thickness significant influence the torsional spring constant of common cantilevers if the material properties are fixed. Designs in this thesis were proposed based on this general rule that also applies to uncommon shapes of cantilevers. The cantilever design A consisted of two thin wires supporting a small beam block to reduce the total thickness and width as shown in Figure 3.2. The beam block connected the bottom of the tip and also provided enough space for the reflection of the laser in the optical detection system. Table 3.1 demonstrates the testing ranges of all the geometric parameters to investigate the effects of the parameters on the torsional spring constant.

Table 3.1 The geometric parameters of the cantilever design A and testing ranges

Parameter	L1 (μm)	L2 (μm)	w1 (μm)	w2 (μm)	t (μm)	d (μm)
Range	200-450	0.2×L1	15-40	0.8×w1	0.6-0.8	0.5t

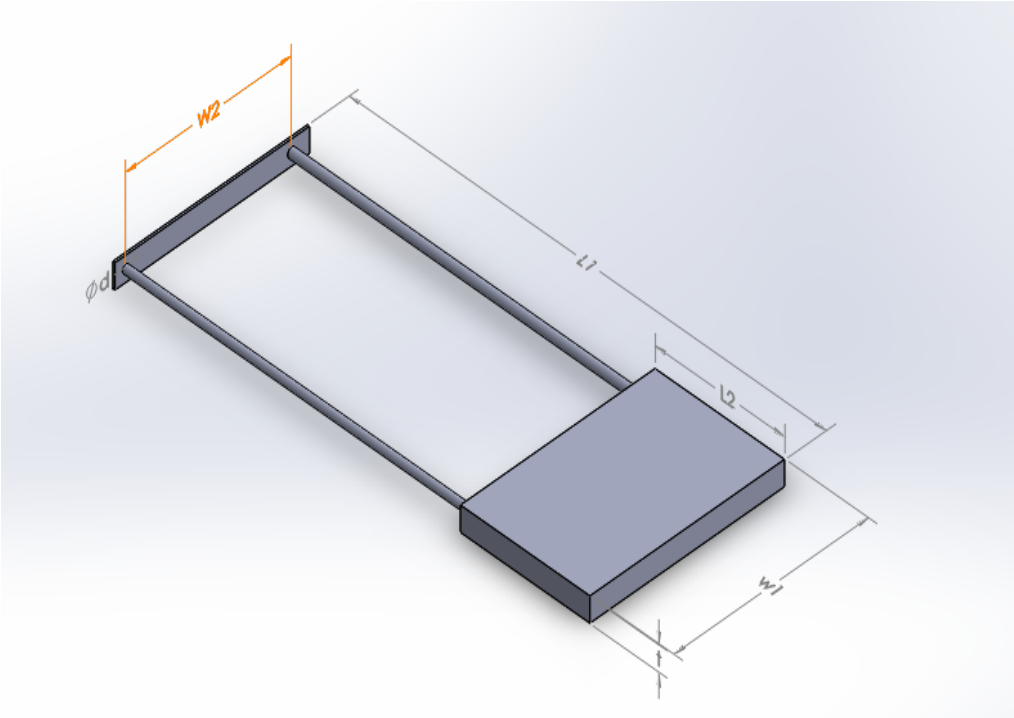

Figure 3.2 Geometric model of cantilever design A with dimension annotations.

Cantilever design B was proposed on the basis of a normal V-shape cantilever whereby the width was reduced to decrease the torsional spring constant of the cantilever as shown in Figure 3.3. The triangle space at the free end of the cantilever was remained for placing laser sport. The effect of half angle α with the range between 15° and 30° on the torsional spring constant were also studied. The effects of the geometric parameters on the torsional spring constant of cantilever design B were investigated and Table 3.2 demonstrates the ranges all the geometric parameters tested.

Table 3.2 The geometric parameters of the cantilever design B and testing ranges

Parameter	L1 (μm)	L2 (μm)	L3 (μm)	w1 (μm)	w2 (μm)	$\boldsymbol{\alpha}$ (°)	t (μm)
Range	200-450	0.4×L1	0.8×L1	15-40	0.5×w1	15-30	0.6-0.8

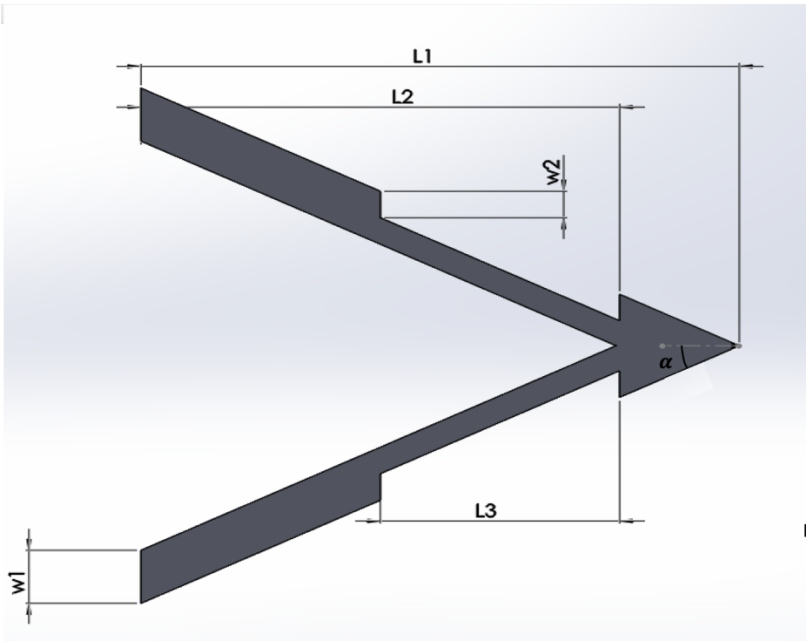

Figure 3.3 Geometric model of cantilever design B with dimension annotations

The cantilever design C was proposed based on the hammerhead cantilever prototype introduced in the Section 2.6.2. Accurate lateral force calibration can be accomplished and

meanwhile the spring constant was reduced because of the decrease in width as demonstrated in Figure 3.4. How the length of wings would affect the torsional spring constant was also explored in this study. The effects of the geometric parameters on the torsional spring constant of cantilever design C were investigated and Table 3.3 demonstrates the ranges of the geometric parameters to be tested.

Table 3.3 The geometric parameters of the cantilever design C and testing ranges

Parameter	L1 (μm)	L2 (μm)	L3 (μm)	w1 (μm)	w2 (μm)	w3 (μm)	t (μm)
Range	180-405	$\frac{1}{9}$L1	0.8×(L1+L2)	45-120	$\frac{1}{3}$w1	0.8×w2	0.6-0.8

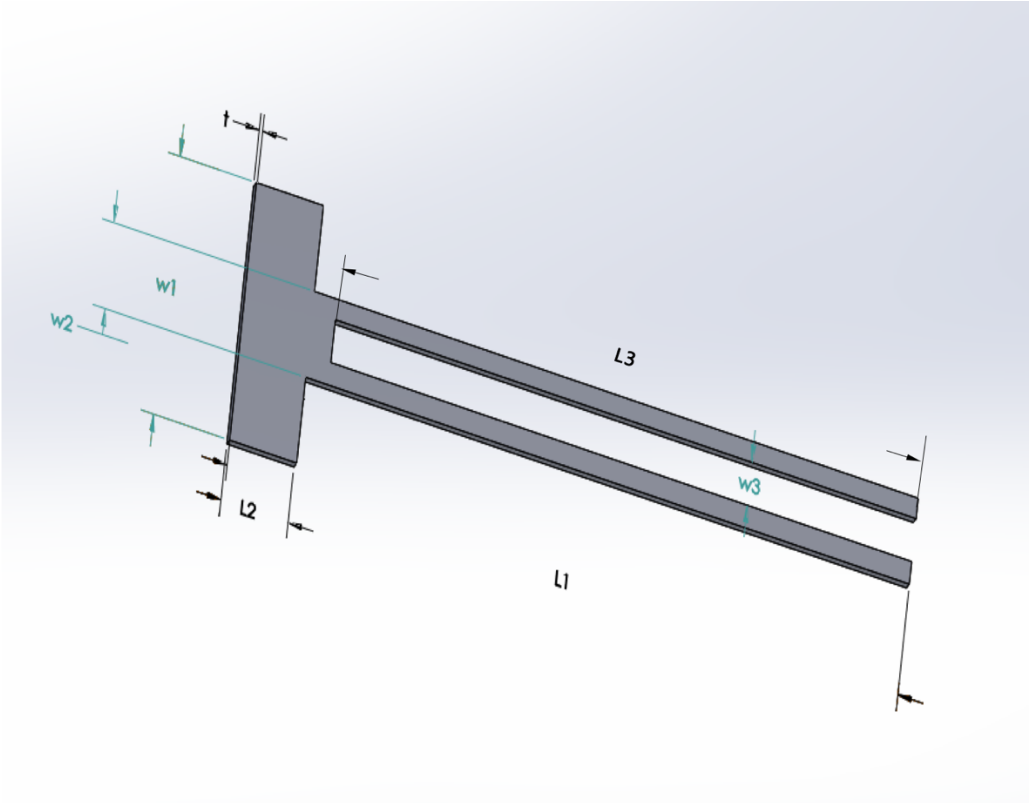

Figure 3.4 Geometric model of cantilever design C with dimension annotations.

Table 3.4 The geometric parameters of the cantilever design D and testing ranges

Parameter	L (μm)	w1(μm)	w2 (μm)	t (μm)	h (μm)
Range	200-450	15-40	2-12	0.6-0.8	5-15

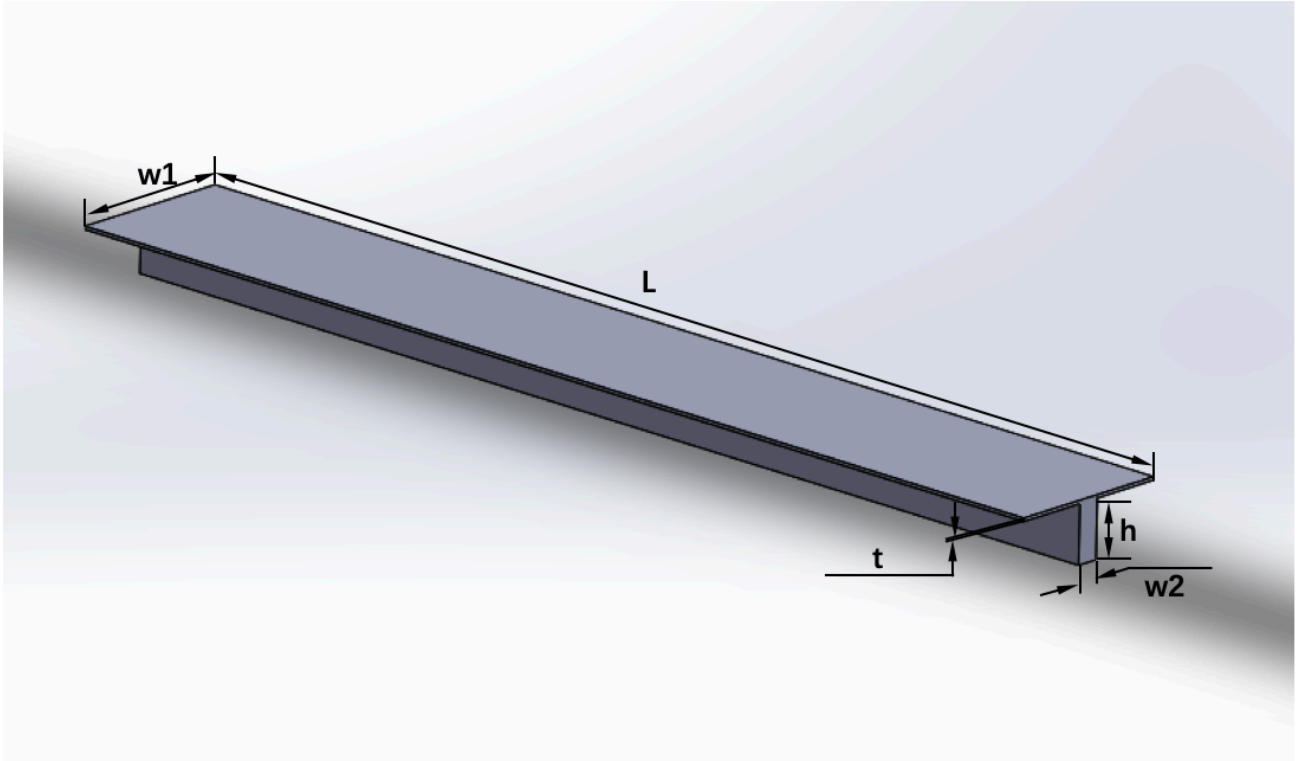

Figure 3.5 Geometric model of cantilever design D with dimension annotations.

A vertical beam was attached at the middle bottom of a regular rectangular cantilever with the same length in the cantilever design D shown in Figure 3.5. The application of the vertical beam increased the normal spring constant significantly so that the cantilever would be much more flexible in the torsional direction than in the normal direction. The disturbance in the normal direction caused by the interaction between tip and sample surface would be minimized. The effects of the geometric parameters on the torsional spring constant of cantilever design D were investigated and Table 3.4 demonstrates the ranges of the geometric parameters tested.

Table 3.5 The properties of cantilever materials to be studied

Properties	Elastic Modulus (N/m^2)	Poisson's Ratio	Mass Density (kg/m^3)	Yield strength (N/m^2)
Si_3N_4	3.10e11	0.27	3290	3.56e5
BN	3.41e10	0.21	2190	3.97e7
Ni-Ti (Martensitic)	2.80e10	0.41	6410	7.00e7
Graphite	8.7e9	0.16	1500	2.55e7

3.3.2 Tip geometry design

After the cantilever design with the lowest torsional spring constant was identified, the tip was attached, and contact modelling was conducted to investigate the performance of different tip shapes introduced in the Section 3.4.4. Tips with two geometries (shown in Figure 3.6) were proposed to improve the measurement sensitivity of mLFM.

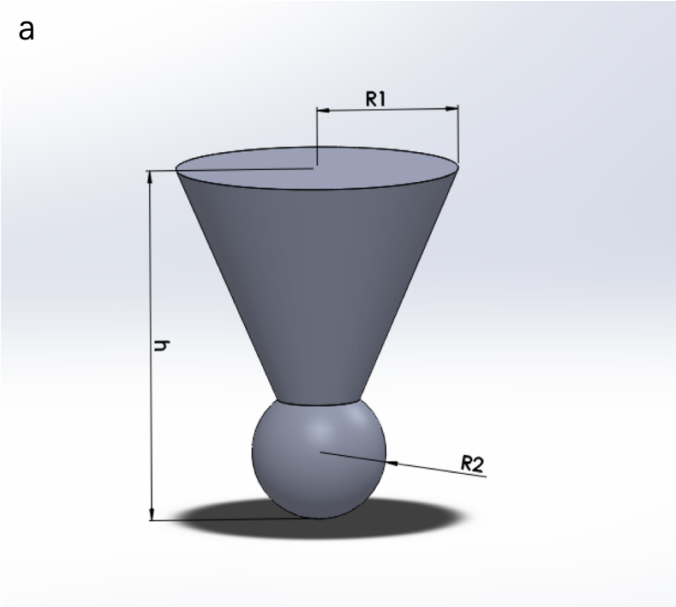

Figure 3.6 Geometric models of tip designs with different configurations that are to be investigated: (a) tip design A; (b) tip design B.

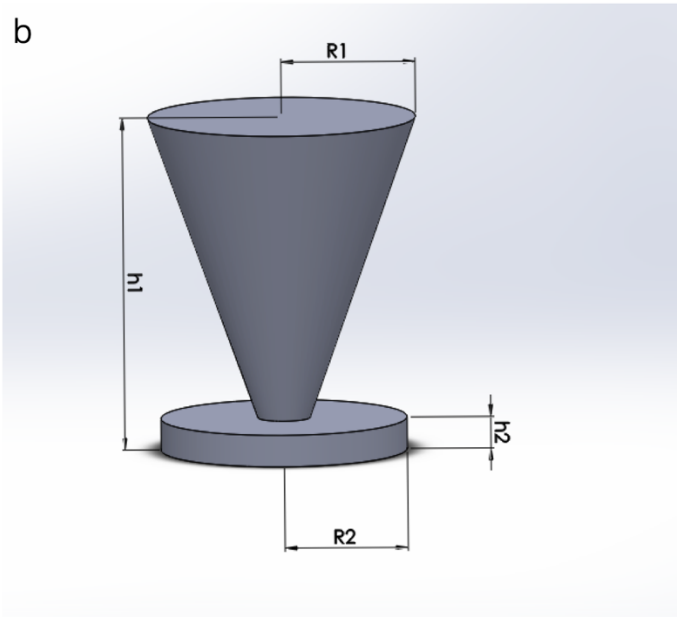

Figure 3.6 Geometric models of tip designs with different configurations that are to be investigated: (a) tip design A; (b) tip design B. (continued)

For tip design A and B, a sphere and a round disk was attached to the apex of a cylindrical tip respectively. The sphere or the disk touched the sidewall of the sample first when the tip was approaching the sidewall of the sample in modified LFM. Compared to the normal tetrahedral tip, these two tip geometries allowed the contact between the tip and the sample for a longer period of time, which should cause larger twist when the scanning path and distance was determined. The spherical shape of design A provided more uniform contact area reduces localized pressure between the tip and the sample surface. In LFM, the tip height could be approximately considered as the lever arm distance of the torque in the torsion calculation. However, the lever arm distance was no longer the tip height in mLFM but the perpendicular distance from point of force action to the rotation axis. When the total heights of the two tip geometries were the same, the round disk design in the geometry design B produced longer lever arm distance which should lead to larger torque and larger twist of the cantilever than design A.

All the parts creation procedures in SolidWorks, including the cantilever designs and tip designs, were listed in the Appendix A.

Table 3.6 The geometric parameters of the tip design A and testing ranges

Parameters	R1 (μm)	R2 (nm)	h (μm)	Tip position (μm)
Ranges or constraints	1.5	150-600	2.5	4-28

Table 3.7 The geometric parameters of the tip design A and testing ranges

Parameters	R1 (μm)	R1 (nm)	h1 (μm)	h2 (nm)	Tip position (μm)
Ranges or constraints	1.5	150-600	2.5	150	4-28

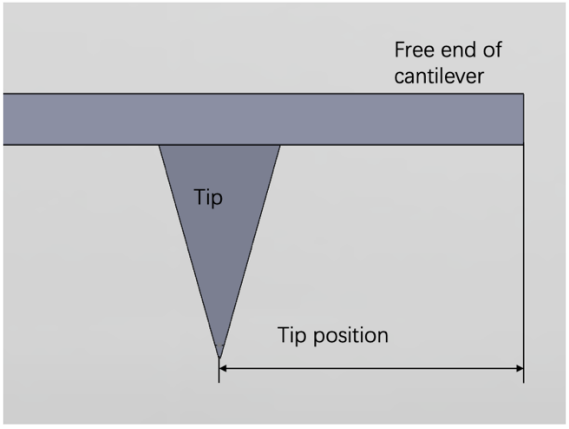

Figure 3.7 The tip position defined as the distance between the tip and the free end of the cantilever

The effect of variations in the sphere radius and the disk radius on the measurement sensitivity was explored by performing the simulation in interval of 50nm from 150nm to 600nm of the radius. The tip position was defined as the distance from the edge of the cantilever free end to the center of the circular cross-section between the tip and the cantilever as illustrated in Figure 3.7. The effect of tip position was also investigated by calculating the measurement sensitivity of varied tip position value with the interval of 4μm when the other test conditions

were constant. Different geometric parameters were investigated and simulated, the ranges of which are listed in Table 3.6 and Table 3.7. The corresponding parameters are shown in the Figure 3.6. Because special mechanical properties were not required for the tip, the same material properties as the corresponding cantilever were assigned to the tip shown in Table 3.5.

3.3.3 Sample selection

A hard sample and a soft sample with the mechanical properties of silicon dioxide and Sylgard-184 silicon elastomer respectively were chosen as control samples in the FEA. The silicon dioxide is the material of the Bruker calibration grid which was generic hard control sample used for the calibration in AFM and LFM. The soft sample Sylgard-184 Silicon Elastomer was chosen because it was widely used in the nonlinear deformation investigation of biomedical materials and biological membranes in mechanobiology (Hopf, Bernardi, Menze, Zündel, Mazza & Ehret, 2016). Because complex geometries were not necessary in the study of linear and nonlinear deformation of the sample, the sample was simplified as a cubic block with the length of 800nm in the simulation. The structure is shown in Figure 3.8 and the mechanical properties are shown in Table 3.8.

Table 3.8 The material properties of the samples used in the contact model

Properties	Elastic Modulus (N/m^2)	Poisson's Ratio	Mass Density (kg/m^3)	Yield strength (N/m^2)
Silicon dioxide	6.63e10	0.150	2170	4.50e7
Sylgrid-184	2.97e6	0.499	1030	1.20e6

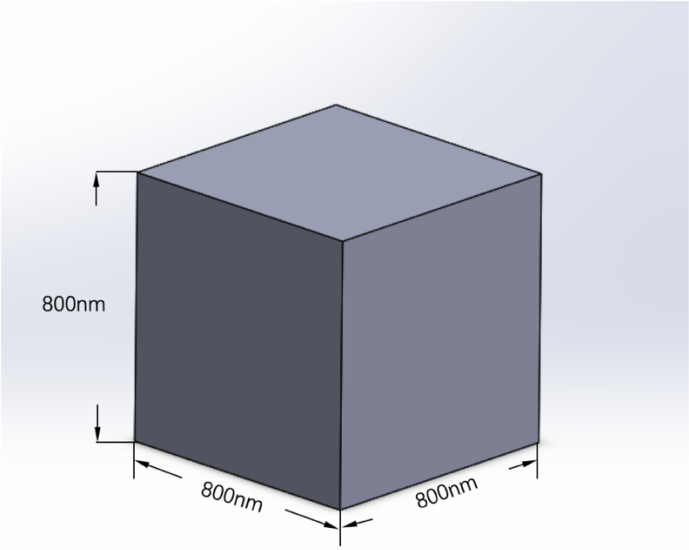

Figure 3.8 Configurations of samples to be used in the simulation.

3.4 Test procedures

3.4.1 Normal spring constant

The normal spring constant of the four cantilever designs were measured by FEA to explore their normal stiffness and to identify the normal stiffness-torsional stiffness ratio. Figure 3.9 shows the FEA setups for the normal spring constant measurement taken the example of DNP cantilever. The normal spring constant of the control DNP cantilever was measured and compared with the analytical calculation Eq. (2-3) for the model validation. A force of 5×10^{-15} N in the normal direction was applied at the free end of the cantilever. The value of the force was determined by trials and error to make sure the deflection of the cantilever remaining in the small displacement region and yet detectable. The other end of the cantilever was fixed completely as it would be fixed on the substrate in the real working environment of mLFM. The normal spring constant (N/m) of the cantilever was calculated by Eq. (2-1) where the F was 5×10^{-15} N and d was the normal displacement at the free end of the cantilever acquired from the simulation

results. The influence of gravity on the cantilever normal spring constant was not taken into consideration in the derivation of Eq. (2-3), so it was also neglected in the simulation setup for better comparison.

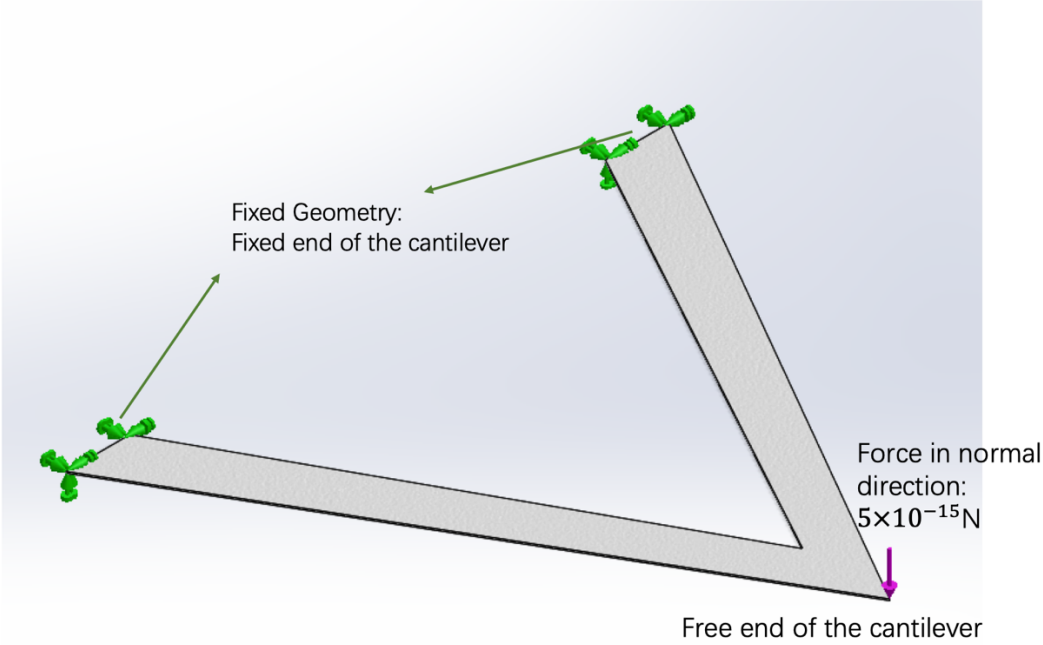

Figure 3.9 The illustration of torsional spring constant measurement model of DNP cantilever

3.4.2 Torsional spring constant

The torsional spring constants of the cantilevers were measured to identify the optimum cantilever design with the corresponding geometric parameters and material properties. Figure 3.10 shows the FEA setup of the torsional spring constant measurement of the DNP control probe. A prescribed torque of 5×10^{-15} Nm about the Axis 1 was applied at the free end of cantilever and the perpendicular distance from the action position to the cantilever free end was 4μm. The magnitude of the torque was also determined by trials and error, which caused detectable torsion of the cantilever in the linear deformation region. The torque can only be

applied on faces instead of edges or vertexes. Thus, an area with the width of 1 μm was splitted from the whole cantilever face to place the torque as shown in the Figure 3-11. The other end of the cantilever was defined as the fixed geometry and had zero degree of freedom as the cantilever would act in the real working condition. The gravity was not applied in the measurement of torsional spring constant, but the influence of gravity was explored specially in the next section.

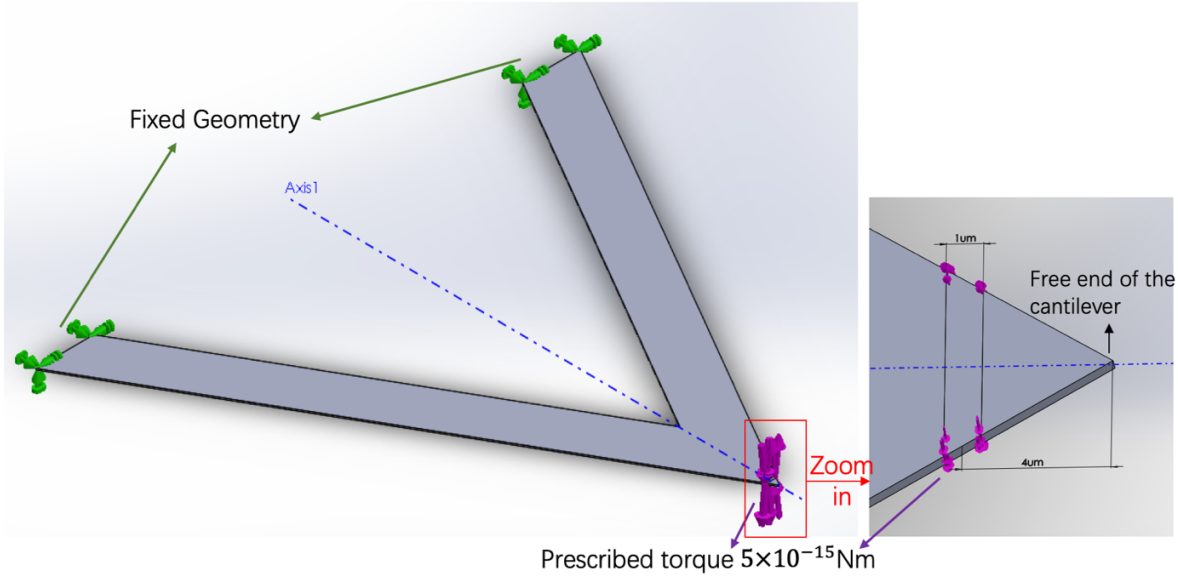

Figure 3.10 The illustration of torsional spring constant measurement model of DNP cantilever

The torsional spring constant of cantilevers was calculated by the following equations. The resultant tangential displacement was obtained to calculate the twist angle based on small angle assumption. The twist angle θ (rad) is determined as:

$$\theta = tan\theta = \frac{d_t}{d_1} \tag{3-1}$$

where d_t is the tangential displacement obtained from the simulation results and d_1 is half length of the diagonal on the cross section of the cantilever as shown in Figure 3.11. According to Eq. (2-4), the torsional spring constant (Nm/rad) in this thesis was calculated as:

$$K_\theta = \frac{T}{\theta} = \frac{5\times10^{-15}\times d_1}{d_t} \tag{3-2}$$

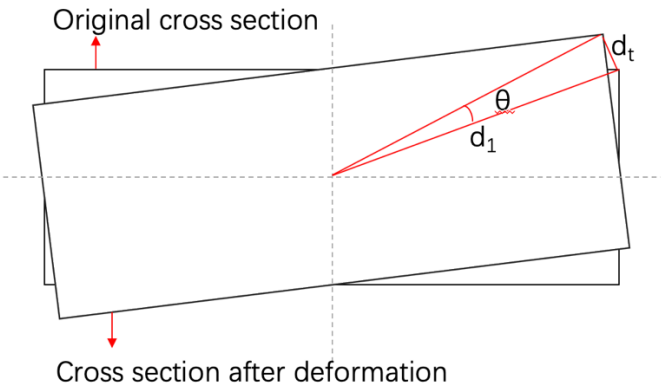

Figure 3.11 The illustration of variables used in the calculation of twist angle.

3.4.3 Normal deflection measurement

If the cantilevers are very flexible in the torsional direction, chances are that they are too fragile and have very large deflection caused by self-weight in the normal direction. Thus, the maximum deflection of the cantilevers under gravity was also measured for the optimum cantilever design identified from the Section 3.4.2 to ensure the cantilever was rigid enough in the normal direction. The simulation setting was shown in Figure 3.12. One end of the cantilever was fixed completely, and the gravity with the gravitational acceleration of 9.81 m/s^2 was applied as the external load.

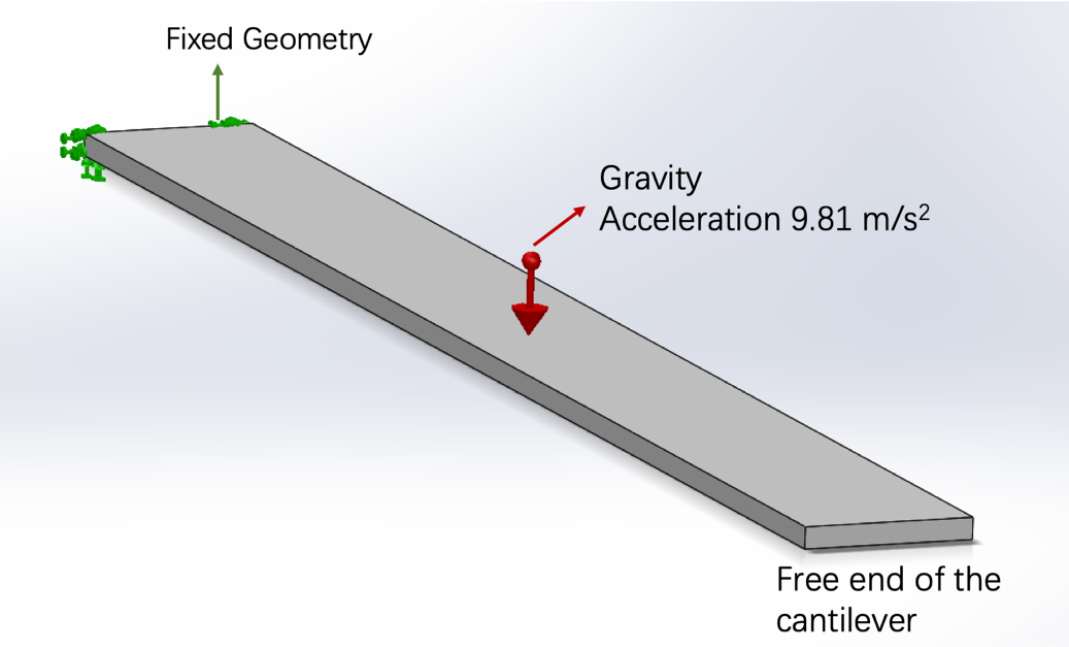

Figure 3.12 The simulation setup for measuring the normal deflection of a beam cantilever under gravity

The maximum deflection in normal direction was measured by FEM and compared to analytical equations below for model validation (Mott, 2007).

$$\delta_{max} = \frac{q \cdot L^4}{8EI} \tag{4-1}$$

$$I = \frac{b \cdot h^3}{12} \tag{4-2}$$

where the q is the distributed load intensity, which is equal to the gravity of the cantilever subtracted by the length of the cantilever; the L is the unsupported length of the cantilever, E is the Young's modulus of the cantilever material, and the I is the planar moment of inertia calculated by eq. (4-2). b is the width of the cantilever and h is the thickness of the cantilever. All the detailed procedures of the static study set-up in SolidWorks including normal spring constant measurement, torsional spring constant, and the maximum normal deflection, were provided in Appendix B.

3.4.4 Measurement sensitivity

In this procedure, the contact between the tips and the sidewall of samples was simulated by non-linear FE simulation. The tip and sample were put into touch by creating an assembly as presented in Figure 3.14. As presented in the figure, the height of the tip in the contact area with the sample sidewall was 150nm. Instead of applying an external force or torque, lateral displacement of 100nm was prescribed on the sample to simulate the scanning path of sample scanner and investigate the interaction between the tip and the sidewall of the sample. The sample was defined as a slider/roller in constraints with one degree of freedom and can only move in its plane along the direction of the prescribed displacement. No penetration contact was determined for connection between the sidewall of the sample and the tip because this type of contact allows two or more faces to touch and develop pressure or forces. The entities deformed under the pressure or forces without flowing into each other, which matched the phenomena occurring in practice. The detailed nonlinear study set-up procedures in SolidWorks were provided in Appendix C.

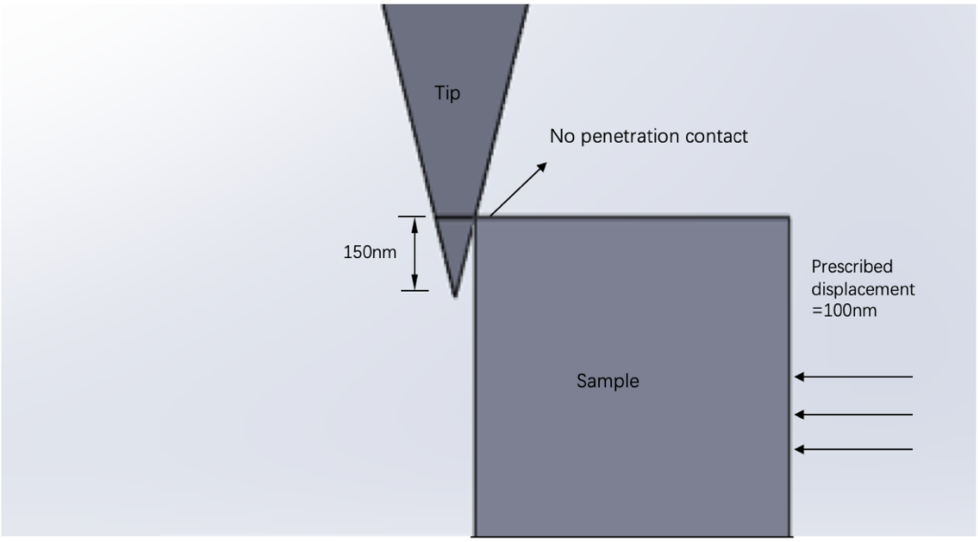

Figure 3.13 The contact assembly of the control DNP tip and the sample.

The contact situation of the tip design A and the tip design B were shown in Figure 3-15. The edge of the sample side wall had an initial contact with the orthodrome of the sphere no matter the change of the sphere radius. In terms of tip design B, the height of the disk remained at 150nm for the contact with the sample sidewall.

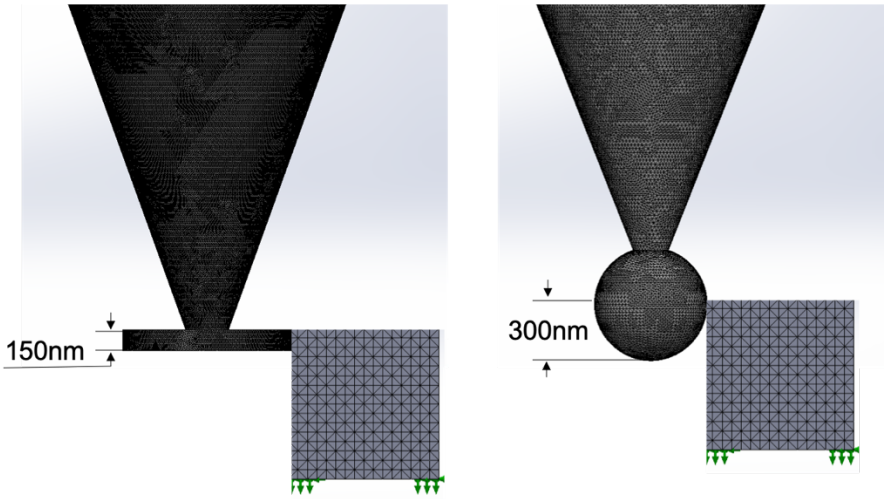

Figure 3.14 The contact assembly of the tip design A and B with the sample respectively.

The twist angle of the cantilever (θ) will be obtained from Eq. (3-3) and the resultant force *F* on the tip was probed by selecting "List Result Force" after running the simulation. The measurement sensitivity *S* was calculated as:

$$S = \frac{\theta}{F} = \frac{d_t}{F \times d_1} \tag{3-3}$$

3.5 Threats

The potential treats occurred in the cantilever-tip design study was considered. Even if the set-up of FE simulation is appropriate, the accuracy of FEA could be subject to the three types of errors: modelling error, discretization error, and numerical error (Shah, 2002; Murad,

2019). The modeling errors might occur due to the assumptions and simplifications made in the Chapter 1. The discretization errors arise from the creation of the meshing and the density of meshing (Shah, 2002). In this study, the creation of the meshing might be influenced by the variation of geometric parameters even if the simulation set-up and the meshing control stays consistent. The numerical errors arise because of the approximation and the rounding of the software when dealing with extremely large or small numbers (Murad, 2019).

3.6 Summary

This chapter covered the key variables, design criteria and testing procedures to investigate the optimum probe configuration parameters in order to improve the sensitivity of the mLFM technique by utilizing finite element modelling and analysis. The experimental design, modelling software and data regression methods were also outlined.

CHAPTER 4. RESULTS

4.1 Model Validation Results

The simulation data of the control probe, the DNP silicon nitride probe, was compared with the analytical calculations and experimental results for the validation of FEA settings. The normal and torsional spring constant were calculated and compared to applicable analytical solution Eq. (2-3) and (2-6) respectively to validate the static study model. The normal spring constants of the DNP probe were 0.0967N/m from the theoretical calculation and 0.0935 N/m from simulation with the error of 3.31%. The normal displacement of cantilever increased gradually from the fixed end to the free end and reached the maximum value at the free end as shown in the Figure 4.1. The maximum deflection of -5.347×10^{-8} μm was used to calculate the normal spring constant by Eq (2-1).

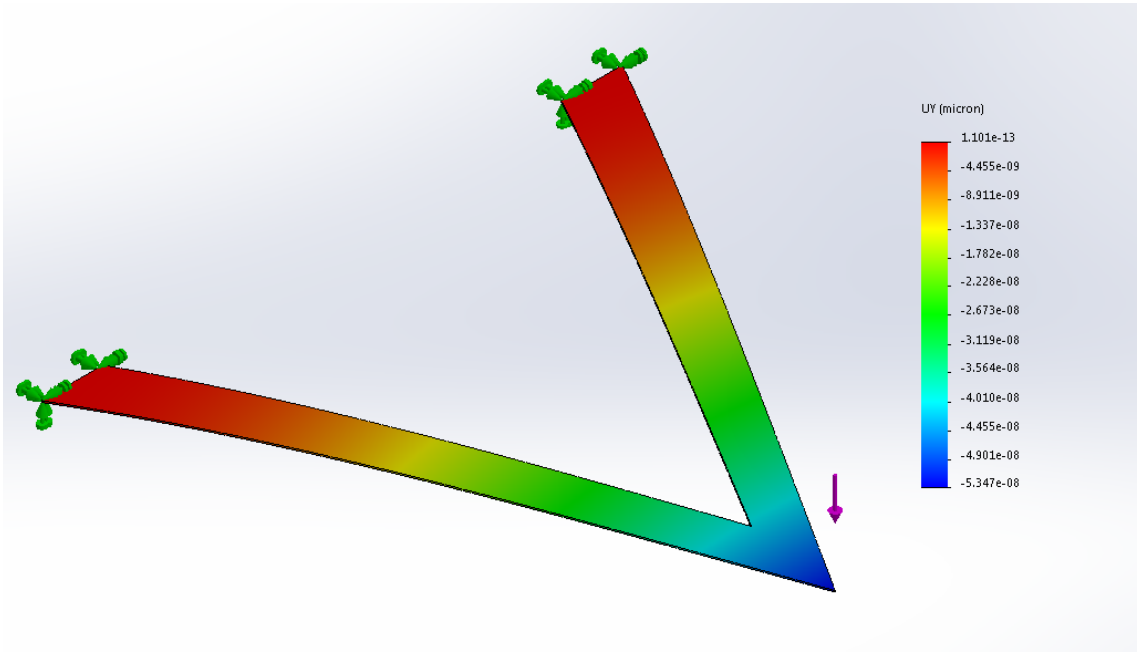

Figure 4.1 The normal displacement of the DNP cantilever in the normal spring constant measurement

The torsional spring constant obtained from the analytical solution Eq. (3-5) was 2.21 × 10^{-9} Nm/rad and the one from simulation was 2.35 × 10^{-9} Nm/rad whereby the error was 6.51%. Figure 4.2 shows the tangential displacement result of the DNP cantilever simulation in torsional direction. The region with the red color shows the maximum deformation on the whole body located in the middle of the cantilever close to the free end. The tangential displacement on the edge of cantilever 4 µm to the free end was probed and used to calculate the torsional spring constant. The tangential displacements of all the cantilevers were taken at the same place to calculate the torsional spring constants for consistency.

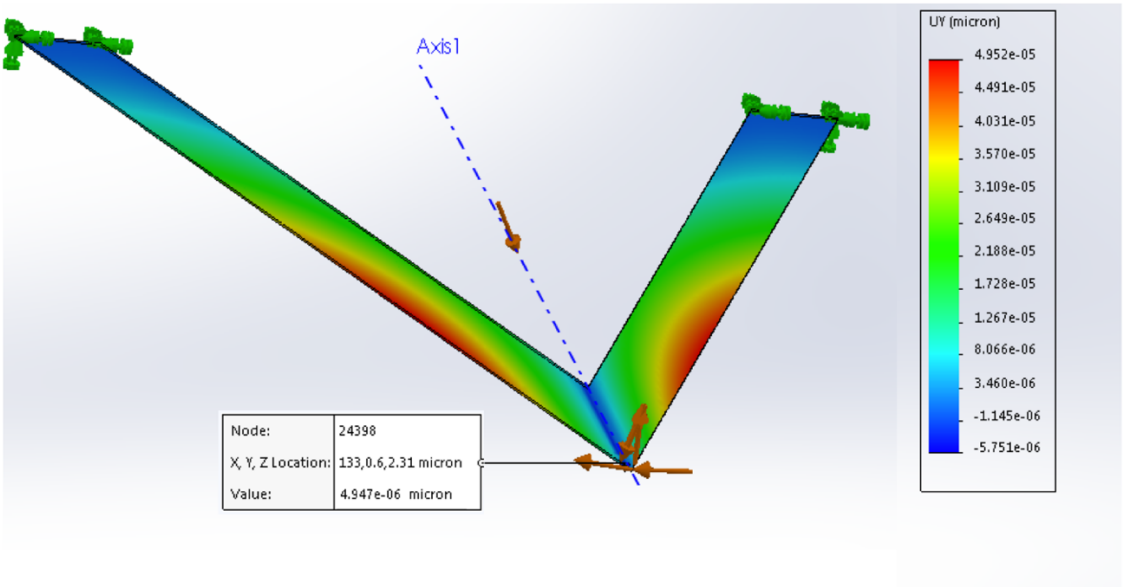

Figure 4.2 The tangential displacement of DNP cantilever in torsional spring constant.

The normal displacement of the beam cantilever caused by gravity was illustrated by Figure 4.3. The normal deflection increased gradually from the fixed end to the free end and reached the maximum value at the free end. The maximum deflection value at the free end was 4.389 × 10^{-9} m. The gravity acceleration of 9.81m/s^2 was used in the calculation. *L*, *b*, and *h*

were 500µm, 50µm, and, 6µm respectively. The maximum deflection calculated from Eq. (4-1) was 4.40× 10^{-9} m and the error between the calculation and the simulation results was 0.25%.

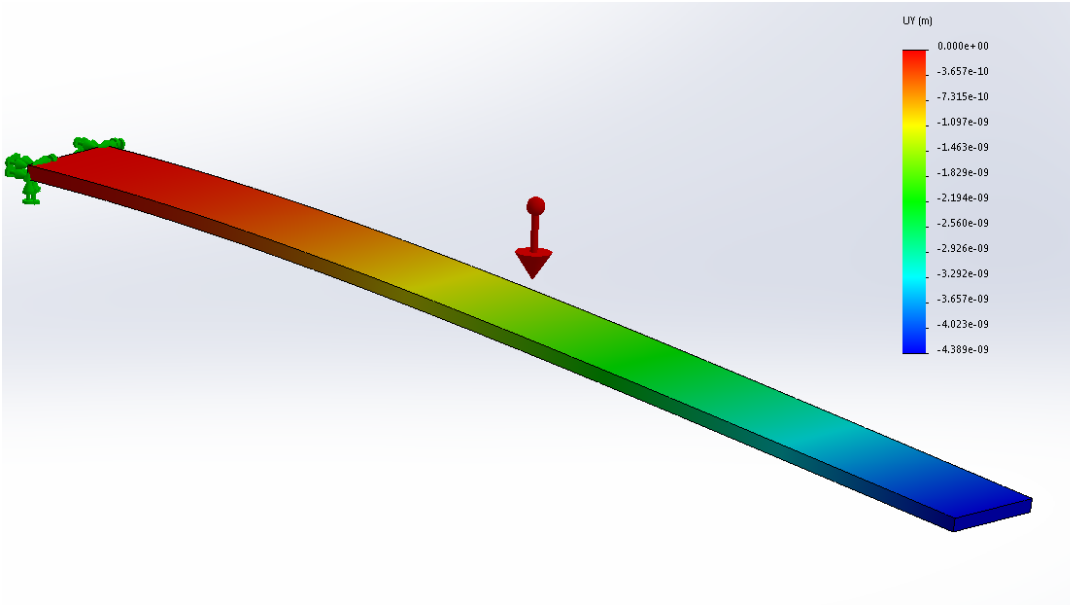

Figure 4.3 The normal displacement of the beam cantilever under gravity

The validation of the contact model between the tip and the sample surface was accomplished by simulation of the DNP V-shape cantilever and the silicon dioxide calibration grid. The deflection of the cantilever in lateral direction obtained from the contact modeling was compared to the experimental results obtained in Hseu's thesis (Hseu, 2015). When the hard sample contacted the tip and continued to move in the lateral direction of 100 nm, the lateral deflection from simulation and experiments were 46.48nm and 48.29nm respectively leading to the error of 3.54%.

The force-time curves at all directions were provided the SolidWorks and the data points were extracted to plot the processed contact force-distance curves. The force-distance curve on the hard sample shows linearity and the force reaches the peak of 22.84nN when the sample

moved for 100nm in the lateral direction as illustrated in Figure 4.4. The force-distance curve of the soft sample was also processed by the data points abstracted from the force-time curves shown in Figure 4.5. The black line represented the actual force curves and the red dot line acted as a linear reference. According to the figure, the force-distance curve on the soft sample also shows both linearity and nonlinearity. The force reached the peak of 23.6nN when the sample moved for 500nm in the lateral direction and the red dotted line acted as a linear reference. The force-distance curve of the soft sample was observed to enter the nonlinear region when the tip moved for 300nm in the lateral direction. The soft sample did not resist the contact from the tip as much as the hard sample, so the maximum force of soft sample was lower than the hard sample when the moving distances of the tip were the same.

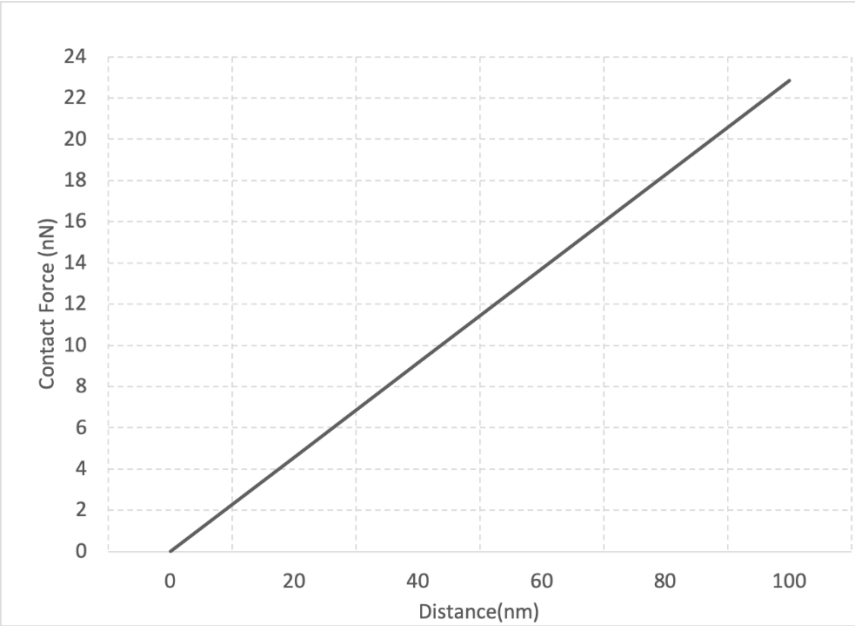

Figure 4.4 The processed force-distance curve of the DNP probe contacting the hard sample with prescribed displacement of 100nm.

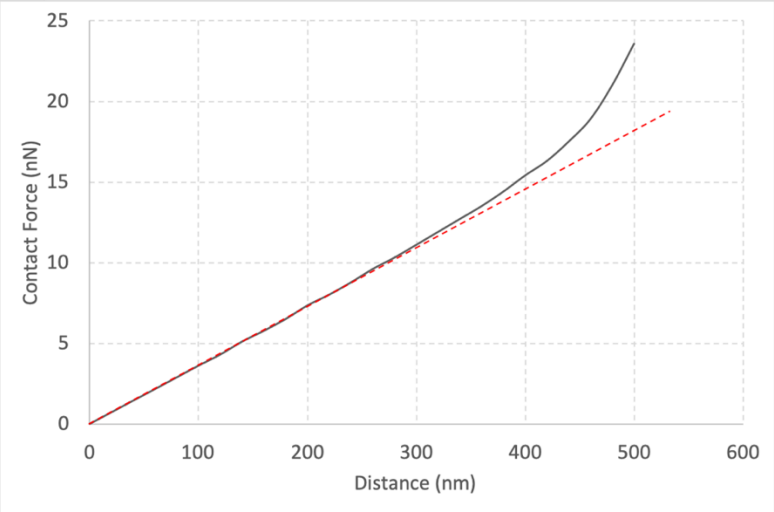

Figure 4.5 The processed force-distance curve of the DNP probe contacting the soft sample with prescribed displacement of 500nm.

The tangential displacement result in the Figure 4.6 shows the torsional deformation of the cantilever. The deformation in torsional direction concentrated on half of the cantilever close to the free end and the deformation reached maximum at the free end. The other half of the cantilever towards the fixed end barely deformed. The blue region and the red region on two sides of the major axis demonstrates the different directions of the tangential displacement, which is in compliance with the torsional phenomenon.

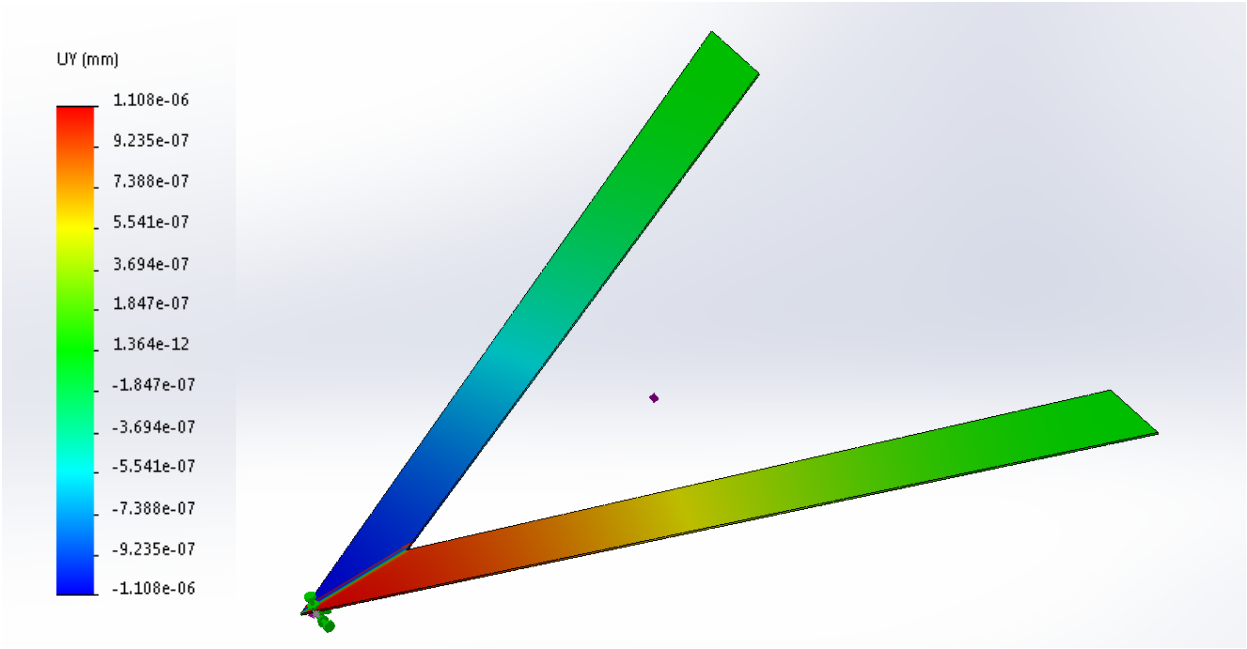

Figure 4.6 The tangential displacement of contact simulation between a DNP probe and the silicon dioxide sample

4.2 Cantilever Design Data

4.2.1 Torsional spring constant of design A

The torsional spring constants of cantilever Design A made from three materials, i.e. boron nitride (BN), nickel-titanium alloy (Ni-Ti), and graphite were investigated. The effects of the geometric parameters on the torsional spring constant within the test ranges shown in Table 3-1 were also studied. Figure 4.7 shows the relationship between the torsional spring constant and the cantilever length (L1 in Figure 3.2) of design A expressed by a power function. The parameters and the corresponding values used in the test are listed in Table 4-1. The trendlines of the torsional spring constant with the variation of length accomplished by curve fit with R-squared values are also shown in the figure. The R-squared defines how much variation in torsional spring constant can be explained by the variation in length. The trend is most reliable

when the R-squared is at or near 1. Thus, the appropriate curve fit method was chosen for each plot to get a R-squared value closest to 1 through data analysis.

Table 4.1 Parameters and values used in the investigation of length on torsional spring constant

Parameter	L1 (μm)	L2 (μm)	w1 (μm)	w2 (μm)	t (μm)	d (μm)
Values	200, 250, 300, 350, 400, 450	0.2×L1	30	24	0.6	0.3

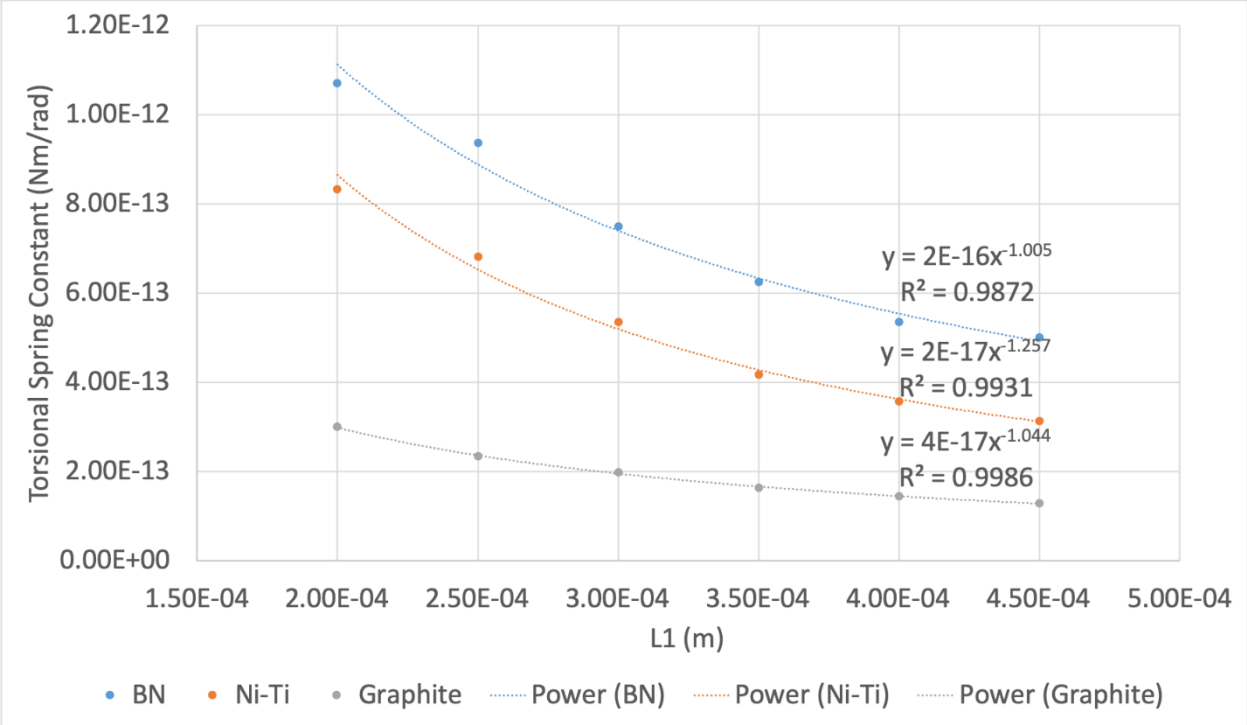

Figure 4.7 Cantilever design A: the effect of length on torsional spring constant made from three materials

The torsional spring constant of cantilever design A made from the boron nitride ranged from the 1.02×10^{-12} Nm/rad to 5.00×10^{-13} Nm/rad when length changed from 200μm to 450μm. The torsional spring constant made from Ni-Ti alloy ranged from 8.33×10^{-13} Nm/rad to 3.13×10^{-13} Nm/rad when length changed from 200μm to 450μm. The torsional spring constant made from graphite ranged from 3.00×10^{-13} Nm/rad to 1.29×10^{-13} Nm/rad when length

increased from 200μm to 450μm. The torsional spring constant of cantilever design A reduced as the length increased for the three materials as shown in the Figure 4.7.

The relationship between the torsional spring constant and the cantilever width (w1 in Figure 3.2) of design A was expressed by a linear function. The parameters and the corresponding values used in the test are listed in Table 4-2. The torsional spring constant of cantilever design A made from the boron nitride ranged from the 6.51×10^{-13} Nm/rad to 7.69×10^{-13} Nm/rad when width changed from 15μm to 40μm. The torsional spring constant made from Ni-Ti alloy ranged from 5.15×10^{-13} Nm/rad to 5.68×10^{-13} Nm/rad when width changed from 15μm to 40μm. The torsional spring constant made from graphite ranged from 1.88×10^{-13} Nm/rad to 2.00×10^{-13} Nm/rad when width went up from 15μm to 40μm. The trendlines of the torsional spring constant with the variation of width in Figure 4.7 illustrated that the torsional spring constant of cantilever design A went up with the increase of the width.

Table 4.2 Parameters and values used in the investigation of width on torsional spring constant

Parameter	L1 (μm)	L2 (μm)	w1 (μm)	w2 (μm)	t (μm)	d (μm)
Values	300	60	15, 20, 25, 30, 35, 40	0.2× w1	0.6	0.3

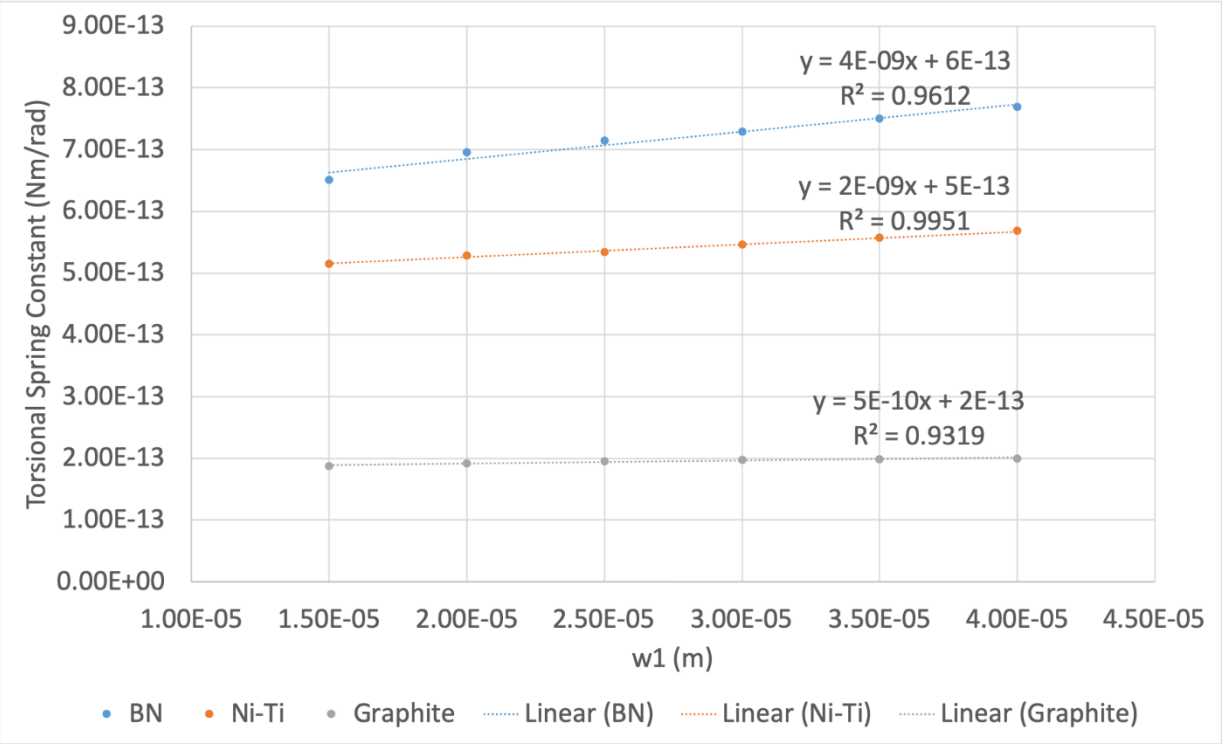

Figure 4.8 Cantilever design A: the effect of width on torsional spring constant made from three materials

The relationship between the torsional spring constant and the cantilever thickness (t in Figure 3-2) of design A expressed by a power function. The parameters and the corresponding values used in the test are listed in Table 4-3. The torsional spring constant of cantilever design A made from the boron nitride increased from the 7.5×10^{-13} Nm/rad to 2.5×10^{-12} Nm/rad when thickness varied from 0.6 µm to 0.8 µm. The torsional spring constant made from Ni-Ti alloy increased from 5.36×10^{-13} Nm/rad to 1.50×10^{-12} Nm/rad when thickness increased from 0.6 µm to 0.8 µm. The torsional spring constant made from graphite ranged from 1.97×10^{-13} Nm/rad to 5.77×10^{-13} Nm/rad when thickness changed from 0.6µm to 0.8µm. The trendlines of the torsional spring constant with the variation of width in Figure 4.9 illustrated that the torsional spring constant of cantilever design A increased with the increment of

thickness. According to the three figures in this section, the cantilever made from boron nitride provided highest spring constant, and the Ni-Ti alloy ranked the second. The graphite was the most promising material to fabricate the cantilevers with lowest torsional spring constant among the three.

Table 4.3 Parameters and values used in the investigation of thickness on torsional spring constant

Parameter	L1(μm)	L2(μm)	w1 (μm)	w2 (μm)	t (μm)	d (μm)
Values	300	60	30	24	0.6, 0.64, 0.68, 0.72, 0.76, 0.8	0.8× t

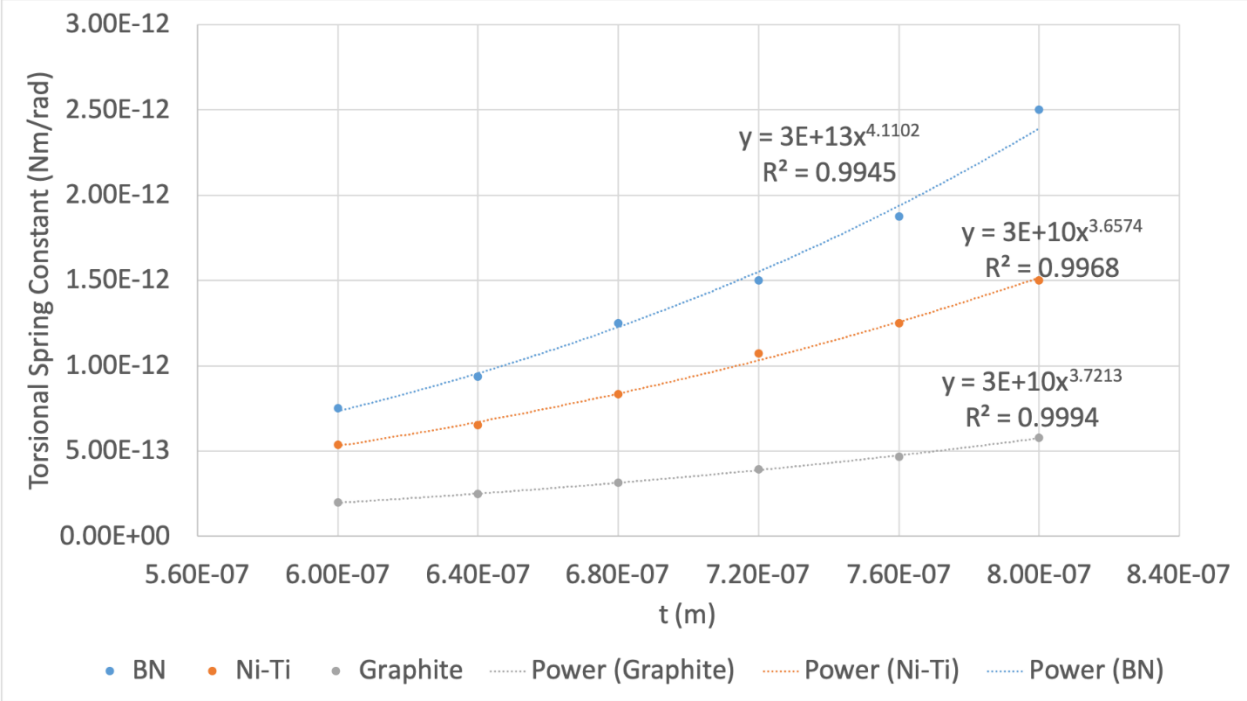

Figure 4.9 Cantilever design A: the effect of thickness on torsional spring constant made from three materials

4.2.2 Torsional spring constant of design B

The torsional spring constants of cantilever Design B made from three materials, i.e. boron nitride (BN), nickel-titanium alloy (Ni-Ti), and graphite were measured. The effects of the

geometric parameters on the torsional spring constant within the test ranges shown in Table 3.2 were also studied. Figure 4.10 shows the relationship between the torsional spring constant and the cantilever length (L1 in Figure 3-3) of design B in a power function. The parameters and the corresponding values used in the test are listed in Table 4.4.

Table 4.4 Parameters and values used in the investigation of length on torsional spring constant

Parameter	L1 (μm)	L2 (μm)	L3 (μm)	w1 (μm)	w2 (μm)	α (°)	t (μm)
Range	200, 250, 300, 350, 400, 450	0.4×L1	0.8×L1	30	15	30	0.6

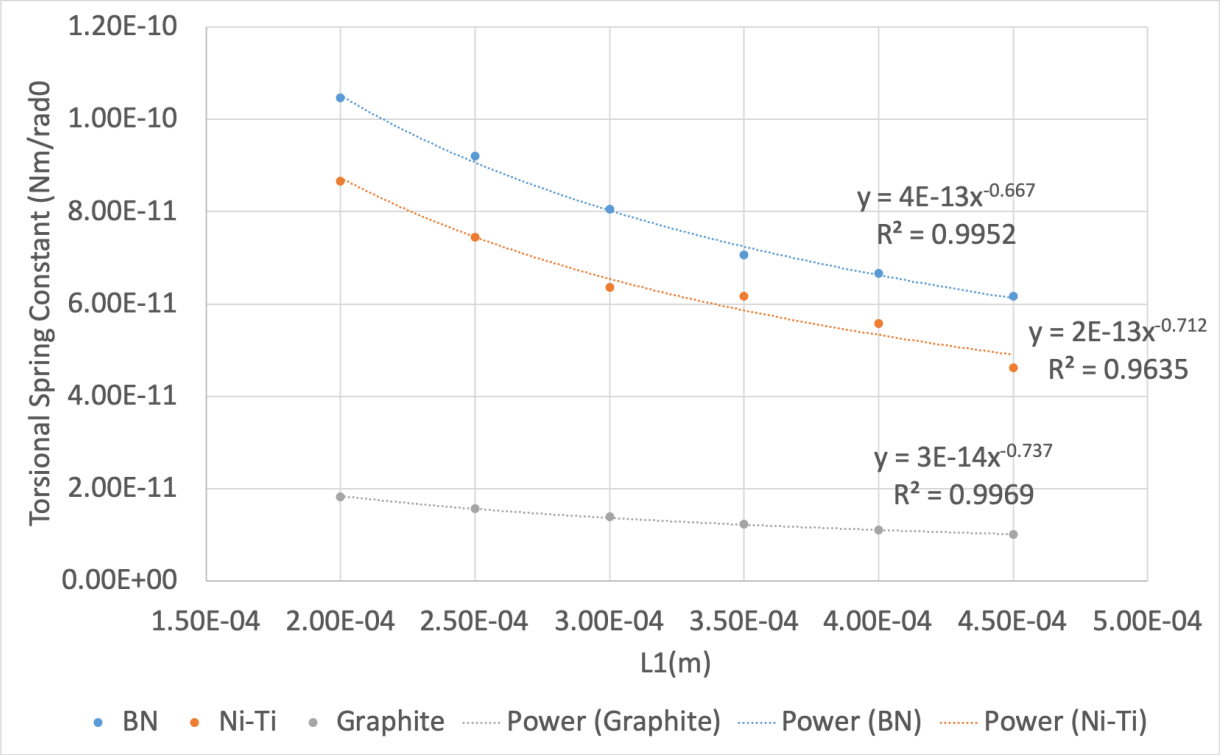

Figure 4.10 Cantilever design B: the effect of length on torsional spring constant made from three materials

The torsional spring constant of cantilever design B made from the boron nitride decreased from the 1.05×10^{-10} Nm/rad to 6.17×10^{-11} Nm/rad when length varied from 200μm to 450μm. The torsional spring constant made from Ni-Ti alloy decreased from 8.67×10^{-11}

Nm/rad to 4.62 × 10^{-11} Nm/rad when length increased from 200μm to 450μm. The torsional spring constant made from graphite decreased from 1.82 × 10^{-11} Nm/rad to 1.03 × 10^{-11} Nm/rad when length increased from 200μm to 450μm. The torsional spring constant of cantilever design A reduced as the length increased for the three materials as shown in the Figure 4.10.

The torsional spring constant of cantilever B was expressed as a function of cantilever width (w1 in Figure 3.3) demonstrated in the Figure 4.11. The parameters and the corresponding values used in the test are listed in Table 4.5. The torsional spring constant of cantilever design B made from the boron nitride increased from the 7.06 × 10^{-11} Nm/rad to 8.73 × 10^{-11} Nm/rad when width went up from 15μm to 40μm. The torsional spring constant made from Ni-Ti alloy increased from 5.69 × 10^{-11} Nm/rad to 6.84 × 10^{-11} Nm/rad when width changed from 15μm to 40μm. The torsional spring constant made from graphite ranged from 1.01 × 10^{-11} Nm/rad to 1.73 × 10^{-11} Nm/rad when width increased from 15μm to 40μm. The trendlines of the torsional spring constant with the variation of width in Figure 4.11 illustrated that the torsional spring constant of cantilever design B went up with the increase of the width for the three materials.

Table 4.5 Parameters and values used in the investigation of width on torsional spring constant

Parameter	L1 (μm)	L2 (μm)	L3 (μm)	w1 (μm)	w2 (μm)	$\boldsymbol{\alpha}$ (°)	t (μm)
Range	300	120	240	15, 20, 25, 30, 35, 40	0.5× w1	30	0.6

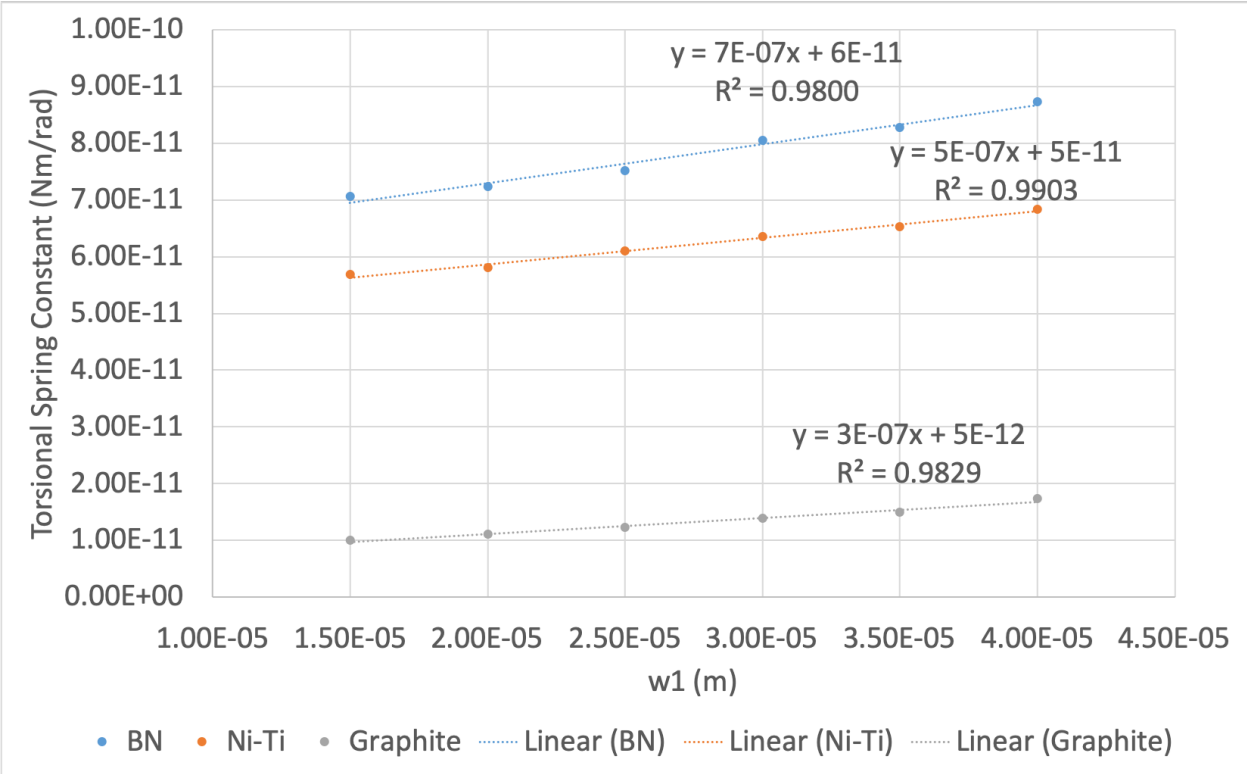

Figure 4.11 Cantilever design B: the effect of width on torsional spring constant made from three materials

The torsional spring constant of cantilever B was expressed as a logarithmic function of the half angle (α in Figure 3.3) demonstrated in the Figure 4.12. The parameters and the corresponding values used in the test are listed in Table 4.6. The torsional spring constant of cantilever design B made from the boron nitride increased from the 3.77×10^{-11} Nm/rad to 8.05×10^{-11} Nm/rad when the angle went up from 15˚ to 30˚. The torsional spring constant made from Ni-Ti alloy increased from 2.51×10^{-11} Nm/rad to 6.36×10^{-11} Nm/rad when when the angle varied from 15˚ to 30˚. The torsional spring constant made from graphite ranged from 1.02×10^{-11} Nm/rad to 1.39×10^{-11} Nm/rad when the angle increased from 15˚ to 30˚. The trendlines of the torsional spring constant with the variation of the cantilever half angle in

Figure 4.12 illustrated that the torsional spring constant of cantilever design B went up with the increase of the half angle within the test range.

Table 4.6 Parameters and values used in the investigation of half angle on torsional spring constant

Parameter	L1 (μm)	L2 (μm)	L3 (μm)	w1 (μm)	w2 (μm)	α (°)	t (μm)
Range	300	120	240	30	15	15, 18, 21, 24, 27, 30	0.6

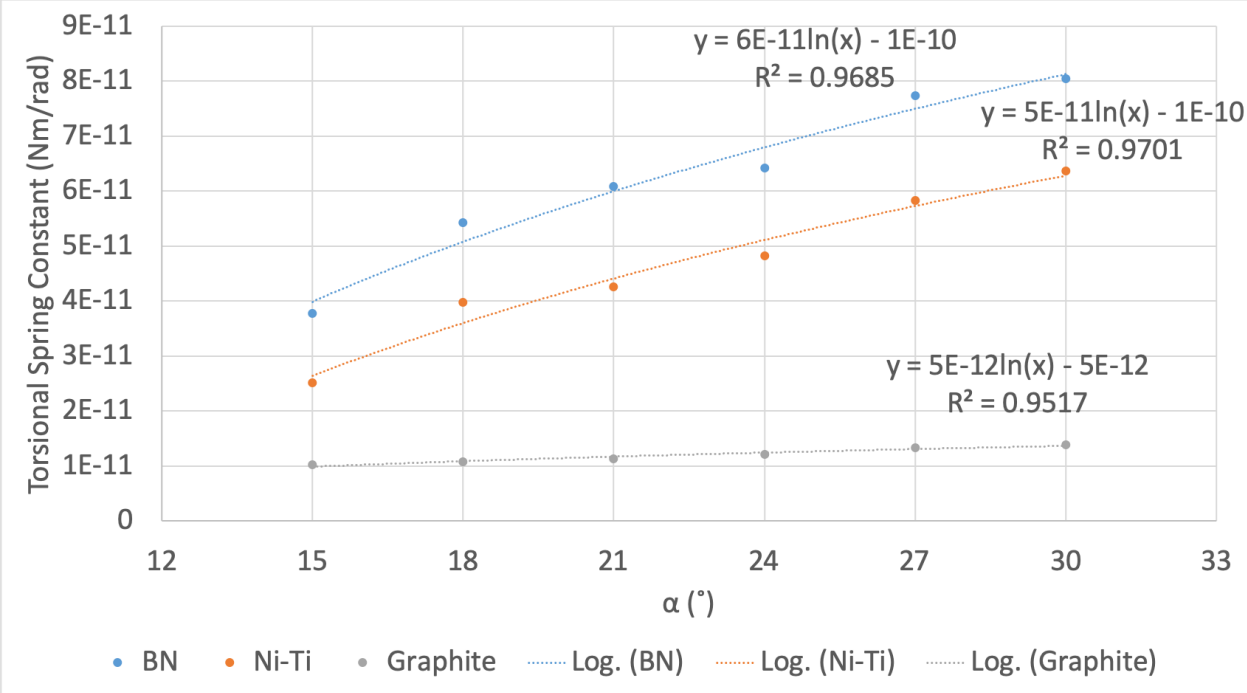

Figure 4.12 Cantilever design B: the effect of half angle on torsional spring constant made from three materials

The relationship between the torsional spring constant and the cantilever thickness (t in Figure 3.3) of design B was expressed by a power function. The parameters and the corresponding values used in the test are listed in Table 4.7. The torsional spring constant of cantilever design B made from the boron nitride increased from the 8.05×10^{-11} Nm/rad to 1.31

$\times 10^{-10}$ Nm/rad when thickness increased from 0.6 μm to 0.8 μm. The torsional spring constant made from Ni-Ti alloy increased from 6.36×10^{-11} Nm/rad to 1.15×10^{-10} Nm/rad when thickness increased from 0.6 μm to 0.8 μm. The torsional spring constant made from graphite ranged from 1.39×10^{-11} Nm/rad to 2.79×10^{-11} Nm/rad when thickness changed from 0.6μm to 0.8μm. The trendlines of the torsional spring constant with the variation of width in Figure 4.13 illustrated that the torsional spring constant of cantilever design B increased with the increment of thickness. According to the figures in this section, when the geometric dimensions were the same, the cantilevers made from graphite possessed the lowest torsional spring constants while the boron nitride turned out to be the most rigid material in the torsional direction among the three materials and Ni-Ti alloy fell in the middle.

Table 4.7 Parameters and values used in the investigation of thickness on torsional spring constant

Parameter	L1 (μm)	L2 (μm)	L3 (μm)	w1 (μm)	w2 (μm)	$\boldsymbol{\alpha}$ (°)	t (μm)
Range	300	120	240	30	15	30	0.6, 0.64, 0.68, 0.72, 0.76, 0.8

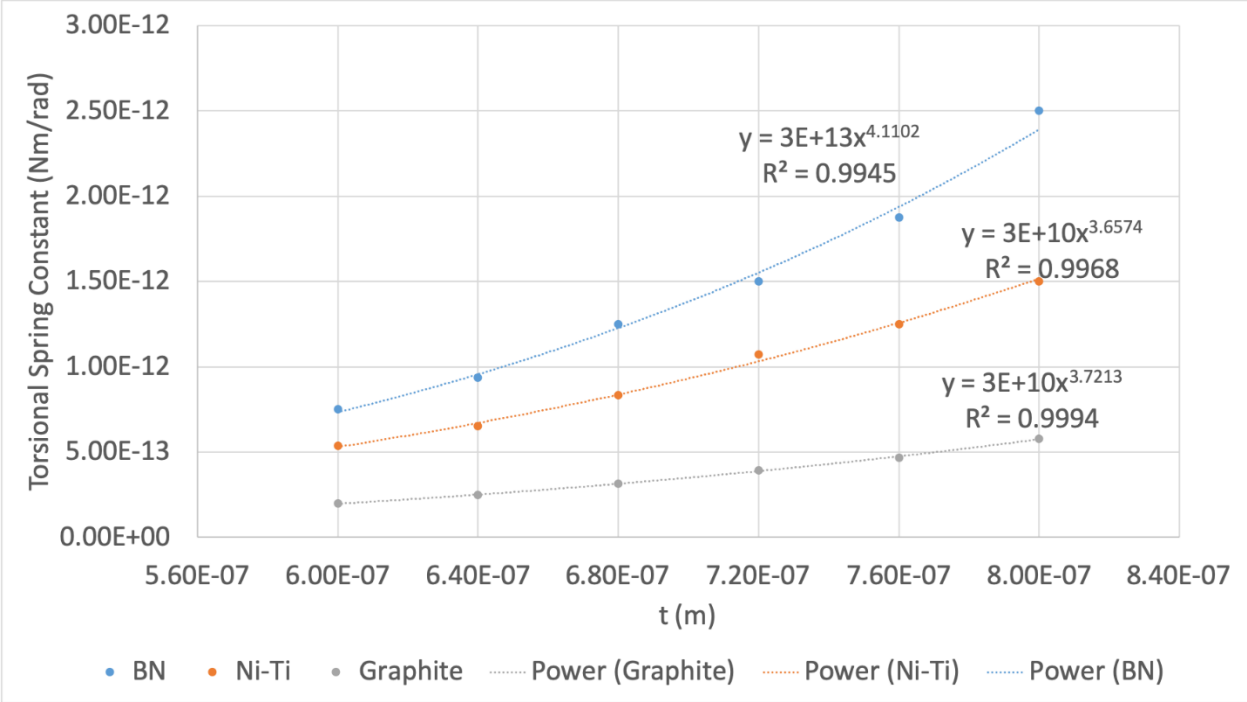

Figure 4.13 Cantilever design B: the effect of thickness on torsional spring constant made from three materials

4.2.3 Torsional spring constant of design C

The effects of the geometric parameters on the torsional spring constant within the test ranges shown in Table 3.3 for three materials were studied. Figure 4.14 shows the torsional spring constant of design C in a power function of the total cantilever length (L1 plus L2 in Figure 3-4). The parameters and the corresponding values used in the test are listed in Table 4.8. The torsional spring constant of cantilever design C made from the boron nitride decreased from the 3.63×10^{-10} Nm/rad to 1.58×10^{-10} Nm/rad when total length varied from 200μm to 450μm. The torsional spring constant made from Ni-Ti alloy decreased from 2.46×10^{-10} Nm/rad to 1.07×10^{-10} Nm/rad when length increased from 200μm to 450μm. The torsional spring constant made from graphite decreased from 7.83×10^{-11} Nm/rad to 2.88×10^{-11} Nm/rad when length

increased from 200µm to 450µm. The torsional spring constant of cantilever design C reduced as the length increased for the three materials as shown in the Figure 4.14.

Table 4.8 Parameters and values used in the investigation of length on torsional spring constant

Parameter	L1 (µm)	L2 (µm)	L3 (µm)	w1 (µm)	w2 (µm)	w3 (µm)	t (µm)
Range	180, 225, 270, 315, 360, 405	$\frac{1}{9}$L1	0.8×(L1+L2)	90	30	24	0.6

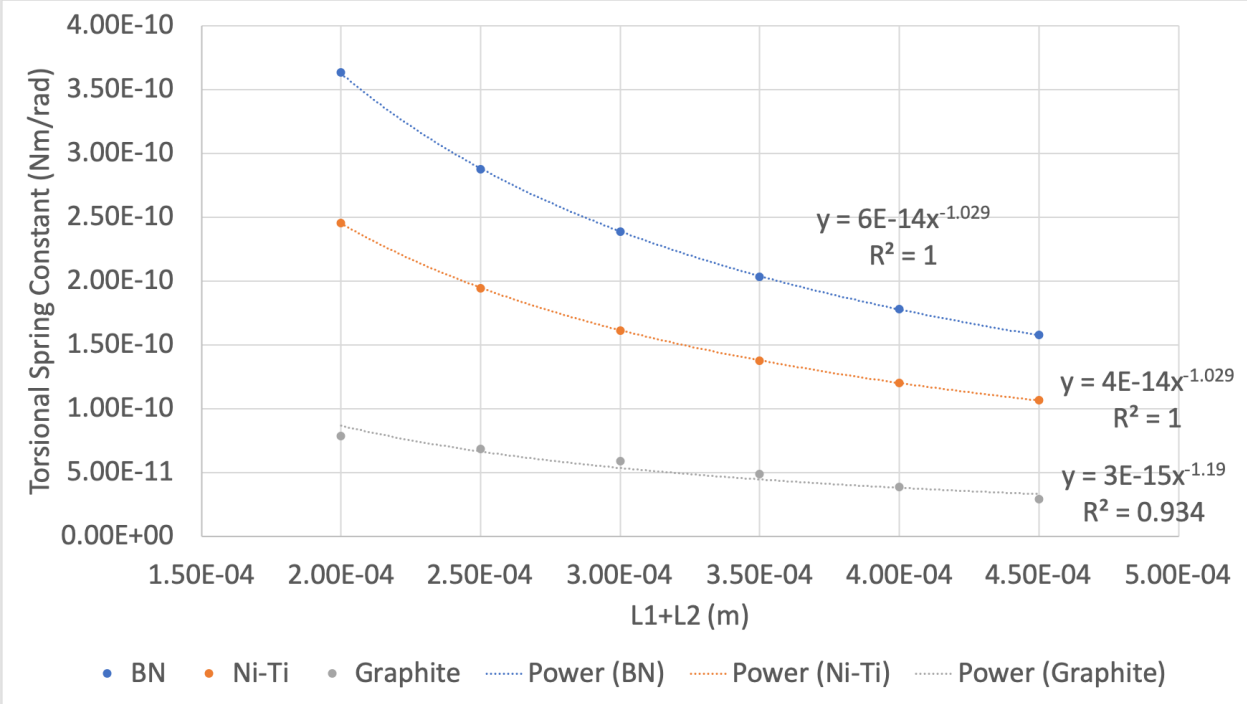

Figure 4.14 Cantilever design C: the effect of total length on torsional spring constant for three materials

The relationship between torsional spring constant of cantilever C and the width of the hammerhead wing (w1 in Figure 3.4) was demonstrated in the Figure 4.15. The parameters and the corresponding values used in the test are listed in Table 4.9. The torsional spring constant of cantilever design C made from the boron nitride increased from the 9.57×10^{-11} Nm/rad to 3.15×10^{-10} Nm/rad when width went up from 45µm to 120µm. The torsional spring constant

made from Ni-Ti alloy increased from 9.57×10^{-11} Nm/rad to 2.13×10^{-10} Nm/rad when width changed from 45µm to 120µm. The torsional spring constant made from graphite ranged from 2.52×10^{-11} Nm/rad to 8.29×10^{-11} Nm/rad when width increased from 45µm to 120µm. The trendlines of the torsional spring constant with the variation of width in Figure 4.15 suggested that the torsional spring constant of cantilever design C went up with the increase of the width for the three materials.

Table 4.9 Parameters and values used in the investigation of length on torsional spring constant

Parameter	L1 (µm)	L2 (µm)	L3 (µm)	w1 (µm)	w2 (µm)	w3 (µm)	t (µm)
Range	300	33	267	45, 60, 75, 90, 105, 120	$\frac{1}{3}$w1	0.8×w2	0.6

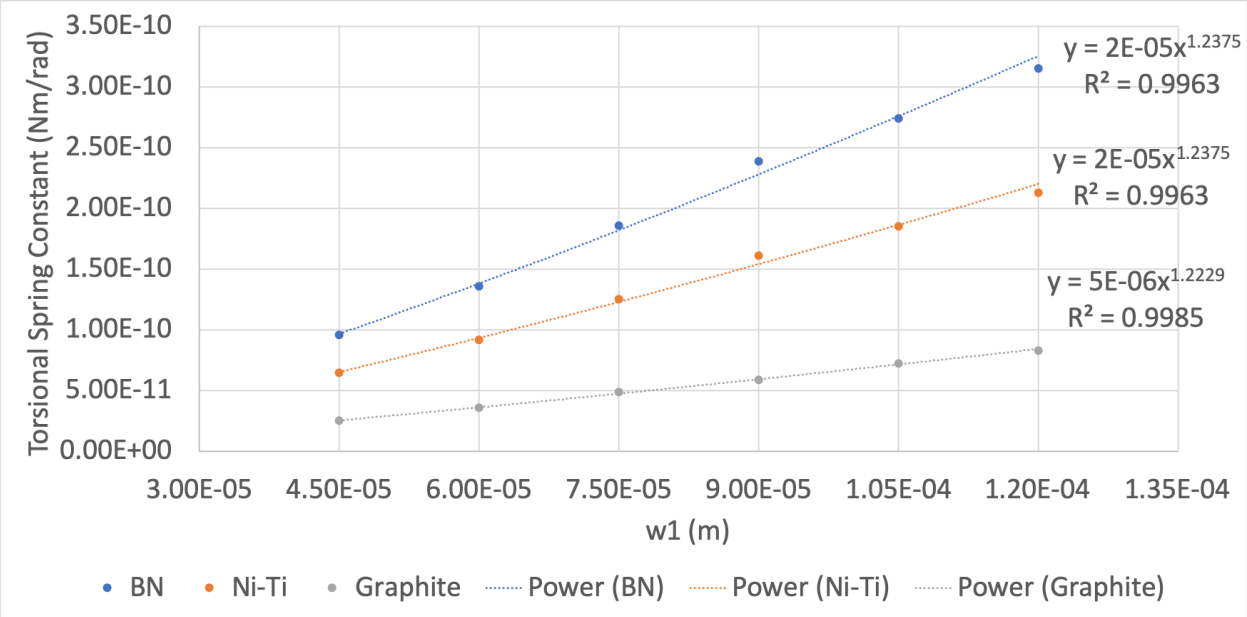

Figure 4.15 Cantilever design C: the effect of width of hammerhead wing on torsional spring constant for three materials

The relationship between the torsional spring constant and the cantilever thickness (t in Figure 3-4) of design C was expressed by a polynomial function. The parameters and the

corresponding values used in the test are listed in Table 4.10. The torsional spring constant of cantilever design C made from the boron nitride increased from the 2.38×10^{-10} Nm/rad to 3.01×10^{-10} Nm/rad when thickness increased from 0.6 μm to 0.8 μm. The torsional spring constant made from Ni-Ti alloy increased from 1.61×10^{-10} Nm/rad to 2.40×10^{-10} Nm/rad when thickness increased from 0.6 μm to 0.8 μm. The torsional spring constant made from graphite ranged from 5.85×10^{-11} Nm/rad to 6.87×10^{-11} Nm/rad when thickness changed from 0.6μm to 0.8μm. The trendlines of the torsional spring constant with the variation of width in Figure 4.16 illustrated that the torsional spring constant of cantilever design C increased with the increment of thickness. The torsional spring constants of three materials showed the same pattern as the Section 4.2.1 and 4.2.2, the cantilevers made from graphite had the lowest torsional spring constants while the boron nitride turned out to be the most rigid material in the torsional direction among the three materials and Ni-Ti alloy fell in the middle.

Table 4.10 Parameters and values used in the investigation of thickness on torsional spring constant

Parameter	L1 (μm)	L2 (μm)	L3 (μm)	w1 (μm)	w2 (μm)	w3 (μm)	t (μm)
Range	300	33	267	90	30	24	0.6, 0.64, 0.68, 0.72, 0.76, 0.8

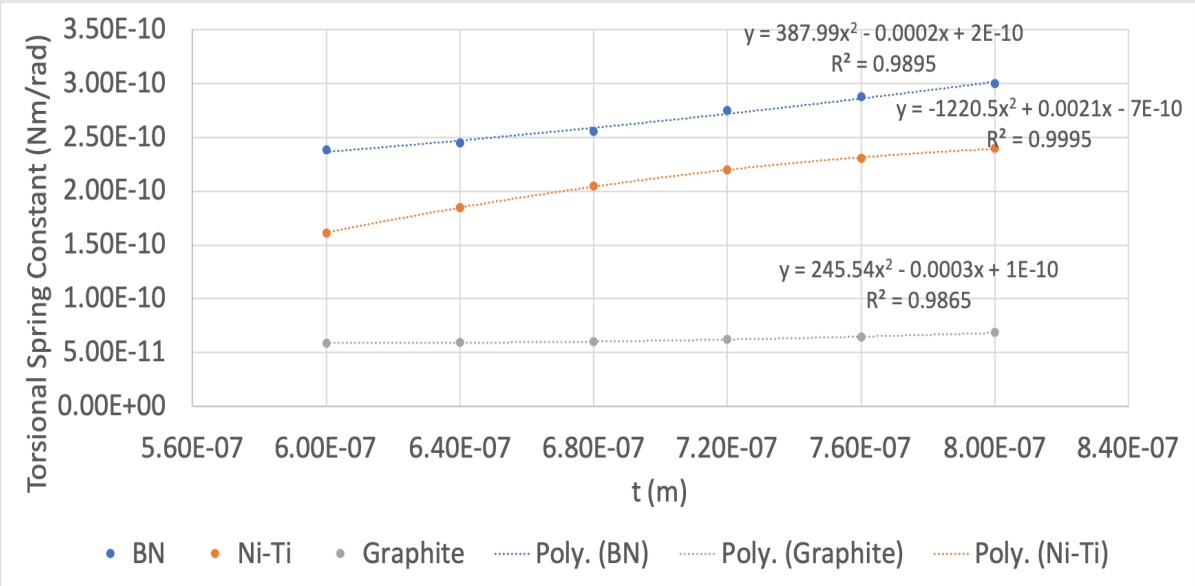

Figure 4.16 Cantilever design C: the effect of thickness on torsional spring constant for three materials

4.2.4 The torsional spring constant of design D

The effects of the geometric parameters on the torsional spring constant within the test ranges shown in Table 3.4 for three materials were studied. Figure 4.17 shows the torsional spring constant of design D in a power function of the total cantilever length (L in Figure 3.5). The parameters and the corresponding values used in the test are listed in Table 4.11. The torsional spring constant of cantilever design D made from the boron nitride decreased from the 5.87×10^{-9} Nm/rad to 2.58×10^{-9} Nm/rad when total length varied from 200µm to 450µm. The torsional spring constant made from Ni-Ti alloy decreased from 4.88×10^{-9} Nm/rad to 2.29×10^{-9} Nm/rad when length increased from 200µm to 450µm. The torsional spring constant made from graphite decreased from 3.75×10^{-9} Nm/rad to 1.88×10^{-9} Nm/rad as length increased from 200µm to 450µm. The torsional spring constant of cantilever design D went down as the length increased for the three materials as shown in the Figure 4.17.

Table 4.11 Parameters and values used in the investigation of length on torsional spring constant

Parameter	L (μm)	w1(μm)	w2 (μm)	t (μm)	h (μm)
Range	200, 250, 300, 350, 400, 450	30	2	0.6	10

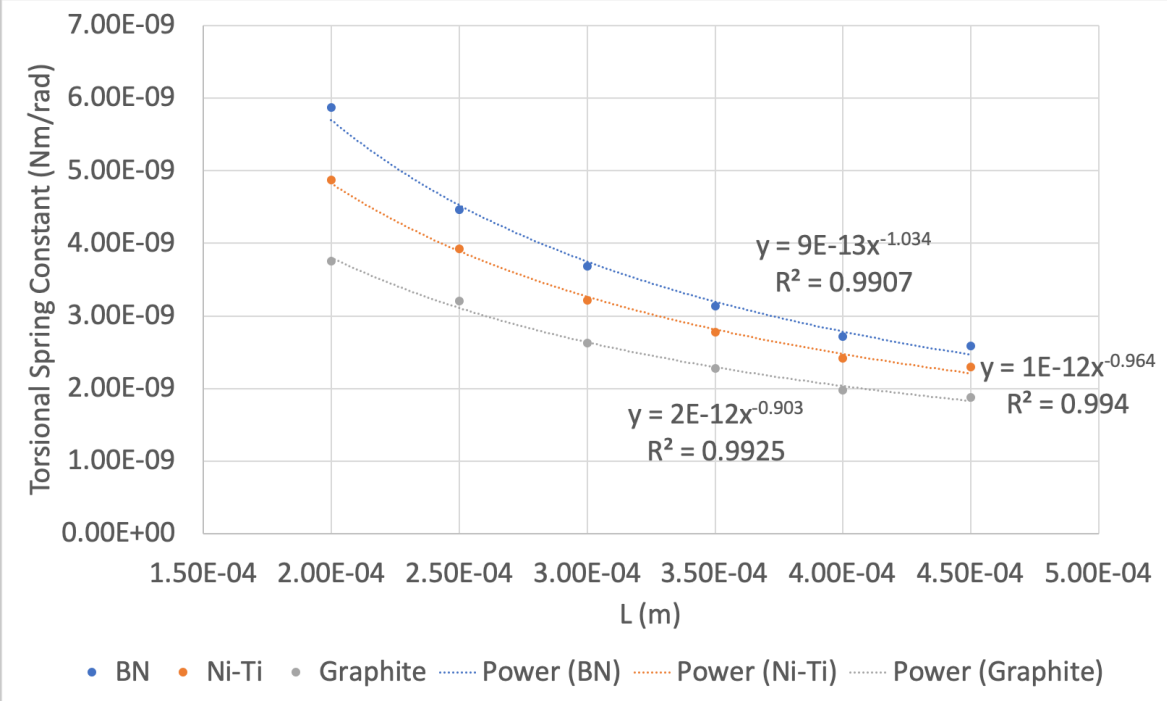

Figure 4.17 Cantilever design D: the effect of length on torsional spring constant for three materials

The relationship between torsional spring constant of cantilever D and the width of the horizontal beam (w1 in Figure 3-5) is demonstrated in the Figure 4.18. The parameters and the corresponding values used in the test are listed in Table 4.12. The torsional spring constant of cantilever design D made from the boron nitride decreased from the 4.67×10^{-9} Nm/rad to 2.80×10^{-9} Nm/rad when width of the horizontal beam went up from 15μm to 40μm. The torsional spring constant made from Ni-Ti alloy decreased from 4.22×10^{-9} Nm/rad to 2.58×10^{-9} Nm/rad when width changed from 15 μm to 40 μm. The torsional spring constant made from graphite dropped from 3.41×10^{-9} Nm/rad to 2.14×10^{-9} Nm/rad when width increased from

15µm to 40µm. The trendlines of the torsional spring constant with the variation of width in Figure 4.18 suggested that the torsional spring constant of cantilever design D decreased with the increase of the width for the three materials.

Table 4.12 Parameters and values used in the investigation of the horizontal beam width on torsional spring constant

Parameter	L (µm)	w1(µm)	w2 (µm)	t (µm)	h (µm)
Range	300	15, 20, 25, 30, 35, 40	2	0.6	10

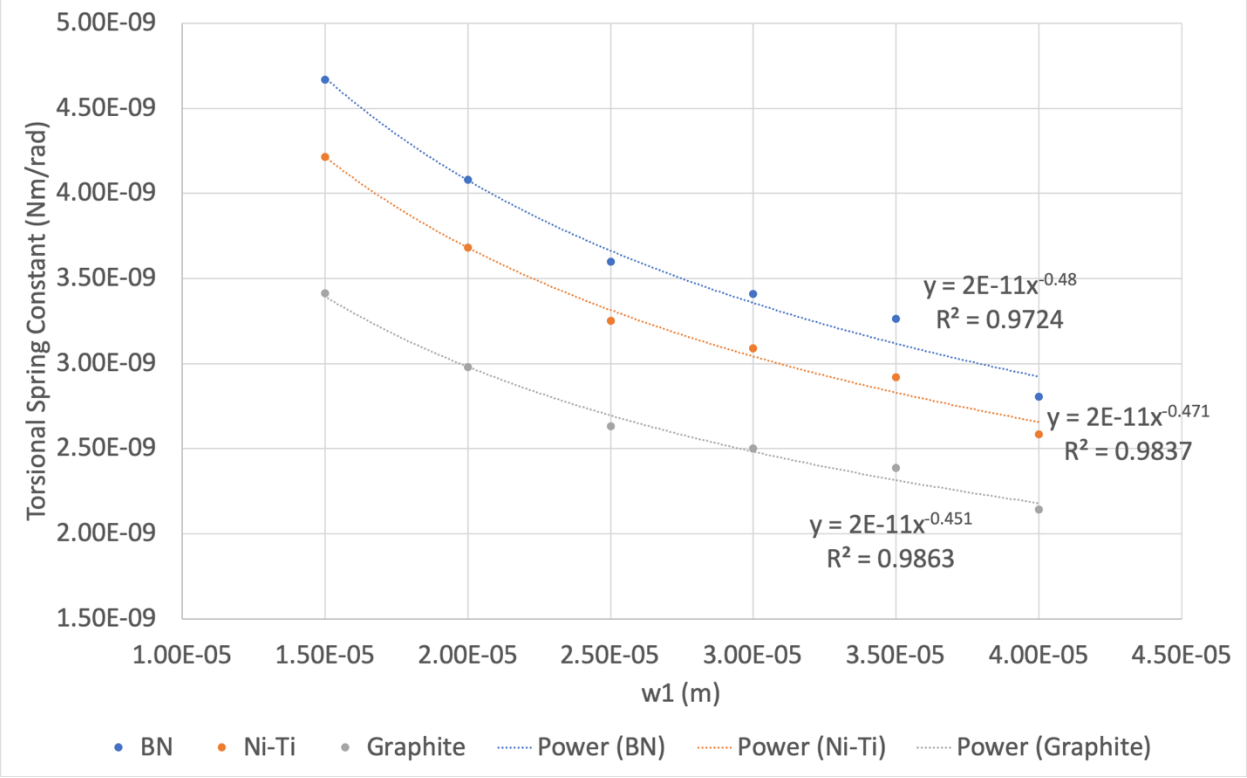

Figure 4.18 Cantilever design D: the effect of width of the horizontal beam on torsional spring constant for three materials

The relationship between torsional spring constant of cantilever D and the width of the vertical beam (w2 in Figure 3-5) is demonstrated in the Figure 4.19. The parameters and the

corresponding values used in the test are listed in Table 4.13. The torsional spring constant of cantilever design D made from the boron nitride increased from the 3.68 × 10^{-9} Nm/rad to 5.89 × 10^{-9} Nm/rad when width of the vertical beam went up from 2μm to 12μm. The torsional spring constant made from Ni-Ti alloy went up from 3.21 × 10^{-9} Nm/rad to 5.35× 10^{-9} Nm/rad when width changed from 2 μm to 12 μm. The torsional spring constant made from graphite ranged from 2.63 × 10^{-9} Nm/rad to 4.29 × 10^{-9} Nm/rad when width increased from 2 μm to 12 μm. The trendlines of the torsional spring constant with the variation of vertical beam width in Figure 4.19 suggested that the torsional spring constant of cantilever design D increased with the increase of the width for the three materials.

Table 4.13 Parameters and values used in the investigation of the vertical beam width on torsional spring constant

Parameter	L (μm)	w1(μm)	w2 (μm)	t (μm)	h (μm)
Range	300	30	2, 4, 6, 8, 10, 12	0.6	10

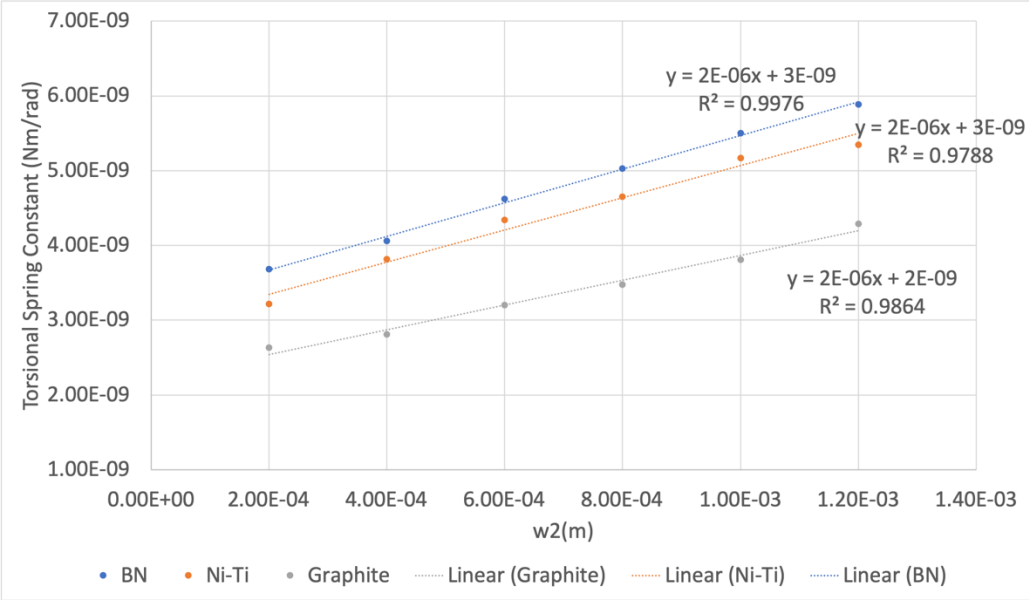

Figure 4.19 Cantilever design D: the effect of width of the vertical beam on torsional spring constant for three materials

The relationship between the torsional spring constant and the thickness of the horizontal beam (t in Figure 3.5) of design D expressed by a polynomial function. The parameters and the corresponding values used in the test are listed in Table 4.14. The torsional spring constant of cantilever design D made from the boron nitride increased from the 3.68×10^{-9} Nm/rad to 5.33×10^{-9} Nm/rad when thickness of the horizontal beam increased from 0.6 μm to 0.8 μm. The torsional spring constant made from Ni-Ti alloy increased from 3.21×10^{-9} Nm/rad to 4.87×10^{-9} Nm/rad when thickness increased from 0.6 μm to 0.8 μm. The torsional spring constant made from graphite increased from 2.63×10^{-9} Nm/rad to 3.87×10^{-9} Nm/rad when thickness changed from 0.6μm to 0.8μm. The trendlines of the torsional spring constant with the variation of horizontal beam thickness in Figure 4.20 illustrated that the torsional spring constant of cantilever design D increased as the thickness of the horizontal beam increased.

Table 4.14 Parameters and values used in the investigation of the horizontal beam thickness on torsional spring constant

Parameter	L (μm)	w1(μm)	w2 (μm)	t (μm)	h (μm)
Range	300	30	2	0.6, 0.64, 0.68, 0.72, 0.76, 0.8	10

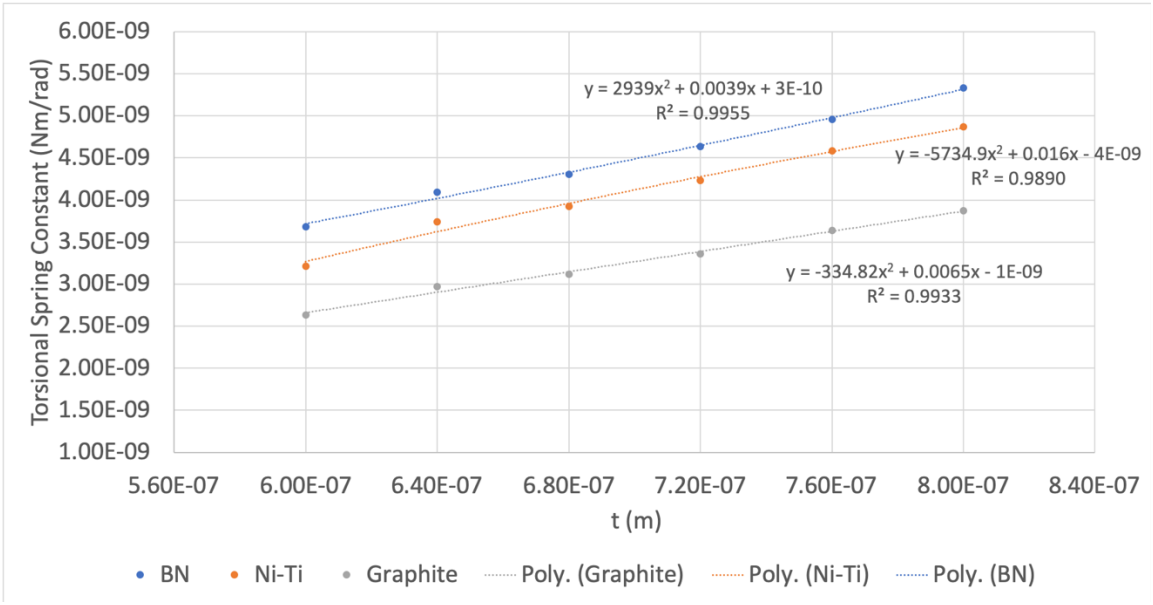

Figure 4.20 Cantilever design D: the effect of thickness of the horizontal beam on torsional spring constant for three materials

The relationship between the torsional spring constant and the height of the vertical beam (h in Figure 3-5) of design D expressed by a polynomial function. The parameters and the corresponding values used in the test are listed in Table 4.15. The torsional spring constant of cantilever design D made from the boron nitride increased from the 2.04×10^{-9} Nm/rad to 5.61×10^{-9} Nm/rad when height of the vertical beam increased from 5 µm to 15 µm. The torsional spring constant made from Ni-Ti alloy increased from 1.85×10^{-9} Nm/rad to 5.09×10^{-9} Nm/rad when height increased from 5 µm to 15 µm. The torsional spring constant made from graphite increased from 1.50×10^{-9} Nm/rad to 4.12×10^{-9} Nm/rad when height changed from 5 µm to 15 µm. The trendlines of the torsional spring constant with the variation of vertical beam height in Figure 4.21 suggested that the torsional spring constant of cantilever design D increased as the height of the vertical beam became larger. As shown in the five figures in this section, the cantilevers made from graphite had the lowest torsional spring constants while the

boron nitride turned out to be the most rigid material in the torsional direction among the three materials and Ni-Ti alloy ranked the second.

Table 4.15 Parameters and values used in the investigation of the vertical beam height on torsional spring constant

Parameter	L (µm)	w1(µm)	w2 (µm)	t (µm)	h (µm)
Range	300	30	2	0.5	5, 7, 9, 11, 13, 15

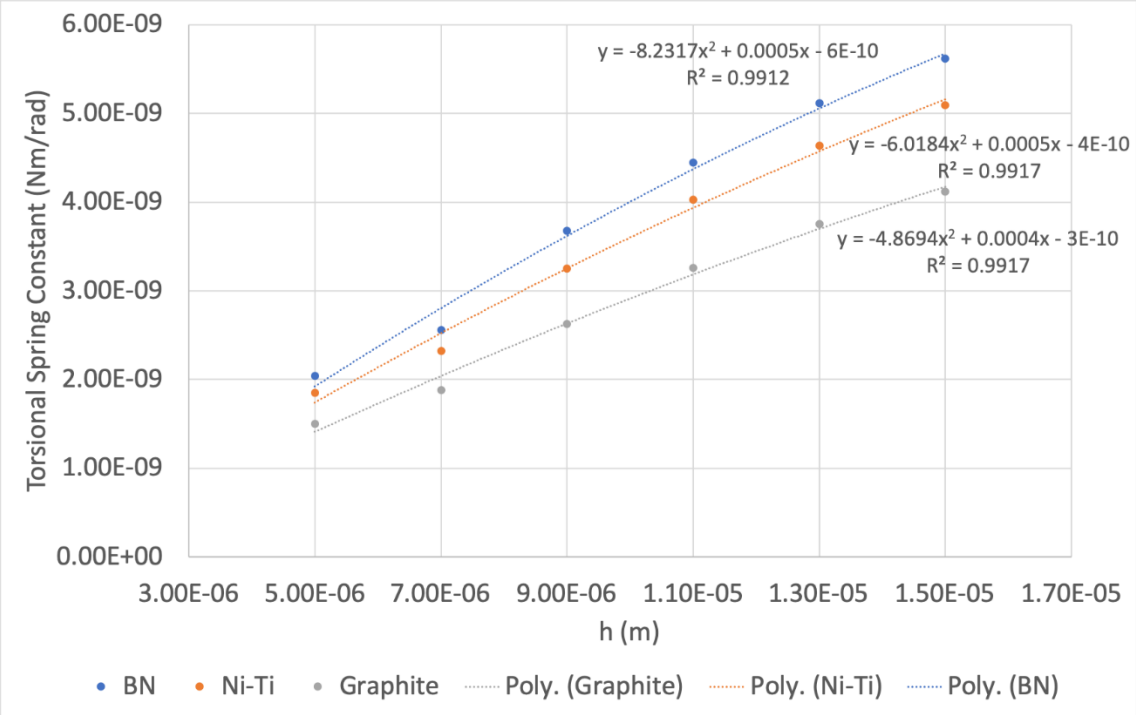

Figure 4.21 Cantilever design D: the effect of height of the vertical beam on torsional spring constant for three materials

4.2.5 The normal stiffness-torsional stiffness of cantilever design

The normal stiffness – torsional stiffness ratios of four cantilevers designs made from graphite were presented in the Figure 4.22. The ratio with the variation of cantilever length from 200µm to 450µm was calculated and plotted to compare the stiffness ratio at the same length for

the four designs. The testing parameters and values for the four cantilever designs A, B, C, and D utilized in this section were listed in the Table 4.1, 4.4, 4.8, and 4.11 respectively.

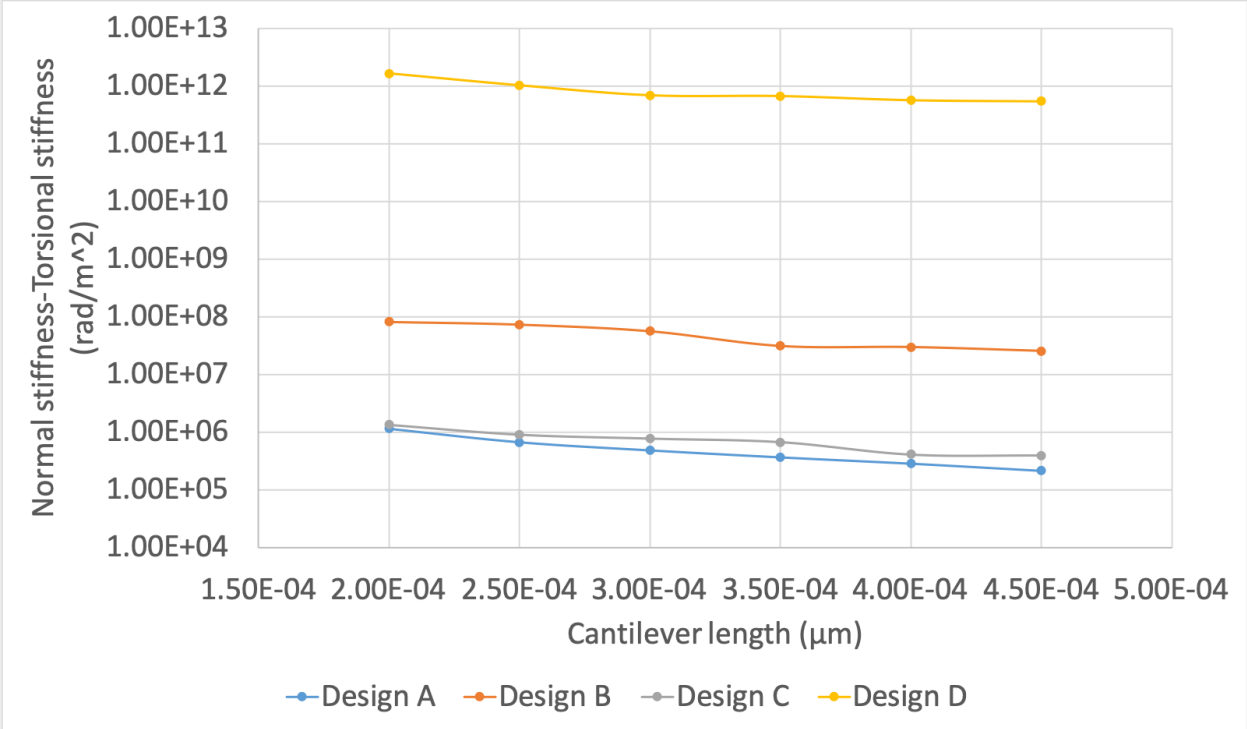

Figure 4.22 The normal stiffness – torsional stiffness ratio of four cantilever designs made from graphite with the variation of cantilever length.

The ratio of normal stiffness to torsional stiffness of design A ranged from 2.16×10^{5} rad/m^2 to 1.15×10^{6} rad/m^2, which ranked the lowest among the four cantilever designs. The design D had the highest ratio with the range from 5.49×10^{11} rad/m^2 to 1.65×10^{12} rad/m^2, which suggested that the design D was extremely stiff in normal direction while fairly flexible in the torsional directions. The design B's ratio ranged from 2.56×10^{7} rad/m^2 to 8.23×10^{7} rad/m^2 and the design C's ratio ranged from 3.98×10^{5} rad/m^2 to 1.45×10^{6} rad/m^2, ranking the second and

third place respectively. A negative correlation was also observed between the ratio and the cantilever length for all the four designs.

4.2.6 Summary of the cantilever design

According to the data from the Section 4.2.1 to 4.2.4, the cantilevers made from graphite had the lowest torsional spring constants while the boron nitride turned out to be the most rigid material in the torsional direction among the three materials and Ni-Ti alloy fell in the middle. Thus, graphite was identified as the promising material to produce cantilevers with lowest torsional spring constant and was chosen for further tip design investigation. The other two materials were eliminated from further study.

The cantilever design A and cantilever design D was chosen for the further measurement sensitivity evaluation in the Section 4.3 because design A had the lowest torsion spring constant and design D provided the highest normal stiffness-torsional stiffness ratio among the four designs. According to data analysis in the Section 4.2, when the length of the cantilever was 450μm, the width was 15μm, and the thickness was 0.6 μm, the cantilever design A would have the lowest torsional spring constant in the testing range proposed in the section 4.2.2, which would be 5.06×10^{-14} Nm/rad with the normal deflection percentage of 2.01% calculated by FEA. If the length of the cantilever was restricted to 300 μm when working conditions and equipment adaptability are considered, the torsional spring constant had the smallest value of 1.95×10^{-13} Nm/rad with width of 15μm and thickness of 0.6μm. The corresponding normal deflection is 0.4% of the whole cantilever length. When the length of the cantilever was 450μm, the width of the horizontal beam was 40μm, the thickness of the horizontal beam was 0.6μm, the height of the vertical beam was 5 μm, and the width of the vertical beam was 2μm, the cantilever design D would have the lowest torsional spring constant in the testing range proposed in the

section 4.2.2, which would be 3.47×10^{-10} Nm/rad with the normal deflection percentage of 8.31×10^{-3}%. If the length of the cantilever is restricted to 300 μm when working conditions and equipment adaptability are considered, the torsional spring constant has the smallest value of 4.27×10^{-9} Nm/rad and the corresponding normal deflection is 6.16×10^{-4}% of the whole cantilever length.

The cantilever design A (300μm long) with torsional spring constant of 1.95×10^{-13} Nm/rad and cantilever design D (300μm long) with torsional spring constant of 4.27×10^{-9} Nm/rad were utilized in the investigation of tip design. The two optimum cantilevers from the design A and design D were denoted as cantilever A and cantilever D respectively in the Section 4.3.

4.3 Tip Design Data

4.3.1 Measurement sensitivity on the hard sample

The measurement sensitivities of two tip designs with different tip apex radius were investigated by the simulation results from the contact model with the hard sample introduced in the Section 3.3.3. The measurement sensitivity was calculated by Eq. (3-3) using the tangential displacement of the cantilever and contact force between the tip and the sample. The measurement sensitivity of DNP tip was calculated as the control set by attaching it to the DNP cantilever, the cantilever A, and the cantilever D respectively. The data of the control set was demonstrated in the Table 4.16.

Table 4.16 The simulation results of twist angle (θ), contact force (F) and the measurement sensitivity (S) of the contact set on the hard sample

Tip type	Cantilever type	θ (rad)	F (N)	S (rad/N)
DNP tip	DNP V-shaped	1.47E-04	2.28E-08	6.45E+03
DNP tip	Cantilever A	7.43E-03	1.37E-06	5.41E+03
DNP tip	Cantilever D	1.25E-03	3.13E-08	3.98E+04

The measurement sensitivity of the DNP probe, was 3.87×10^{3} rad/N. The DNP tip with cantilever A and cantilever D had the measurement sensitivity of 5.41×10^{3} rad/N and 6.45×10^{3} rad/N respectively. The cantilever D with the DNP tip demonstrated the highest measurement sensitivity with the second largest twist angle. The DNP tip on the cantilever design D displayed largest twist angle but lowest measurement sensitivity because of the large contact force.

The simulation results of twist angle and resultant contact force of the two tip designs on the cantilever A with the variation of radius was presented in Figure 4.23 and Figure 4.24 respectively. A slight decrease in twist angle and contact force with the increment of sphere radius was observed because the increasing radius resulted in the decreasing lever arm distance when the total tip height was fixed and led to smaller cantilever torsion. The twist angle and contact force increased as the disk radius increased as shown in the Figure 4.24 due to the larger contact area. The fluctuation of the curves might be caused by the FEA simulation error mentioned in the Section 3.6.

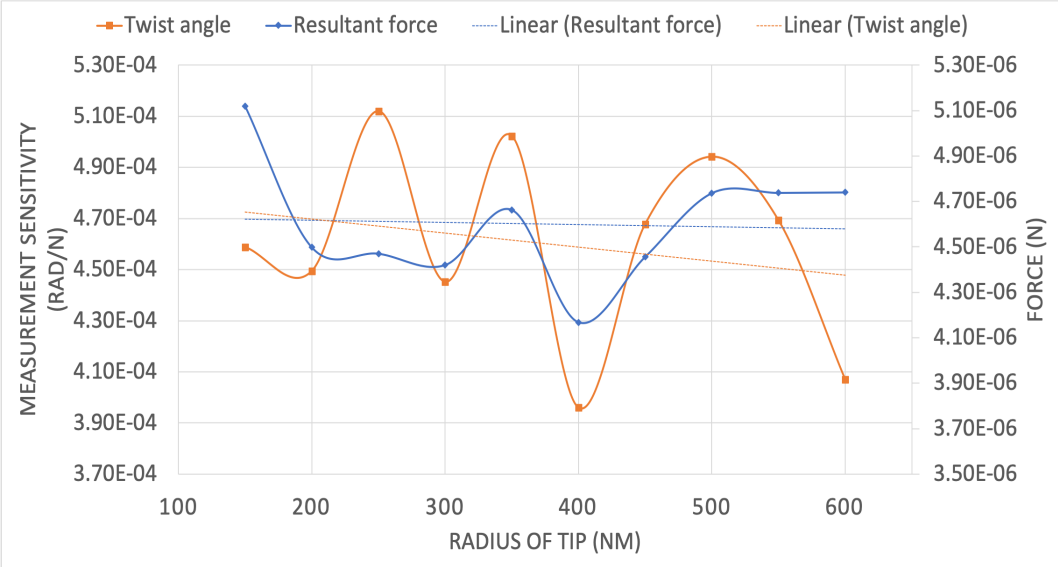

Figure 4.23 The twist angle and force with varied radius of tip design A on cantilever A with hard sample

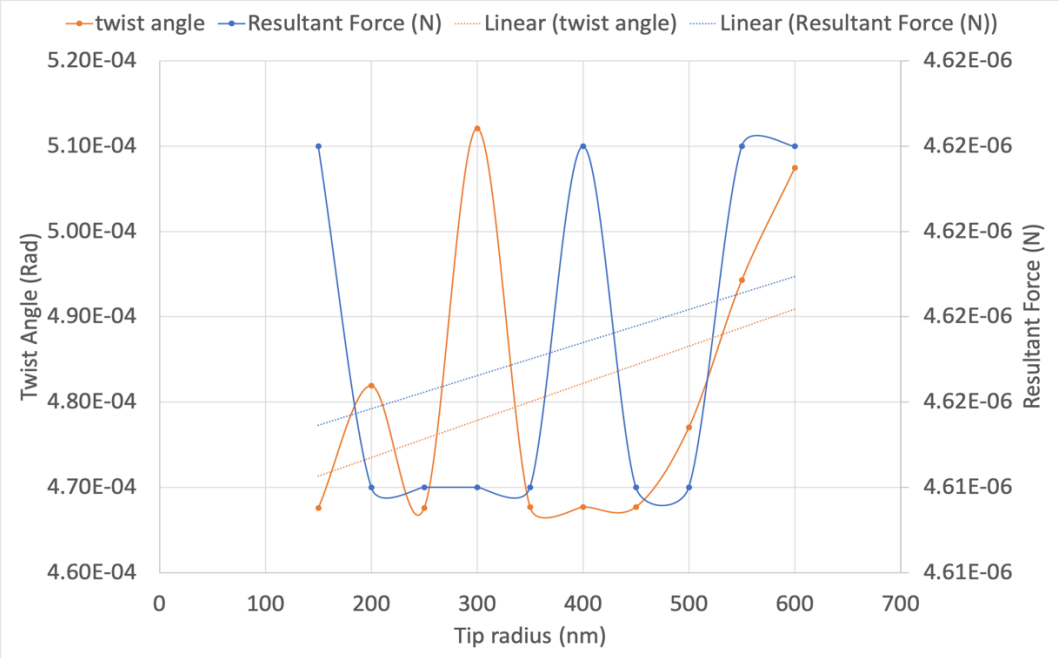

Figure 4.24 The twist angle and force with varied radius of tip design B on cantilever A with hard sample

The measurement sensitivities of tip design A and tip design B on the cantilever A with different radius were plotted in Figure 4.25. The measurement sensitivity of tip design A ranged from 79.1 rad/N to 1.15 $\times 10^2$ rad/N and the measurement sensitivity of the tip design B ranged

from 1.01×10^2 rad/N to 1.11×10^3 rad/N. The measurement results suggested that both tip designs possessed smaller twist angle and lower measurement sensitivity compared to the normal DNP tip. This phenomenon resulted from the lack of gradient of the two tip designs. The DNP tip had an upward gradient leading to one side of the cantilever deflected upwards and producing a bigger off-plane deformation when it was pushed by the hard sample in lateral direction. However, when the tip designs proposed were contacted by the sample, they were pushed directly in lateral direction resulting in cantilever deflect in the horizontal plane instead of twisting.

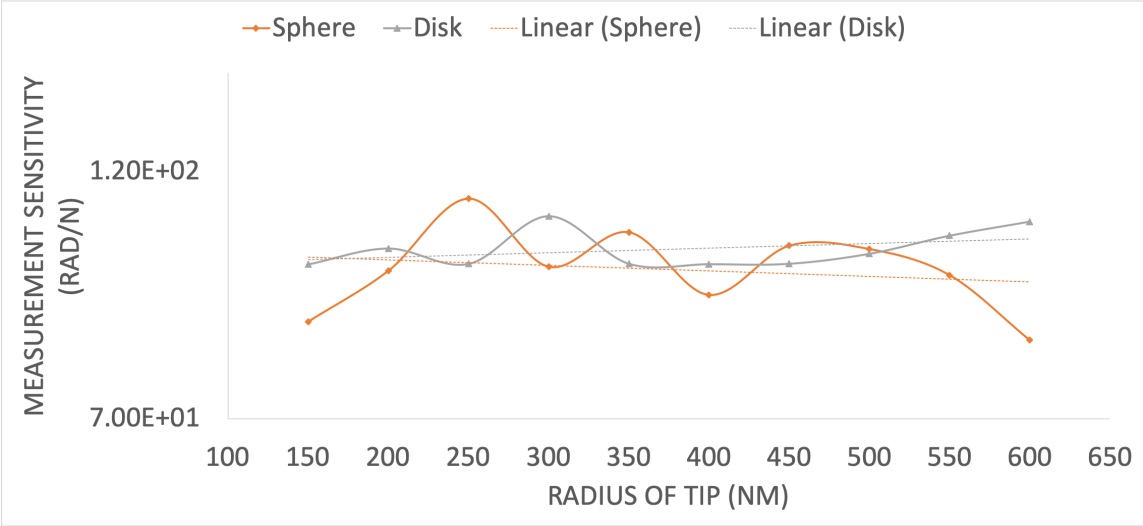

Figure 4.25 The measurement sensitivity of the two tip designs on cantilever A and hard sample: tip design A-sphere apex; tip design B-disk apex.

The effect of the radius of sphere and disk on measurement sensitivity on hard sample was observed from the dash linear trendlines in Figure 4.25. The measurement sensitivity of tip design A on a hard sample decreased slowly with the increment of radius due to the decreasing lever arm distance. The measurement sensitivity of design B on a hard sample increased with increasing contact area.

The simulation results of twist angle and contact force of the two tip designs on the cantilever D was presented in Figure 4.26 and 4.27. The contact force and the twist angle with the variation of radius of both tip design A and B on cantilever D showed the same phenomenon compared with the tips on cantilever A. A slight decrease in twist angle and contact force with the increment of sphere radius was observed because the increasing radius resulted in the decreasing lever arm distance when the total tip height was fixed and led to smaller cantilever torsion. The twist angle and contact force increased as the disk radius increased as shown in the Figure 4.27 due to the larger contact area.

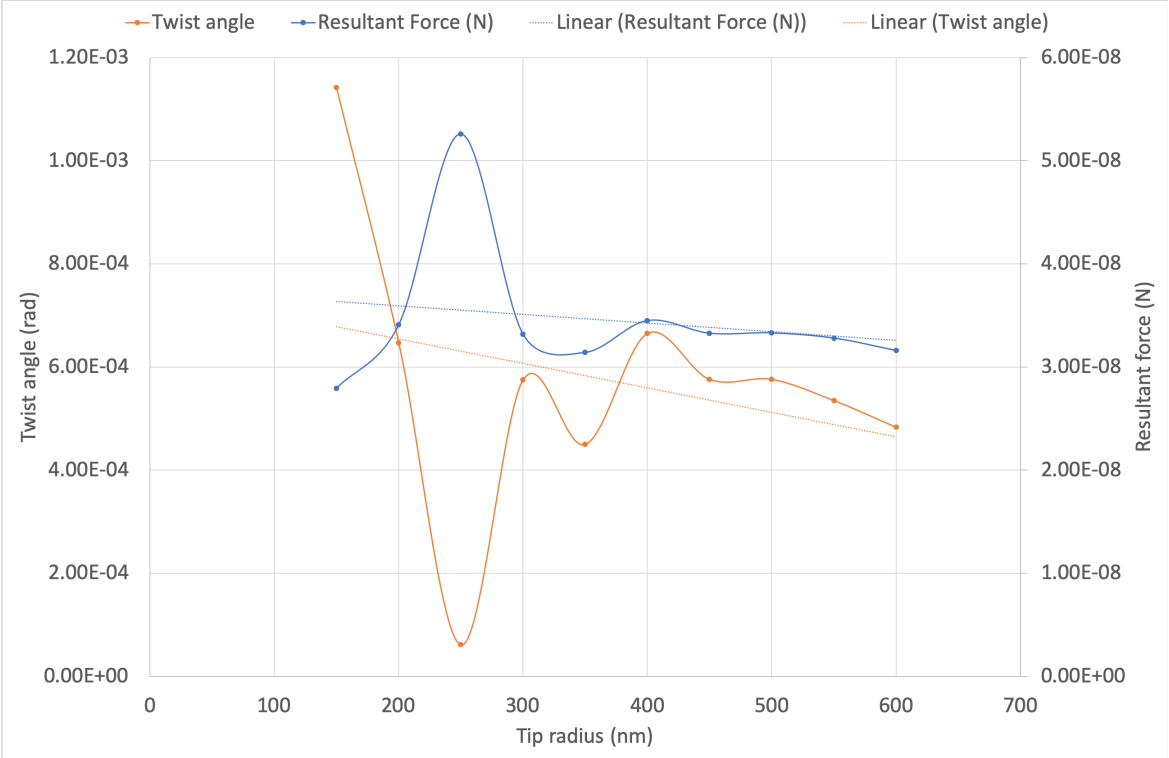

Figure 4.26 The twist angle and force with varied radius of tip design B on cantilever D with hard sample

Figure 4.27 The twist angle and force with varied radius of tip design B on cantilever D with hard sample

The measurement sensitivities of tip design A and tip design B on the cantilever D with different radius were plotted in Figure 4.28. The measurement sensitivity of tip design A ranged from 1.17×10^3 rad/N to 4.09×10^4 rad/N and the measurement sensitivity of the tip design B ranged from 2.06×10^3 rad/N to 4.14×10^4 rad/N. The measurement results suggest that both tip designs had lower measurement sensitivity compared to the DNP tip with cantilever D due to the lack of gradient on tips.

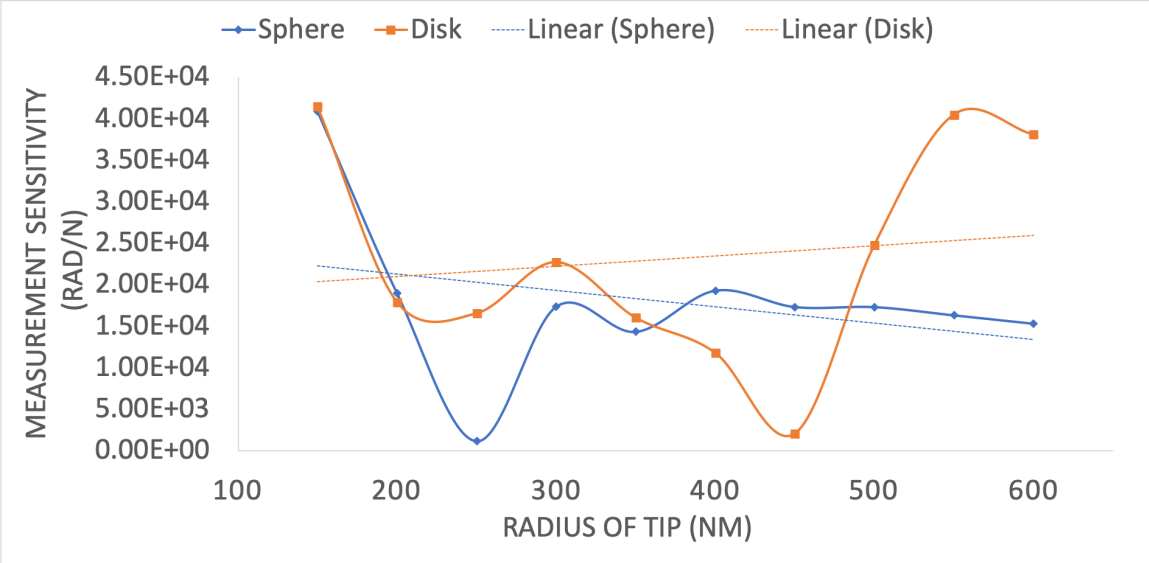

Figure 4.28 The measurement sensitivity of the two tip designs on cantilever D and hard sample: tip design A-sphere apex; tip design B-disk apex.

Similar to the measurement sensitivity done on cantilever A, the measurement sensitivity of tip design A on a hard sample decreased slowly with the increment of radius due to the decreasing lever arm distance. The measurement sensitivity of design B on a hard sample increased with increasing contact area. No matter which tip designs were studied, the cantilever D provided larger twist angle and higher measurement sensitivity in the contact process than cantilever A even though cantilever D had larger torsional spring constant. The reason might be that the cantilever A was too flexible in the lateral direction so that when the tip was pushed in the lateral direction, the cantilever tended to have larger in-plane displacement in the lateral direction instead of the torsional, causing the smaller twist angle.

4.3.2 Measurement sensitivity study on soft samples

The measurement sensitivities of two tips were also investigated on the soft sample introduced in the section 3.3.3. The control set introduced in the Section 4.3.1 was also measured for comparison and the results was presented in the Table 4.17.

Table 4.17 The simulation results of twist angle (θ), contact force (F) and the measurement sensitivity (S) of the contact set on the soft sample

Tip type	**Cantilever type**	$\boldsymbol{\theta}$ **(rad)**	$\boldsymbol{F}$ **(N)**	$\boldsymbol{S}$ **(rad/N)**
DNP tip	DNP V-shaped	3.34E-05	3.61E-09	9.24E+03
DNP tip	Cantilever A	2.23E-05	2.38E-08	9.38E+02
DNP tip	Cantilever D	8.90E-05	3.13E-09	2.85E+04

The measurement sensitivity of the DNP probe was 1.92×10^4 rad/N. The DNP tip on the cantilever A and cantilever D had measurement sensitivity of 9.38×10^2 rad/N and 2.85×10^4 rad/N respectively. The cantilever D showed the largest twist angle and highest measurement sensitivity among the three contact sets.

The simulation results on the soft sample of twist angle, contact force, and the measurement sensitivity of the two tip designs on the cantilever A was presented in Figure 4.29 and 4.30. Both the twist angle and the contact force increased slightly with the increment of tip apex radius for tip design A and B due to the increasing contact area.

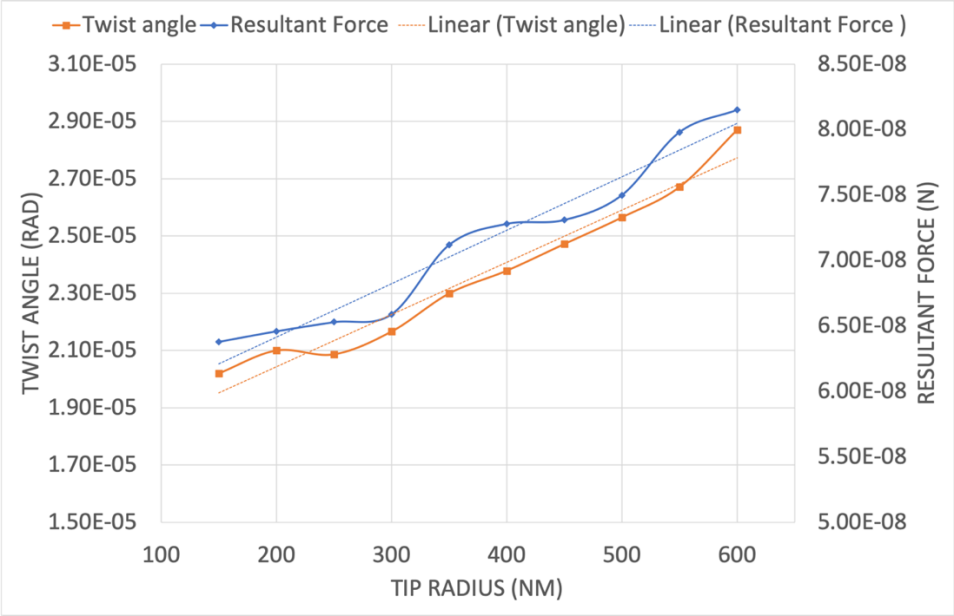

Figure 4.29 The twist angle and force with varied radius of tip design A on cantilever A with soft sample

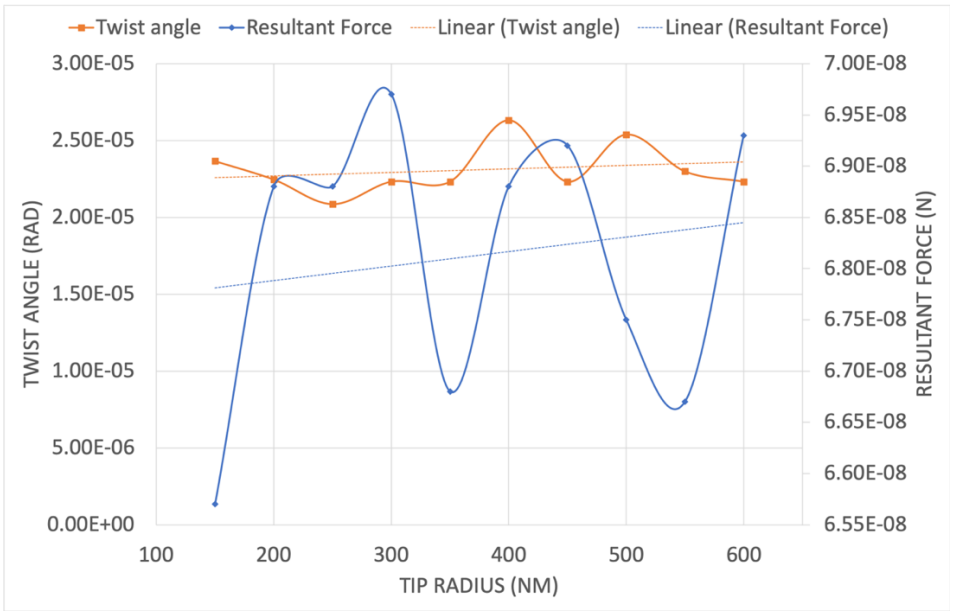

Figure 4.30 The twist angle and force with varied radius of tip design B on cantilever A with soft sample

The measurement sensitivities of tip design A and tip design B on the cantilever A with different radius accomplished on the soft sample were plotted in Figure 4-17. The measurement

sensitivity of tip design A went up from 3.17×10^2 rad/N to 3.52×10^2 rad/N as the tip radius increased from 150nm to 600nm. The measurement sensitivity of the tip design B on the cantilever A fluctuated from 3.03×10^2 rad/N to 3.82×10^3 rad/N as the tip radius changed. The measurement results suggest that both tip designs possessed lower measurement sensitivity on the soft sample compared to the normal DNP tip.

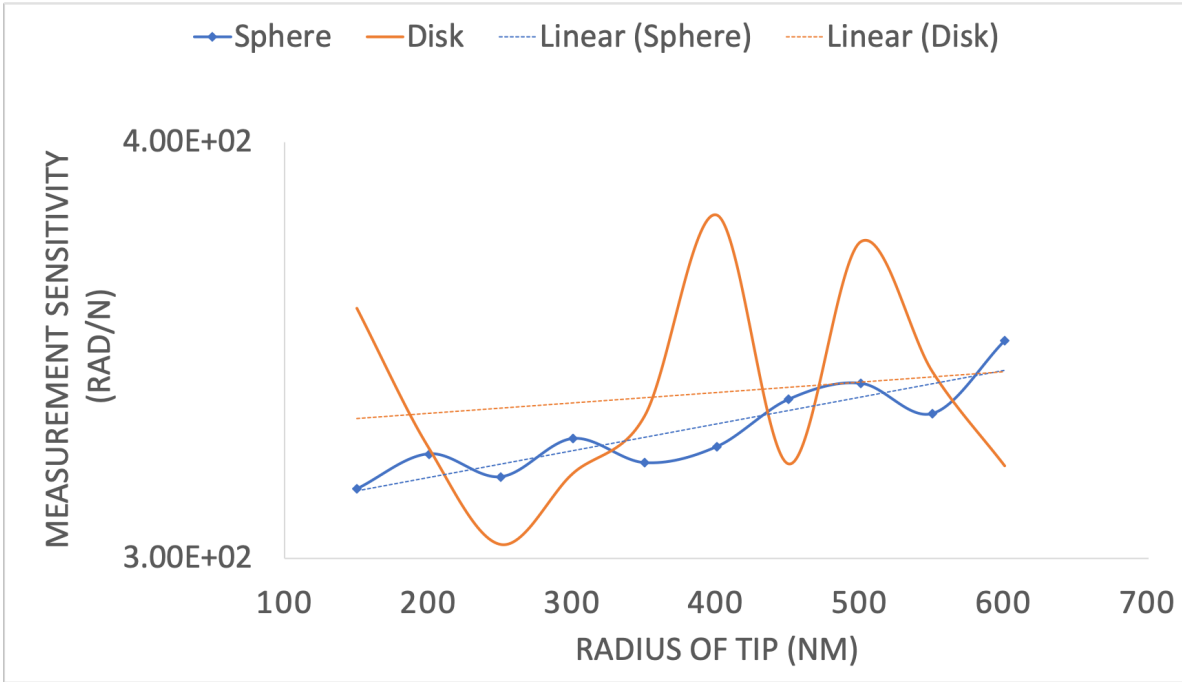

Figure 4.31 The measurement sensitivity of the two tip designs on cantilever A and soft sample: tip design A-sphere apex; tip design B-disk apex.

The simulation results on the soft sample of twist angle and contact force of the two tip designs on the cantilever D was presented in Figure 4.32 and 4.33. Both the twist angle and the contact force increased slightly with the increment of tip apex radius for tip design A and B due to the increasing contact area.

Figure 4.32 The twist angle and force with varied radius of tip design A on cantilever D with soft sample

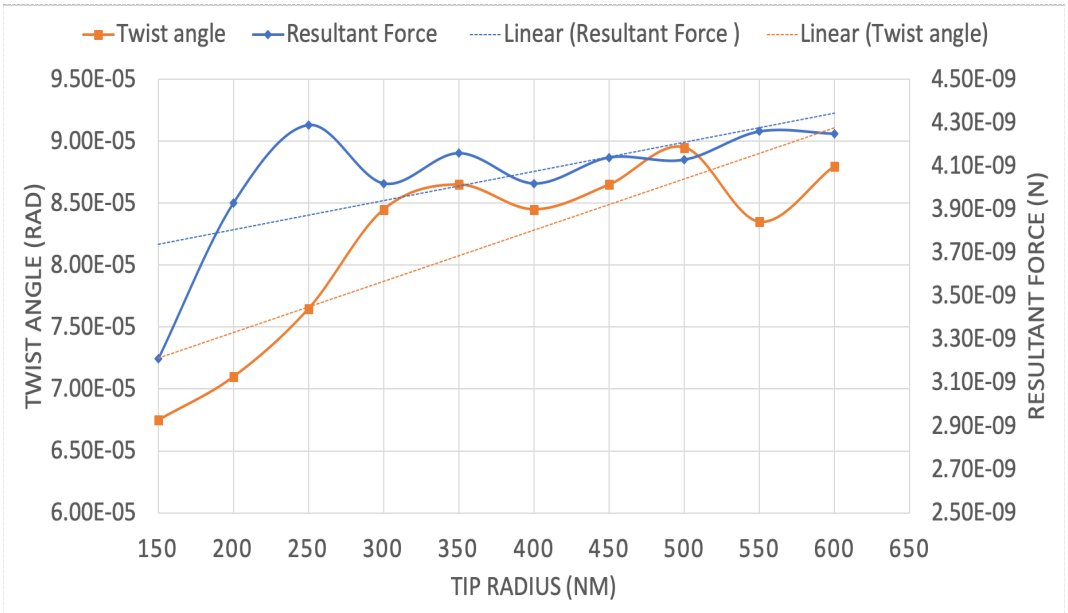

Figure 4.33 The twist angle and force with varied radius of tip design B on cantilever D with soft sample

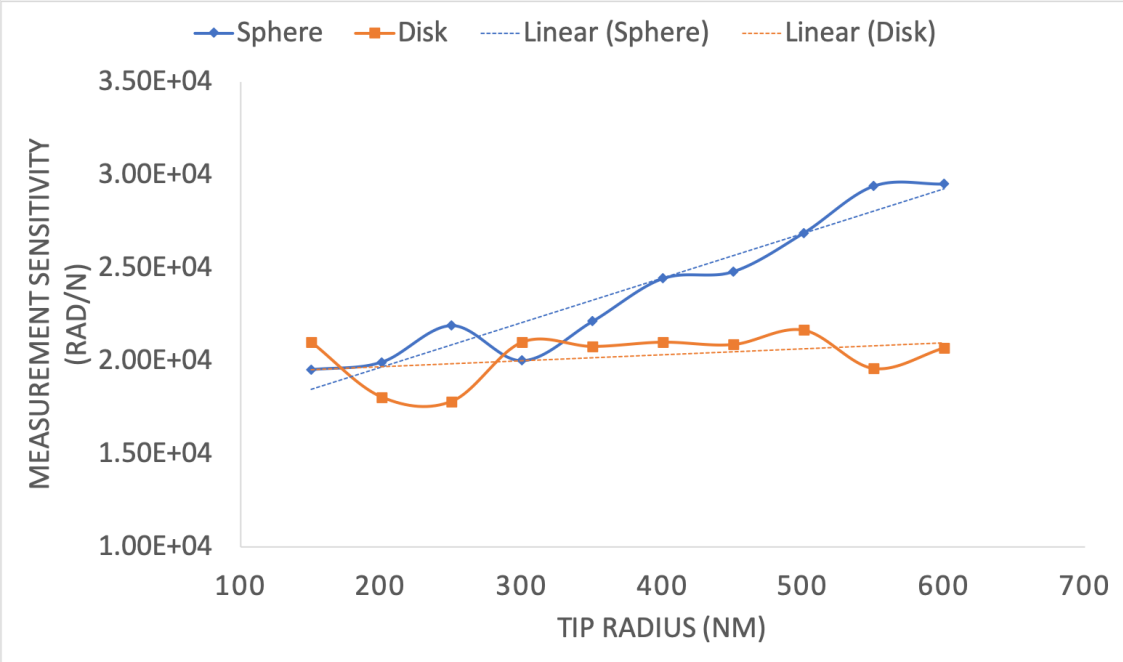

Figure 4.34 The measurement sensitivity of the two tip designs on cantilever D and soft sample: tip design A-sphere apex; tip design B-disk apex.

The measurement sensitivities of tip design A and tip design B on the cantilever D with different radius accomplished on the soft sample were plotted in Figure 4.32. The measurement sensitivity of tip design A went up from 1.95×10^4 rad/N to 2.95×10^4 rad/N as the tip radius increased from 150nm to 600nm. The measurement sensitivity of the tip design B on the cantilever A fluctuated from 1.78×10^4 rad/N to 2.1×10^4 rad/N as the tip radius changed indicating that the incremental rates of twist angle and contact force were similar. The measurement results of cantilever D suggested that the tip design B with the radius of 550 nm and 600 nm demonstrated higher lower measurement sensitivity on the soft sample compared with the normal DNP tip. The other experimental objectives had lower measurement sensitivity compared with the normal DNP tip.

4.3.3 Measurement sensitivity and the tip position

The effect of the distance from the tip to the cantilever free end was investigated on both tip design A and design B with the radius of 300 nm attached to the cantilever A. The trendline of the influence were demonstrated in the Figure 4.33. Tip position denoted the distance from the center of the tip base to the free end of the cantilever. The measurement sensitivity of tip design A dropped from 1.01×10^2 rad/N to 0.67×10^2 rad/N linearly as the distance increased from 4μm to 28μm. The linear function of the measurement sensitivity (y) as the tip position (x) could be written as y=-1.9121x+118.09. The measurement sensitivity of tip design B also decreased from 1.11×10^2 rad/N to 0.73×10^2 rad/N linearly as the distance increased from 4μm to 28μm. The linear function of the measurement sensitivity (y) as the tip position (x) could be written as y=-1.9094x+118.01. Thus, the tip should be attached close to the free end of the cantilever in order to obtain the optimum measurement sensitivity.

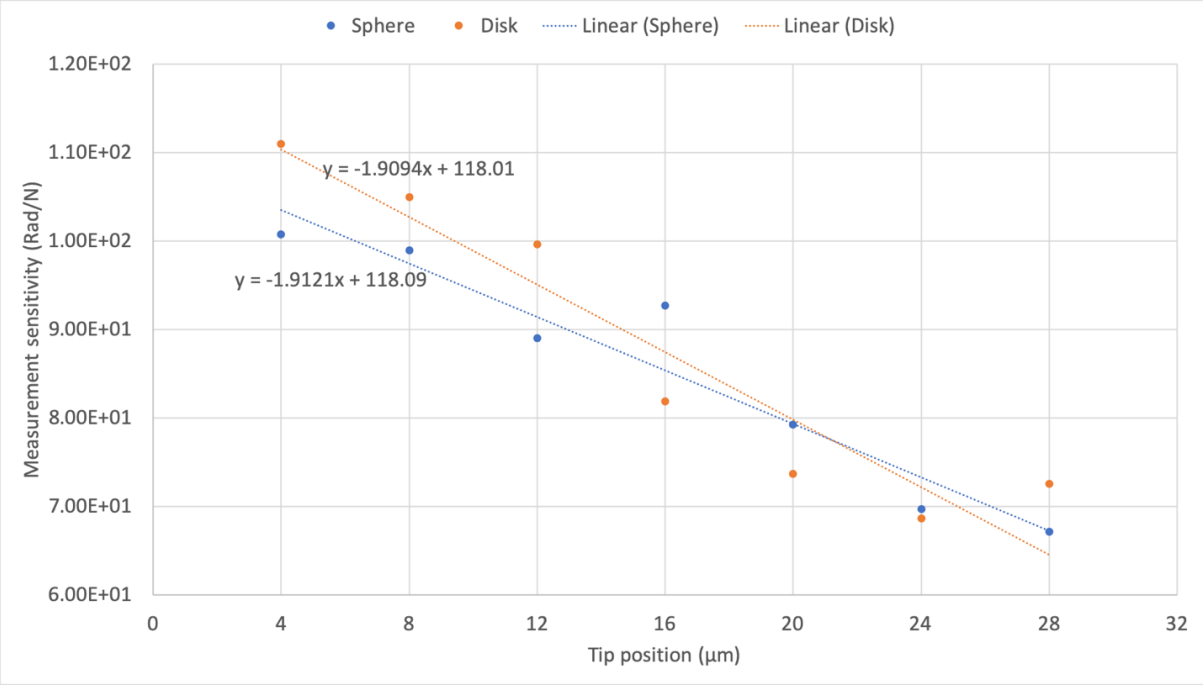

Figure 4.35 The relationship of the measurement sensitivity with the tip position on tip design A and tip design B on cantilever A

CHAPTER 5. SUMMARY, CONCLUSIONS, AND RECOMMENDATIONS

This chapter presents the summary and conclusions regarding the study of the effect of cantilever and tip design for mLFM. The discussion of the future work of the FEA of the cantilever-tip design and the microfabrication of graphite.

5.1 Summary

This paper displayed the simulation and calculation results and data analysis in this thesis. Starting from the model validation, the torsional spring constant measurements and the tip design data was demonstrated in this chapter. In the end, the optimum combination of the probe was summarized as following.

In summary, the optimum combination of the probe depends on the application and the type of the sample. In the investigation on the hard samples, the probe with the optimum measurement sensitivity was the combination of the cantilever D (horizonal beam width of 40μm, horizontal beam thickness of 0.6 μm, vertical beam height of 5μm, vertical beam width of 2μm, length 300μm) and a DNP tetrahedral tip (tip height of 2.5μm, side angle of 17.5 degree, tip position of 4μm), which had the measurement sensitivity of 3.98 ×104 rad/N. The probe consisting of the cantilever design D (horizonal beam width of 40μm, vertical height of 5μm, length 300μm) and the tip design A (sphere) with the radius of 600 nm had the optimum measurement sensitivity on the soft sample, which was 2.95×104 rad/N.

5.2 Conclusions

The results and data in section 4.1 demonstrated the feasibility of SolidWorks Prime simulation add-in package on the investigation regarding the deformation and mechanics of AFM and LFM probes. The model was validated with experimental results and analytical calculation of the cantilever mechanics. However, the limits of the SolidWorks simulation on nano-structures are also noticeable that the SolidWorks simulation is not able to process displacements smaller than 100 nm. Displacements or distances smaller than 100nm was found to be treated as zero when setting up the simulation by SolidWorks.

The cantilever-tip design results performed by FEA and linear regression shown in the section 4.2 and 4.3 demonstrated the optimum probe configuration of modified LFM with the best measurement sensitivity when conducted on a hard sample and a soft sample. The measurement sensitivity has been improved significantly compared to a DNP V-shaped probe. For the hard sample, the cantilever D and a DNP tip had the optimum measurement sensitivity of 3.98×10^4 rad/N, increasing the measurement sensitivity by 517.1%, compared to the DNP probe with the measurement sensitivity of 6.45×10^3 rad/N. For the soft sample, the cantilever D and the tip design A with the radius of 600 nm had the optimum measurement sensitivity of 2.95×10^4 rad/N, increasing the sensitivity by 219.3%, compared to DNP probe with the sensitivity of 9.24×10^3 rad/N.

The measurements results can be utilized as a good reference in designing and manufacturing new cantilevers and tips with better performance for modified LFM technique. However, future work is needed to further improve the accuracy and the resolution of the design model.

5.3 Recommendations for Future Work

The ECN computers available on campus for conducting the FEA have very limited RAM memory and storage, which significantly influence the performance of the FEA software and the accuracy of the measurements. In the future, computers with larger RAM and solid state storage will be preferred in performing finite element modelling.

The manipulation of the FEA softwares need to be improved. SolidWorks Prime simulation package is a powerful FEA tool and also has design study, convenient for run a group of simulation at one click. However, the investigation on cantilevers and tips at micro scale was performed at the limits of SolidWorks. In the future, more proficiency on the software should be developed, such as the manipulation of different usage of direct and iterative solvers, or the development of more efficient meshing control. More professional FEA simulation tools such as ABAQUS or COMSOL Multiphysics can be considered to improve the simulation accuracy.

The mLFM probe with the optimum configuration can be manufactured from graphite in future so the appropriate microfabrication methods for graphite need to be studied in the future. The fabrication and manipulation of graphite at micro-scale has been investigated by many, for instance, by scanning tunneling microscopy (McCarley, Hendricks & Allen, 1992) or chemical vapor deposition (Daly et al., 2012). How to implement these methods to the microfabrication of graphite cantilevers for mLFM entails further exploration.

The contact simulation between a hard sample and the tip have been conducted by the non-linear study of FEA. According to the data obtained in the Section 4.3, the measurement sensitivity of the same probe was subject to the type of samples. The soft sample selected in this study had higher elastic modulus than the real cells and remained linear deformation in the defined contact model. Thus, in order to add nonlinearity of cell membranes on the measurement

sensitivity, the sample with similar mechanical property to real cells are to be utilized in the simulation. Also, both the approach and retraction process should be simulated on the sample with similar mechanical property to real cells in the future to study the impact of resilience on the measurement sensitivity.

APPENDIX A PROCEDURES OF PARTS CREATION IN SOLIDWORKS

The procedures of model creation of cantilever design A

1. Open the **SolidWorks 2018** and create a new **part**.
2. Select the Front plane and click the **Sketch**. Draw the sketch of a rectangle for the short beam. Use **Smart Dimensions** to assign dimensions (length and width) and edit annotations. The sketch created will show up in the FeatureManager Design Tree as sketch1.
3. Select the sketch1 in the Design Tree and click **Features.** Use the **Extruded Boss/Base** to build the three-dimensional short beam. In the setting window of Extruded Boss/Base, determine the desired extrusion value (thickness).
4. Select the sidewall of the rectangle and click the **Sketch**. Draw two circles on the sidewall with the same distance to the center. Use **Smart Dimensions** to assign dimensions and edit annotations. The sketch created will show up in the FeatureManager Design Tree as sketch2.
5. Select the sketch2 in the Design Tree and click **Features.** Use the **Extruded Boss/Base** to build two wires. In the setting window of Extruded Boss/Base, determine the desired extrusion value.

The procedures of model creation of cantilever design B

1. Open the **SolidWorks 2018** and create a new **part**.
2. Select the Front plane and click the **Sketch**. Draw a triangle for V-shape cantilever. Use **Smart Dimensions** to assign dimensions and edit annotations. The sketch created will show up in the FeatureManager Design Tree as sketch1.
3. Select the sketch1 in the Design Tree and click **Features.** Use the **Extruded Boss/Base** to build the three-dimensional cantilevers. In the setting window of Extruded Boss/Base, determine the desired extrusion value (thickness).
4. Select the top plane of the triangle and click the **Sketch**. Use the **Line** to draw a small triangle in align of the edge of the cantilever fixed end. Use **Smart Dimensions** to assign dimensions and edit annotations. The sketch created will show up in the FeatureManager Design Tree as sketch2.
5. Select the sketch2 in the Design Tree and click **Features.** Use the **Extruded cut** to remove the small triangle to build a V-shape cantilever. The value of the cut is the same as the thickness.
6. Select the top plane of the triangle and click the **Sketch**. Use the **Line** to draw two small rectangles at two outer sides of the V-shape. Use **Smart Dimensions** to assign dimensions and edit annotations. The sketch created will show up in the FeatureManager Design Tree as sketch3.
7. Select the sketch2 in the Design Tree and click **Features.** Use the **Extruded cut** to remove small rectangles. The value of the cut is the same as the thickness.

The procedures of model creation of cantilever design C

1. Open the **SolidWorks 2018** and create a new **part**.
2. Select the Front plane and click the **Sketch**. Use the **Line** to draw sketch of hammerhead cantilever. Use **Smart Dimensions** to assign dimensions and edit annotations. The sketch created will show up in the FeatureManager Design Tree as sketch1.
3. Select the sketch1 in the Design Tree and click **Features.** Use the **Extruded Boss/Base** to build the three-dimensional cantilevers. In the setting window of Extruded Boss/Base, determine the desired extrusion value (thickness).
4. Select the top plane of the hammerhead cantilever solid and click the **Sketch**. Use the **Line** to draw a small rectangle in align of the edge of the cantilever fixed end. Make sure the rectangle is in the center of the cantilever top plane. Use **Smart Dimensions** to assign dimensions and edit annotations. The sketch created will show up in the FeatureManager Design Tree as sketch2.
5. Select the sketch2 in the Design Tree and click **Features.** Use the **Extruded cut** to remove the small triangle to build a V-shape cantilever. The value of the cut is the same as the thickness.

The procedures of model creation of cantilever design D

1. Open the **SolidWorks 2018** and create a new **part**.
2. Select the Front plane and click the **Sketch**. Draw a rectangle for the sketch of the horizontal beam. Use **Smart Dimensions** to assign dimensions and edit annotations. The sketch created will show up in the FeatureManager Design Tree as sketch1.
3. Select the sketch1 in the Design Tree and click **Features.** Use the **Extruded Boss/Base** to build the three-dimensional cantilevers. In the setting window of Extruded Boss/Base, determine the desired extrusion value (thickness of the horizontal beam).
4. Select the bottom plane of the rectangle solid and click the **Sketch**. Draw a small rectangle with the same length as the horizontal beam solid. Make sure the rectangle is in the center of the cantilever bottom plane. Use **Smart Dimensions** to assign dimensions and edit annotations. The sketch created will show up in the FeatureManager Design Tree as sketch2.
5. Select the sketch2 in the Design Tree and click **Features.** Use the **Extruded Boss/Base** to build the three-dimensional cantilevers. In the setting window of Extruded Boss/Base, determine the desired extrusion value (height of the vertical beam).

The procedures of model creation of tip designs

1. Open the **SolidWorks 2018** and open the part file of the cantilever which will be used for the tip design.
2. Select the bottom plane of the cantilever and click **Sketch**. Add a reference point on the center line of the cantilever. Use **Smart Dimensions** to edit distance from the point to the free end of the cantilever. The distance should be the desired distance from tip to the free end and the point will be the center of the tip base.
3. Select the point and click **Reference Geometry>Plane**. Select the point as the first reference and the right plane as the second reference. Let the new plane be perpendicular to the right plane. The new plane will show up in the FeatureManager Design Tree as plane1.
4. Select the plane1 and click the **Sketch**. Use Line to draw a centerline in the vertical direction. Use **Line** and **Circle** by three points to draw the sketch of tip design A. Use **Line** to draw the sketch of tip design A. The sketch will be the half of the front view of the tip design A splitted from centerline of the tip. the Use **Smart Dimensions** to edit dimensions and annotations. The sketch created will show up in the FeatureManager Design Tree as sketch4.
6. Select the sketch4 in the Design Tree and click **Features.** Use the **Revolved Boss/Base** to build the conical tips. In the revolve parameter panel, the revolve axis will be the centerline on the plane1. The revolution is 360˚. Click OK to create the revolved tip.

APPENDIX B PROCEDURES OF STATIC STUDY SET-UP IN SOLIDWORKS

Procedures of simulation set up of normal spring constant measurement

1. Open the **SolidWorks 2018** and open the file of cantilever to be tested.
2. Click **Simulation** in the tool bar and create a new **static** study. If the Simulation is not in the tool bar, click on the **SOLIDWORKS Add-Ins** and select Simulation.
3. Click **Apply Material** on the Simulation CommandManager and select the materials of interest and click apply. To add custom material, copy an existing material and paste it in the custom library. Then change name and material properties of the copy to material of interest.
4. Click **Add a Fixture** and select **fixed geometry**. After the Fixture PropertyManager appear, select the faces to be fixed at the end of the cantilever and click green check mark.
5. Click the down arrow on **External Loads** and select **Force**. Select the edge of the free end to add **Normal** force with the magnitude of 5×10^{-15}N.
6. Click the down arrow on **Run** and select **Create Mesh**. In the **Mesh Factor**, slide the slider to the rightmost position (**Fine**) to sets the global element size. In the **Mesh Parameters**, activate the standard mech and set the unit as micron. Change the element Size to 0.00274 μm to set the global average element size and click the green check mark.
7. Click **Run** on the Simulation CommandManager tool bar to run the simulation.

Procedures of simulation set-up of torsional spring constant measurement

1. Open the **SolidWorks 2018** and open the file of cantilever to be tested.
2. Click **Simulation** in the tool bar and create a new **static** study. If the Simulation is not in the tool bar, click on the **SOLIDWORKS Add-Ins** and select Simulation.
3. Click **Apply Material** on the Simulation CommandManager and select the materials of interest and click apply. To add custom material, copy an existing material and paste it in the custom library. Then change name and material properties of the copy to material of interest.
4. Click **Add a Fixture** and select **fixed geometry**. After the Fixture PropertyManager appear, select the faces to be fixed at the end of the cantilever and click green check mark.
5. Click Features > Curves > **Split Line** to separate the small area with the width of 1 μm from the cantilever entity so that torque can be applied in this area instead of the whole faces of cantilever.
6. Use Features > Reference Geometry > **Axis** to create the major axis of the cantilever, Axis 1 in Figure 3-10.
7. Click **Simulation** in the tool bar and create a new **static** study. If the Simulation is not in the tool bar, click on the **SOLIDWORKS Add-Ins** and select Simulation.
8. Click **Apply Material** on the Simulation CommandManager and select the materials of interest and click apply. To add custom material, copy an existing material and paste it in the custom library. Then change name and material properties of the copy to material of interest.

9. Click **Add a Fixture** and select **fixed geometry**. After the Fixture PropertyManager appear, select the faces to be fixed at the end of the cantilever and click green check mark.
10. Click the down arrow on **External Loads** and select **Torque**. Select the split faces on the cantilever in step 5 to apply the torque. Specify the **Total** value of the torque 5×10^{-15}Nm and select the Axis 1 as the reference geometry.
11. Click the down arrow on **Run** and select **Create Mesh**. In the **Mesh Factor**, slide the slider to the rightmost position (**Fine**) to sets the global element size. In the **Mesh Parameters**, activate the standard mech and set the unit as micron. Change the element Size to 0.00274 μm to set the global average element size and click the green check mark.
12. Click **Run** on the Simulation CommandManager tool bar to run the simulation.

Procedures of simulation set-up of maximum normal deflection

1. Open the **SolidWorks 2018** and open the file of cantilever to be tested.
2. Click **Simulation** in the tool bar and create a new **static** study. If the Simulation is not in the tool bar, click on the **SOLIDWORKS Add-Ins** and select Simulation.
3. Click **Apply Material** on the Simulation CommandManager and select the materials of interest and click apply. To add custom material, copy an existing material and paste it in the custom library. Then change name and material properties of the copy to material of interest.
4. Click **Add a Fixture** and select **fixed geometry**. After the Fixture PropertyManager appear, select the faces to be fixed at the end of the cantilever and click green check mark.
5. Click the down arrow on **External Loads** and select **Gravity**. Accept the default settings.
6. Click the down arrow on **Run** and select **Create Mesh**. In the **Mesh Factor**, slide the slider to the rightmost position (**Fine**) to sets the global element size. In the **Mesh Parameters**, activate the standard mech and set the unit as micron. Change the element Size to 0.00274 μm to set the global average element size and click the green check mark.
7. Click **Run** on the Simulation CommandManager tool bar to run the simulation.

APPENDIX C PROCEDURE FOR NONLINEAR STUDY SET-UP IN SOLIDWORKS

1. Create the part of probe (containing the cantilever and tip) and the sample using **Sketch** and **Features**.
2. Add one reference point on each of the sidewalls of the sample and the tip where they will be contacted for mating in Step 5.
3. Click Insert > Features > Split to separate the tip with the cantilever so that the tip can be assigned rigid in Step 9 and save the two bodies seperately.
4. Open the **SolidWorks 2018** and create a new **assembly**.
5. Click **Insert Component** on the Assembly toolbar to import probe (containing the cantilever and tip) part and the sample part.
6. Click the **Mate** on the Assembly toolbar. Assign the Front plane and bottom face of the sample as **parallel**. Assign the two points from Step 2 as **coincident**.
7. Click **Simulation** in the tool bar and create a new **nonlinear** study. If the Simulation is not in the tool bar, click on the **SOLIDWORKS Add-Ins** and select Simulation.
8. Click **Apply Material** and select the materials of interest and click apply. The cantilever and the tip are assigned as materials proposed in Chapter 3 and the sample is assigned as the silicon dioxide or sylgrid-184 elastomer.
9. In the simulation study tree, right-click the part of tip and select **make rigid**.
10. Click **Add a Fixture** and select **fixed geometry**. After the Fixture PropertyManager appear, select the faces to be fixed at the end of the cantilever and click green check mark.

11. Click the down arrow on **External Loads** and select **prescribed displacement**. Select the bottom face of the sample and assign the displacement direction as shown in Figure 3-12 with the value of 100 nm. Make the displacements towards other directions and rotations at all angles zero.
12. Click the down arrow on **External Loads** and select **Gravity**. Set the **reference plane** as the Top Plane and the Earth gravity as **9.81** m/s^2.
13. In the Simulation Study Tree, right-click the **Connections** and select **Component Contact**. Activate **Bonded** in the contact type and activate **Global Contact** in the components. Click √.
14. In the Simulation Study Tree, right-click the **Connections** and select **Contact Set**. Select the **No penetration** from selection box. Assign the sidewall of the cantilever that to be touch by the tip as the **Set 1** (source) and assign the sidewall of the tip that to be touched as the **Set 2** (target). Click √.
15. Right-click the study name in the Simulation study tree and select **Properties** > **Solution** > **Advanced options**. Change the **singularity-elimination-factor** to 0.5.
16. In the **Solution**, increase the **initial increment** to 0.001 and **max increment** to 0.05.
17. Click the down arrow on **Run** and select **Create Mesh**. In the **Mesh Factor**, slide the slider to the rightmost position (**Fine**) to sets the global element size. In the **Mesh Parameters**, activate the curvature-based meshing and set the unit as micron. Change the element Size to 0.00274 μm to set the global average element size and click √ .
18. Click **Run** on the Simulation CommandManager tool bar to run the simulation.

REFERENCES

Amakawa, H., Fukuzawa, K., Shikida, M., Tsuji, H., Zhang, H., & Itoh, S. (2012). An electrostatic actuator for dual-axis micro-mechanical probe on friction force microscope. *Sensors and Actuators, A: Physical*, *175*, 94–100.

Bhushan, B., & Marti, O. (2017). Scanning Probe Microscopy—Principle of Operation, Instrumentation, and Probes. In *Nanotribology and Nanomechanics* (pp. 33–93). Cham: Springer International Publishing.

Bhushan, B., & Agrawal, G. B. (2002). Stress analysis of nanostructures using a finite element method. Nanotechnology, 13(4), 515.

Bickel, P., Diggle, P., Fienberg, S., Krickeberg, K., Wermuth, N., & Zeger, S. (2003). The design and analysis of computer experiments (1st ed.). New York, NY: Springer Science and Business Media.

Binning, G., & Quate, C. F. (1986). Atomic Force Microscopy. *Physical Review Letters*, *56*(9), 930–933.

Binning, G., & Rohrer, H. (1982). Scanning tunneling microscopy Scanning tunneling microscopy. *Helvetica Physica Acta*, *55*, 726–735. https://doi.org/10.5169/seals-115309

Bouwens, A. J. (1986). Digital instrumentation. New York: McGraw-Hill.

Bruker AFM Probe. (2019). DNP. Retrieved from https://www.brukerafmprobes.com/p-3588-dnp.aspx

Cappella, B., & Dietler, G. (1999). Force-distance curves by atomic force microscopy. *Surface Science Reports*, *34*, 1–104.

Chan, C. E., & Odde, D. J. (2008). Traction dynamics of filopodia on compliant substrates. *Science*, *322*(5908), 1687–1691.

Choi, J. L., & Gethin, D. T. (2009). Simulation of atomic force microscopy operation via three-dimensional finite element modelling. *Nanotechnology,* 20(6), 065702.

Cleveland, J. P., Manne, S., Bocek, D., & Hansma, P. K. (1993). A nondestructive method for determining the spring constant of cantilevers for scanning force microscopy. *Review of Scientific Instruments*, *64*, 3789.

Cordova, G., Attwood, S., Gaikwad, R., Gu, F., & Leonenko, Z. (2014). Magnetic Force Microscopy Characterization of Superparamagnetic Iron Oxide Nanoparticles (SPIONs). *Nano Biomedicine and Engineering*, *6*(1), 31–39.

Dai, J., & Sheetz, M. P. (1995). *Mechanical Properties of Neuronal Growth Cone Membranes Studied by Tether Formation with Laser Optical Tweezers*. *Biophysical Journal* (Vol. 68).

Daly, R., Kumar, S., Lukacs, G., Lee, K., Weidlich, A., Hegner, M., & Duesberg, G. S. (2012). Cell proliferation tracking using graphene sensor arrays. Journal of Sensors, 2012.

Dinelli, F., Buenviaje, C., & Overney, R. M. (2000). Glass transitions of thin polymeric films: Speed and load dependence in lateral force microscopy. *The Journal of Chemical Physics*, *113*.

Eaton, P., & West, P. (2010). Atomic force microscopy. Oxford university press.

Frisbie, C. D., Rozsnyai, L. F., Noy, A., Wrighton, M. S., & Lieber, C. M. (1994). Functional Group Imaging by Chemical Force Microscopy Chemical Force Microscopy. *Source: Science, New Series Genome Issue*, *265*(5181), 2071–2074.

Fukuzawa, K., Terada, S., Shikida, M., Amakawa, H., Zhang, H., & Mitsuya, Y. (2006). Dual-axis micromechanical probe for independent detection of lateral and vertical forces. *Applied Physics Letters*, *89*(17).

Granta. (2019). CES EduPack 2018 [Windows]. Cambridge

Hazel, J. L., & Tsukruk, V. V. (1999). Spring constants of composite ceramic/gold cantilevers for scanning probe microscopy. *Thin Solid Films*, *399*, 249–257.

Hatami, M. (2019). Modeling composites in biomedical engineering. Materials for Biomedical Engineering: Bioactive Materials, Properties, and Applications, 101.

Hopf, R., Bernardi, L., Menze, J., Zündel, M., Mazza, E., &Ehret, A. E. (20160. Experimental and theoretical analysis of the age-dependent large-strain behavior of Sylgrid 184 (10:1) silicone elastomer. Journal of the mechanical behavior of biomedical materials, 60, 425-437.

Hseu, Y. K. (2015). Development of modified lateral force microscopy technique (Thesis, Purdue University).

Kasza, K. E., Rowat, A. C., Liu, J., Angelini, T. E., Brangwynne, C. P., Koenderink, G. H., & Weitz, D. A. (2008). The cell as a material. *Current Opinion in Cell Biology*, *19*(Cell structure and dynamics), 101–107.

Koch, D., Rosoff, W. J., Jiang, J., Geller, H. M., & Urbach, J. S. (2012). Strength in the Periphery: Growth Cone Biomechanics and Substrate Rigidity Response in Peripheral and Central Nervous System Neurons. *Biophysical Journal*, *102*(3), 452–460.

Li, J. D., Xie, J., Xue, W., & Wu, D. M. (2013). Fabrication of cantilever with self-sharpening nano-silicon-tip for AFM applications. Microsystem technologies, 19(2), 285-290.

Mate, C. M., Mcclelland, G. M., Erlandsson, R., & Chiang, S. (1987). Atomic-Scale Friction of a Tungsten Tip on a Graphite Surface. *Scanning tunnelling microscopy*, *59*(17).

Mathur, A. B., Collinsworth, A. M., Reichert, W. M., Kraus, W. E., & Truskey, G. A. (2001). Endothelial, cardiac muscle and skeletal muscle exhibit different viscous and elastic properties as determined by atomic force microscopy. *Journal of Biomechanics* (Vol. 34).

McCarley, R. L., Hendricks, S. A., & Bard, A. J. (1992). Controlled nanofabrication of highly oriented pyrolytic graphite with the scanning tunneling microscope. The Journal of Physical Chemistry, 96(25), 10089-10092.

Mitsuya, Y., Ohshima, Y., & Nonogaki, T. (1997). Coupling and nonlinear effects of cantilever deflection and torsion encountered when simultaneously measuring vertical and lateral forces using the scanning probe method. *Wear*, *211*(2), 198–202.

Moeendarbary, E., & Harris, A. R. (2014). Cell mechanics: Principles, practices, and prospects. *Wiley Interdisciplinary Reviews: Systems Biology and Medicine*, *6*(5), 371–388.

Morris, V. J., Kirby, A. R., & Gunning, A. P. (2014). *Atomic Force Microscopy for Biologists* (2nd ed.). Imperial College Press.

Mott, R. L. (2007). Applied strength of materials. CRC Press.

Müller, M., Schimmel, T., Haußler, P., Fettig, H., Müller, O., & Albers, A. (2006). Finite element analysis of V-shaped cantilevers for atomic force microscopy under normal and lateral force loads. *Surface and Interface Analysis*, *38*, 1090–1095.

Munz, M. (2010). Force calibration in lateral force microscopy: a review of the experimental methods. *Journal of Physics D: Applied Physics*, *43*(6), 063001.

Murad, J. (2019) Errors in FEA and Understanding Singularities (Beginners' Guide). Retrieved from https://www.simscale.com/blog/2016/06/errors-in-fea-and-singularities/

Mustata, M., Ritchie, K., & Mcnally, H. A. (2010). Neuronal elasticity as measured by atomic force microscopy. *Journal of Neuroscience Methods*, *186*, 35–41.

Neumeister, J. M., & Ducker, W. A. (1994). Lateral, normal, and longitudinal spring constants of atomic force microscopy cantilevers. *Review of Scientific Instruments*, *65*(8), 2527–2531. https://doi.org/10.1063/1.1144646

Pidaparti, R. M. (2017). *Engineering Finite Element Analysis Synthesis*. Synthesis digital library of engineering and computer science. Retrieved from http://store.morganclaypool.com

Reitsma, M. G., Gates, R. S., Friedman, L. H., & Cook, R. F. (2011). Prototype cantilevers for quantitative lateral force microscopy. *Review of Scientific Instruments*, *82*(9).

Sadaie, M., Nishikawa, N., Ohnishi, S., Tamada, K., Yase, K., & Hara, M. (2006). Studies of human hair by friction force microscopy with the hair-model-probe. *Colloids and Surfaces B: Biointerfaces*, *51*(2), 120–129.

Sader, J. E. (2003). Susceptibility of atomic force microscope cantilevers to lateral forces Susceptibility of atomic force microscope cantilevers to lateral forces, *2438*(4), 2438–2443.

Sader, J. E., & Sader, R. C. (2003). Susceptibility of atomic force microscope cantilevers to lateral forces: Experimental verification. *Applied Physics Letters*, *83*(15), 3195–3197.

Salon, S. J. (1995). Finite element analysis of electrical machines (Vol. 101). Boston: Kluwer academic publishers.

Schillers, H., Rianna, C., Schäpe, J., Luque, T., Doschke, H., Wälte, M., ... & Dumitru, A. (2017). Standardized nanomechanical atomic force microscopy procedure (SNAP) for measuring soft and biological samples. Scientific reports, 7(1), 5117.

Shah, C. (2002). Mesh discretization error and criteria for accuracy of finite element solutions. In Ansys Users Conference (Vol. 12).

Shen, Q., Edler, M., Griesser, T., Knall, A.-C., Trimmel, G., Kern, W., & Teichert, C. (2014). *Ex situ* and *in situ* characterization of patterned photoreactive thin organic surface layers using friction force microscopy. *Scanning*, *36*(6), 590–598.

Thomas, G., Burnham, N. A., Camesano, T. A., & Wen, Q. (2013). Measuring the mechanical properties of living cells using atomic force microscopy. JoVE (Journal of Visualized Experiments), (76), e50497.

Tortonese, M. (1997). Cantievers and tips for atomic force microscopy. *IEEE Engineering in Medicine and Biology*, (April), 28–33.

Tseng, Y., Kole, T. P., & Wirtz, D. (2002). Micromechanical Mapping of Live Cells by Multiple-Particle-Tracking Microrheology. *Biophysical Journal*, *83*(6), 3162–3176.

Wang, L., Chauveau, J. M., Brenier, R., Sallet, V., Jomard, F., Sartel, C., & Brémond, G. (2016). Access to residual carrier concentration in ZnO nanowires by calibrated scanning spreading resistance microscopy. *Appl. Phys. Lett*, *108*(132103), 1–5.

Weihs, T. P., Nawaz, Z., Jarvis, S. P., & Pethica, J. B. (1991). Limits of imaging resolution for atomic force microscopy of molecules. *Citation: Appl. Phys. Lett*, *59*(3536).

Weisenhorn, A. L., Hansma, P. K., Albrecht, T. R., & Quate, C. F. (1989). Forces in atomic force microscopy in air and water. *Applied Physics Letters*, *54*, 2651–1045.

Williams, C. C. (1999). Two-dimensional dopant profiling by scanning capacitance microscopy. *Annu. Rev. Mater. Sci* (Vol. 29). Retrieved from www.annualreviews.org

Xu, H., Chen, X., Men, K., & Sun, H. (2018). Simulation and Experimental Verification for Composite Material Structure of Helicopter Tail Fin. In Asia-Pacific International Symposium on Aerospace Technology (pp. 2830-2837). Springer, Singapore.

Zhong, Q., Inniss, D., Kjoller, K., & Elings, V. B. (1993). Fractured polymer/silica fiber surface studied by tapping mode atomic force microscopy. *Surface Science Letters*, *290*(1–2), L688–L692.